THÈSE

présentée

devant l'UNIVERSITÉ CLAUDE BERNARD - LYON I

pour l'obtention

du DIPLÔME de DOCTORAT

(arrêté du 25 avril 2002)

présentée et soutenue publiquement le

23 octobre 2006

par

Roland   ACKERMANN

Propagation of terawatt-femtosecond laser pulses and its application to the triggering and guiding of high-voltage discharges

Directeur de thèse: Jean-Pierre WOLF

Jury:

Président :	M.	G.	BOULON
Rapporteurs :	M.	L.	BERGÉ
	M.	L.	WÖSTE
Examinateurs :	M.	W.	SANDNER
	M.	J.-P.	WOLF

UNIVERSITE CLAUDE BERNARD LYON I

Président de l'Université   **M. le Professeur D. DEBOUZIE**

Vice-Président du Conseil Scientifique   M. le Professeur J.F. MORNEX
Vice-Président du Conseil d'Administration   M. le Professeur R.GARRONE
Vice-Président du Conseil des Etudes et de la Vie Universitaire   M. Le Professeur G. ANNAT
Secrétaire Général   M. J.P. BONHOTAL

SECTEUR SANTE

Composantes

UFR de Médecine Lyon R.T.H. Laënnec	Directeur : M. le Professeur D. VITAL-DURAND
UFR de Médecine Lyon Grange-Blanche	Directeur : M. le Professeur X. MARTIN
UFR de Médecine Lyon-Nord	Directeur : M. le Professeur F. MAUGUIERE
UFR de Médecine Lyon-Sud	Directeuer : M. le Professeur F.N. GILLY
UFR d'Odontologie	Directeur : M. O. ROBIN
Institut des Sciences Pharmaceuteques et Biologiques	Directeur : M. le Professeur F. LOCHER
Institut Techniques de Réadaptation	Directeur : M. le Professeur L. COLLET

Département de Formation et Centre de Recherche en Biologie
Humaine   Directeur : M. le Professeur P. PARGE

Département de Production et Ralisation Assistance Conseil
en Technologie pou l'Education   Directrice : Mme. le Professeur M. HEYDE

SECTEUR SCIENCES

Composantes

UFR de Physique	Directeur : M. le Professeur A. HOAREAU
UFR de Biologie	Directeur : M. le Professeur H. PINON
UFR de Mécanique	Directeur : M. le Professeur H. BEN HADID
UFR de Génie Electrique et des Procédés	Directeur : M. le Professeur A. BRIGUET
UFR Sciences de la Terre	Directeur : M. le Professeur P. HANTZPERGUE
UFR de Mathématiques	Directeur : M. le Professeur M. CHAMARIE
UFR d'Informatique	Directeur : M. le Professeur M. EGEA
UFR de Chimie Biochimie	Directeur : M. le Professeur J.P. SCHARFF
UFR STAPS	Directeur : M. le Professeur R. MASSARELLI
Observatoire de Lyon	Directeur : M. le Professeur R. BACON
Institut des Sciences et des Techniques de l'Ingénieur de Lyon	Directeur : M. le Professeur J. LIETO
IUT A	Directeur : M. le Professeur C. COULET
IUT B	Directeur : M. le Professeur R. LAMARTINE
Institut de Science Financière et d'Assurances	Directeur : M. le Professeur J.C. AUGROS

Abstract

When an ultrashort-terawatt laser pulse is propagating through the atmosphere, long filaments may develop. Their light is confined in an area of about 100 µm over distances up to several hundred meters, and an air plasma is generated along the beam path. Moreover, filamentation leads to a significant broadening of the initial pulse spectrum. These properties open the perspective to improve classical LIDAR techniques as well as to laser lightning control.

In the laboratory, we have shown that the filaments survive the propagation through highly turbulent air as well as under adverse atmospheric conditions such as rain and reduced pressure. By using an multi-terawatt, ultrashort laser pulse, the white-light LIDAR signal could be detected at an altitude of more than 20 km for the first time.

In cooperation with high-voltage facilities, the effective plasma lifetime for the laser guiding of discharges and the achievable guided lengths have been determined. By using an additional nanosecond laser pulse, the triggering probability could be significantly enhanced. Furthermore, we have shown that the triggering and guiding is possible in artificial rain.

These results encourage further research aiming at the application of white-light LIDAR and real-scale lightning control.

Résumé

La propagation d'une impulsion térawatt ultra-brève dans l'atmosphère peut s'accompagner du phènomène de filamentation. La lumière se trouve alors auto-guidée dans des plasmas appelés filaments dont le diamètre est de l'ordre de 100 µm et la longueur peut s'étendre jusqu'à quelques centaines de mètres. De plus, le spectre initial de l'impulsion est considerablement élargi. Ces propriétés offrent la possibilité d'améliorer la technique LIDAR et de contrôler la foudre.

Nous avons montré que les filaments survivent à la propagation dans une turbulence forte et peuvent se développer sous une pression atmosphérique réduite et sous la pluie. Pour la première fois, la lumière blanche genérée par une impulsion ultra-brève, multi-terawatt a été détectée à une altitude de 20 km.

En collaberation avec des installations haute-tension, nous avons déterminé la durée de vie du plasma du filament et la longueur sur laquelle il est possible de guider des décharges électriques. Nous avons pu augmenter l'efficacité de déclenchement avec une configuration à double impulsion. Enfin, nous avons montré que le déclenchement et le guidage sont possibles sous une pluie artificielle.

Ces résultats se sont révélés très encourageants en vue d'expériences LIDAR à lumière blanche et du contrôle de la foudre.

Acknowledgements

First of all, I would like to thank Prof. Jean-Pierre Wolf for having been kindly received in his group in Lyon. His open-mindedness to even very concrete experimental issues has led to a pleasant and uncomplicated working atmosphere.

Equally, I would like to thank Prof. Ludger Wöste, who had recommended me for this PhD-position and has interestedly kept in contact all along.

I am very grateful to Jérôme who always had an ear for all kinds of questions - from assistance at the French registration office to reading the proofs of this work.

Thanks to Prof. Luc Bergé for agreeing to be rapporteur of my thesis and to the other members of the jury, Prof. Georges Boulon and Prof. Wolfgang Sandner, who agreed to join my defence in Lyon in spite of the long journey.

Thanks to my predecessor Guillaume, especially for helping me to take all imaginable hurdles of university administration, and to Estelle for her reliable and, most often, hard work on the laser. Thank you Noëlle, especially for reading the proofs of this work.

Special thanks go to Kamil and Philipp. I highly appreciated the faithful and amicable atmosphere among us, even after I had left Berlin.

By the way, thank you Jin for some unforgetable nights until sunrise during the LIBS-campaign at the "FU-Berlin". Thank you Grégoire for, at least psy-

Contents

Contents

1 Introduction

Since the invention of the first laser by Theodore Maiman in 1960, present pulsed laser systems have reached power and time scales that are beyond our imagination. The time duration of the shortest pulses has attained the attosecond scale (1 as = 10^{-18} s) [PWKC99], whereas the available peak intensity has reached the petawatt regime (1 PW = 10^{15} W) [PPS$^+$99]. The increase of the available intensities has thereby often been accompanied by the discovery of new interaction processes between light and matter, whereas the reduction of the pulse duration at the same time enables to increase the resolution of time-resolved experiments.

This work is concerned with ultrashort[1] laser pulses on the order of several hundreds of femtoseconds (1 fs = 10^{-15} s) at power levels in the terawatt regime (1 TW = 10^{12} W). The phenomenon that is associated with the propagation of ultrashort laser pulses in air at these power levels is the so-called *filamentation*, whose investigation is the main objective of the experiments described in this work.

Their properties open the perspective to a variety of novel laser applications. The filaments confine the propagating laser light in a small volume within the beam, having a radius of about 100 µm each at distances up to several hundred meters, *e. g.* allowing the enhancement of the application radius of classical laser techniques, such as *LIBS* (Laser Induced Breakdown Spectroscopy)

---

[1]Commonly, pulses with a duration shorter than 1 ps are referred to as *ultrashort* pulses.

[RYM$^+$04]. It is a method to identify chemical elements by their characteristic plasma emission, induced by the laser radiation. The filamentation is accompanied by the formation of an air plasma along the beam path, enabling the control of high-voltage discharges, or even lightning strokes in the future. Furthermore, the initial pulse spectrum is significantly broadened due to nonlinear processes in air such as *Self-Phase-Modulation (SPM)*, offering the possibility to advance the precision of the classical *LIDAR* (LIght Detection and Ranging) technique [RBM$^+$04]. Figure 1.1 shows a picture of the emitted supercontinuum of filaments in the atmosphere.

The experiments that are presented in this work may be divided into two parts. One ensemble of experiments concerns the fundamental research on the propagation of the filaments in the laboratory and in the atmosphere. These are in particular the investigation of the influence of adverse ambient conditions on the formation and propagation of filaments, as their capability to withstand
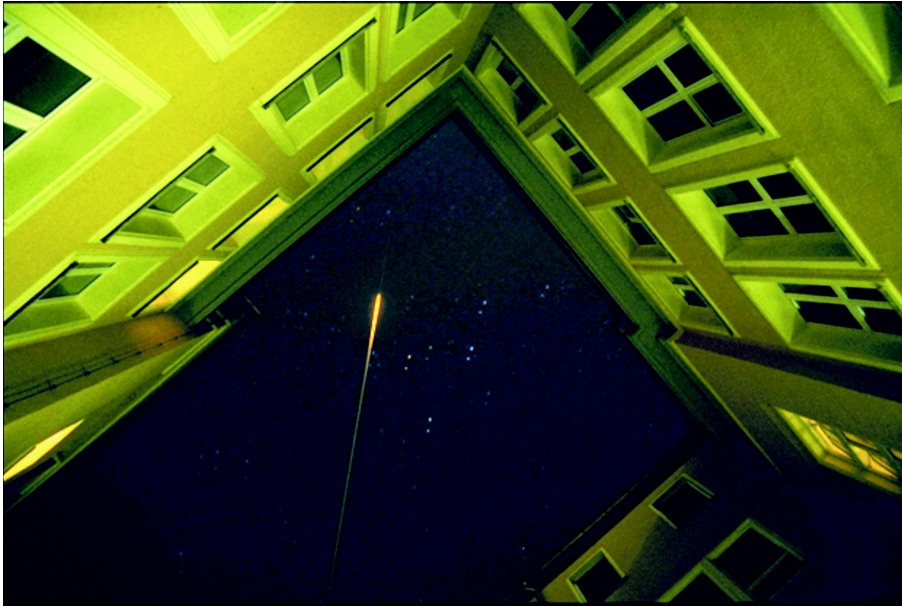

Figure 1.1: The supercontinuum emitted from filaments, produced by a TW-femtosecond laser in the atmosphere. The picture was taken in the courtyard of the faculty of physics of the "Friedrich-Schiller-Universität Jena" (Photo: K. Wedekind).

unfavourable atmospheric conditions is a precondition for further research in this field. Further experiments investigated the effects of higher laser pulse energies on the filament parameters, and the optimization of the temporal shape of the pulse.

The second part deals with the application to high-voltage discharge experiments in air. In these experiments, we have investigated important parameters of the laser triggering process, such as the plasma lifetime of the filament and its effective length. In subsequent experiments we investigated how these parameters may be increased by the use of additional laser sources, and we tested the influence of artificial rain on the triggering efficiency of the filament.

Most of the experiments of my thesis have been conducted with the *Teramobile* [WRK$^+$02, KRM$^+$03], which is a unique mobile terawatt-femtosecond laser system, installed in a standard shipping container. It is obvious that the operation of such a laser system demands a lot of manpower and implies teamwork.

For this reason, I have tried to keep the focus on those experiments to which I contributed most, either by participating in the experiments or analyzing the results. These are in particular the high-voltage experiments, described in chapter 5. In contrast, I will not detail the LIBS-campaign, in which I shortly participated. Nevertheless, this part of the campaign has led to two publications [RSW$^+$05, SRM$^+$04], and a comprehensive description of the LIBS-experiments is given by Ph. Rohwetter [Roh04].

The present work is structured as follows: The next chapter introduces the theoretical background of the filamentation of ultrashort laser pulses in air and gives a brief introduction into the physics of high-voltage discharges in nonuniform gaps. The third chapter describes technical aspects of the generation of high-power, ultrashort laser pulses, and presents the Teramobile. The chapter thereafter comprises the beam propagation experiments, which investigated the influence of adverse ambient conditions on the filamentation. The high-

voltage experiments are presented in chapter 5. Chapter 6 and 7 present two experiments, which evaluate possible improvements of the present techniques for the generation of filaments, namely the optimization of the temporal pulse shape and the effects of a multi-terawatt, high-energy pulse, respectively. The final chapters give a conclusion and outlook of the experiments of this work.

2 Theoretical background

The aim of this chapter is to introduce the theoretical background and the physical processes that are important for the comprehension of the presented experiments, and to present the most relevant work done in this subject area.

The first section will give a mathematical description of ultrashort laser pulses from a phenomenological point-of-view. Then, the filamentation of ultrashort laser pulses in air and the underlying nonlinear processes are presented. Thereafter, a paragraph about the theory of pulse shaping with spatial light modulators is inserted, as this type of device has been used for the experiments optimizing the temporal pulse shape.

The last section of this chapter is dedicated to an introduction to the physics of high-voltage discharges, which stands a little bit apart from the subjects normally taught to physicists. The basic processes in the development and propagation of high-voltage discharges will be presented, turning special attention to negative discharges in highly-nonuniform gaps, as used in our experiments.

2.1 Ultrashort laser pulses
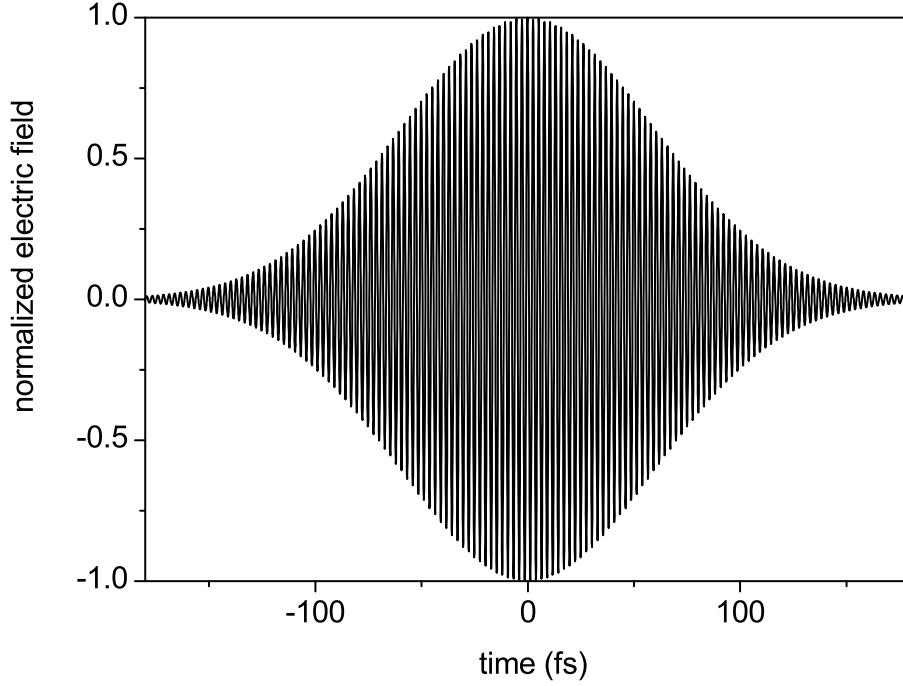
Figure 2.1: The electric field of an ultrashort laser pulse with a pulse duration of 100 fs (FWHM).

Figure 2.1 shows the electric field $E(t)$ of a Gaussian femtosecond laser pulse with the typical parameters used in this work. The pulse has a duration of $\Delta t = 100$ fs, which is defined as the full-width-at-half-maximum (FWHM) of its intensity

$$I(t) = \epsilon_0 c n \int\limits_{t-T/2}^{t+T/2} E^2(t')\mathrm{d}t',\tag{2.1}$$

by averaging $E^2(t')$ over one optical period T. In praxis, T is only of theoretical relevance and has to be replaced by the response time τ_r of the detector. The central wavelength of the pulse, displayed in the present example, is $\lambda = 795$ nm, corresponding to a frequency of 3.77×10^{14} Hz.

Mathematically, the pulse can be described by an amplitude $A(t)$ and phase

$\Phi(t)$ [DR96]

$$E(t) = A(t)e^{i\Phi(t)}, \tag{2.2}$$

for which the complex representation is usually chosen in order to simplify the calculations. The electric field $E(t)$ in the time and frequency domain $\hat{E}(\omega)$ are linked by Fourier-transformation

$$E(t) = \frac{1}{\sqrt{2\pi}} \int_{-\infty}^{\infty} \hat{E}(\omega)e^{i\omega t}\mathrm{d}\omega \tag{2.3}$$

$$\hat{E}(\omega) = \frac{1}{\sqrt{2\pi}} \int_{-\infty}^{\infty} E(t)e^{-i\omega t}\mathrm{d}t. \tag{2.4}$$

The spectrum of the above pulse is shown in figure 2.2, having a width of $\Delta\lambda = 12$ nm or $\Delta\omega = 3.26 \times 10^{13}$ rad/s, centered at $\lambda = 795$ nm. As the electric field $E(t)$ is real, the spectrum obeys the symmetry $\hat{E}(\omega) = \hat{E}(-\omega)$. Therefore, it is convenient to use only the positive frequency contribution, leading to the complex fields

$$E^+(t) = A(t)e^{i\Phi(t)} \tag{2.5}$$

$$\hat{E}^+(\omega) = \hat{A}(\omega)e^{-i\hat{\Phi}(\omega)}, \tag{2.6}$$

where $\hat{E}^+(\omega) = 0$ for $\omega \leq 0$. $E^+(t)$ is the electric field in the time domain obtained by the Fourier-transformation of $\hat{E}^+(\omega)$. Owing to the high frequencies occurring in the optical spectrum ($\omega_0 = 2.37 \times 10^{15}$ rad/s at $\lambda = 795$ nm) it is also convenient to separate out the quickly oscillating carrier frequency ω_0

$$\Phi(t) = \phi(t) - \omega_0 t. \tag{2.7}$$

The temporal derivative of the phase

$$\omega(t) = \frac{d\Phi(t)}{dt} = \frac{d\phi(t)}{dt} - \omega_0 \tag{2.8}$$

yields a time dependent, so-called instantaneous frequency $\omega(t)$.
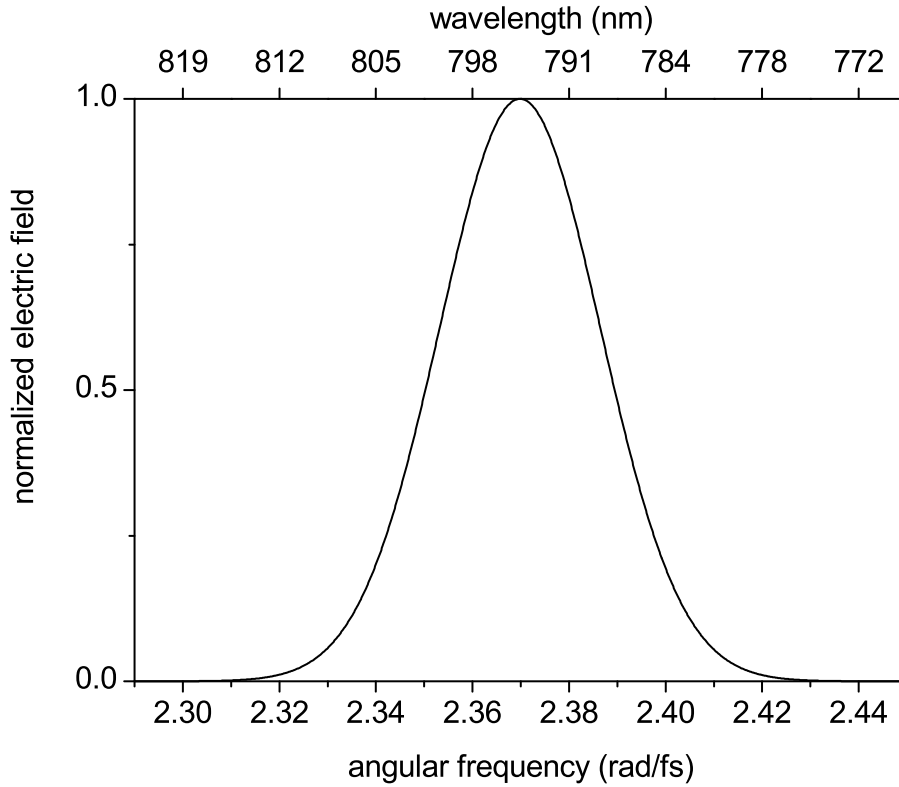
Figure 2.2: The spectrum of an ultrashort laser pulse with a pulse duration of 100 fs (FWHM).

A Gaussian shape is a good approximation for pulses produced in a laser cavity, and their electric field in the time and frequency domain can be expressed by [DR96]

$$E^+(t) \quad \propto \quad e^{-2\ln 2 \frac{t^2}{\Delta t^2}} e^{it\omega_0} \tag{2.9}$$

$$\hat{E}^+(\omega) \quad \propto \quad e^{-\frac{\Delta t^2}{4\ln 2}(\omega-\omega_0)^2}. \tag{2.10}$$

The time dependence of the phase and instantaneous frequency, respectively, are the key parameters when working with femtosecond laser pulses. Furthermore, the discussion of the influence of different phase functions on the temporal pulse shape is also essential for the understanding of the pulse shaping experiments discussed in chapter 6. Therefore, the following section will discuss the effect of different phase modulation functions on the temporal pulse shape.

2.1.1 Phase modulations in the frequency domain

The phase modulation of the incident wave $\hat{E}_{in}$ can generally be expressed by

$$\hat{E}_{out}(\omega) = e^{-i\psi(\omega)}\hat{E}_{in}(\omega). \tag{2.11}$$

For a classification of the different types of phase modulations, the general phase function $\psi(\omega)$ is expanded into a Taylor-series around the carrier frequency ω_0

$$\psi(\omega) = b_0 + b_1(\omega - \omega_0) + \frac{1}{2}b_2(\omega - \omega_0)^2 + \frac{1}{6}b_3(\omega - \omega_0)^3 + ... \tag{2.12}$$

Then, the influence of the coefficients b_0, b_1 and b_2 on the temporal pulse shape $E(t)$ can be easily understood by performing the corresponding Fourier-tranformation [DR96]

$$E(t) = \frac{1}{\sqrt{2\pi}}e^{i\omega_0 t}e^{-ib_0}\int_{-\infty}^{\infty}\hat{E}_{in}(\omega)e^{i(t-b_1)(\omega-\omega_0)}e^{-i\sum_{n=2}^{\infty}b_n(\omega-\omega_0)^n}\mathrm{d}\omega. \tag{2.13}$$

The coefficient b_0 leads to a shift of the carrier frequency with respect to the pulse envelope. Pulses of several 100 fs, as in the experiments presented in this work, feature many optical cycles within the pulse (see figure 2.1), so that the shift of the carrier is negligible. This would become significant, however, for pulse durations on the order of a few femtoseconds that consist only of a few optical cycles. In this case the position of the carrier frequency indeed has an influence on the pulse shape (see figure 2.3(a)).

The coefficient b_1 leads to a delay of the pulse due to the factor $e^{i(t-b_1)(\omega-\omega_0)}$. It has therefore no practical effect in single-pulse experiments. However, it may be used to investigate the limitations of a pulse shaping setup (see section 2.4).

In order to discuss the influence of the next coefficient b_2, equation (2.13) can be rewritten

$$E(t) = \frac{1}{\sqrt{2\pi}}e^{i\omega_0 t}\int_{-\infty}^{\infty}\hat{E}_{in}(\omega)e^{-ib_0}e^{i((t-b_1)-b_2(\omega-\omega_0))(\omega-\omega_0)}e^{-i\sum_{n=3}^{\infty}b_n(\omega-\omega_0)^n}\mathrm{d}\omega. \tag{2.14}$$

One notices that the term b_2 induces a delay proportional to the frequency shift relative to the central frequency ω_0. It results in a continuously varying instantaneous frequency, called *linear chirp*. Additionally, the pulse duration is increased.

In order to illustrate quantitatively the influence of b_2, definite pulse shapes have to be considered. For a Gaussian pulse, the effect of a coefficient $b_2 \neq 0$ can be expressed by [DSLS84]

$$E^+(t) = \frac{E_0}{2\gamma^{0.25}} e^{-\frac{t}{4\beta\gamma}} e^{i(\delta t^2 - \epsilon)} e^{i\omega_0 t}, \tag{2.15}$$

where $\beta = \frac{\delta t^2}{8\ln 2}$, $\gamma = 1 + \frac{\psi''^2}{4\beta^2\gamma}$, $\delta = \frac{\psi''}{8\beta^2\gamma}$ and $\epsilon = 0.5\arctan(\frac{\psi''}{2\beta})$ and

$$\psi'' = b_2 = \left| \frac{d^2\psi}{d\omega^2} \right|_{\omega_0}. \tag{2.16}$$

Figure 2.3 shows the influence of $b_2 = \pm 15$ fs^2 on a pulse with an initial pulse duration of 2 fs. In both cases (figure 2.3(b),(c)) the pulse duration is increased to about 15 fs, but for a *positive chirp* (b), or *up-chirp*, the red part of the pulse spectrum is found in the leading edge of the pulse, whereas in the case of a *negative chirp* (c), or *down-chirp*, the blue part of the spectrum is found in the leading edge of the pulse.

Chirps always appear when ultrashort laser pulses propagate through a medium such as air or glass, where the spectral components of the pulse are subject to a different refractive index. This effect is called *Group Velocity Dispersion* (GVD). In order to discuss the contributions of the different chirp orders (see equation (2.12)), table 2.1 displays numerical values for $b_2 = \psi''$ and $b_3 = \psi'''$ for BK7 at $\lambda = 800$ nm.

$n(\omega_0)$	$n'(\omega_0)$ (10^{-2} fs)	$n''(\omega_0)$ (10^{-3} fs^2)	$n'''(\omega_0)$ (10^{-4} fs^3)	$\psi''(\omega_0)$ (fs^2 mm^{-1})	$\psi'''(\omega_0)$ (fs^3 mm^{-1})
1.5106	0.67	0.06	39	45.14	31

**Table 2.1:** Values for the linear and quadratic chirp of BK7 at $\lambda = 800$ nm [DR96].
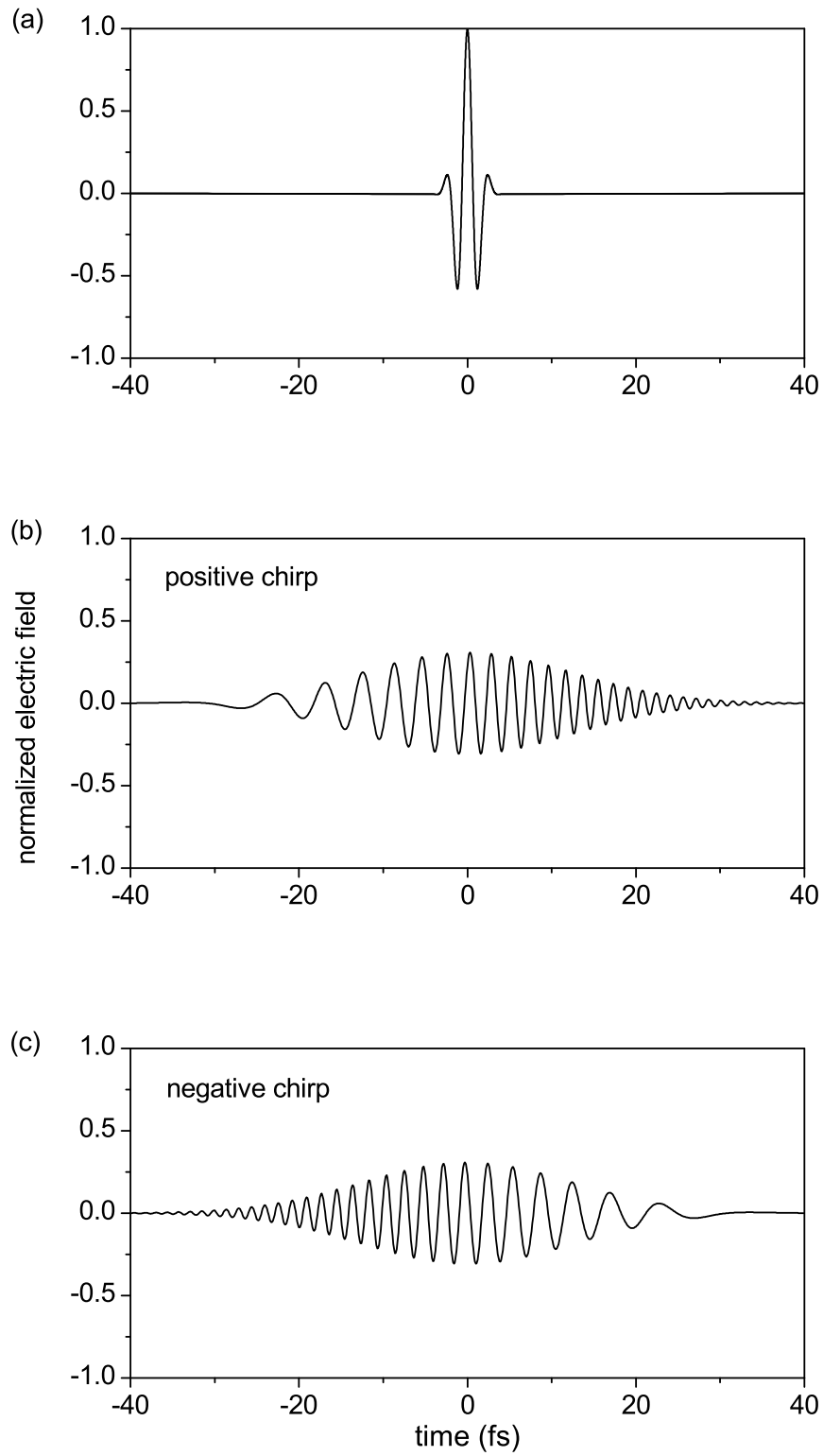
Figure 2.3: The electric fields of a Gaussian pulse in the time domain for different chirps. (a) shows the original pulse with a FWHM of 2 fs and no chirp, (b) the same pulse with a positive chirp of $b_2 = 15$ fs^2 and (c) with a negative chirp.

The values for $\psi^{''}$ and $\psi^{'''}$ are calculated from the derivatives

$$\left|\frac{d^2\psi}{d\omega^2}\right|_{\omega_0} = \frac{d}{c}\left|\left(2\frac{dn}{d\omega} + \omega\frac{d^2n}{d\omega^2}\right)\right|_{\omega_0} \tag{2.17}$$

$$\left|\frac{d^3\psi}{d\omega^3}\right|_{\omega_0} = \frac{d}{c}\left|\left(3\frac{d^2n}{d\omega^2} + \omega\frac{d^3n}{d\omega^3}\right)\right|_{\omega_0} \tag{2.18}$$

of the general expression for the phase shift after the propagation through a medium

$$\psi(\omega) = \frac{\omega}{c}n(\omega)d, \tag{2.19}$$

where c is the speed of light and d the thickness of the medium. Inserting the values of $\psi^{''}$ and $\psi^{'''}$ into equation (2.12), one obtains for a 100 fs-pulse ($\Delta\lambda \approx 10$ nm or $\Delta\omega \approx 2.77 \times 10^{13}$ rad/s)

$$\Delta\phi_{linear\ chirp} \approx 0.004\ \frac{rad}{mm} \tag{2.20}$$

$$\Delta\phi_{quadratic\ chirp} \approx 0.000014\ \frac{rad}{mm}. \tag{2.21}$$

Therefore, for pulse durations on the order of 100 fs, the contribution of the quadratic and higher order chirps is negligible. Yet, shorter pulses require the consideration of higher order chirps due to the increasing frequency bandwidth.

The pulse broadening due to the linear chirp, fortunately, may be reversed by employing a special grating arrangement [DR96, Mar87, SM85, Tre69]. It will be presented in section 3.1, where the technical aspects of the generation of ultrashort laser pulses are being discussed.

2.2 Nonlinear propagation of ultrashort laser pulses

After ultrashort laser pulses have been discussed within the scope of linear optics, the following section will introduce the phenomena of nonlinear optics that lead to the occurrence of filaments in air. Nonlinear effects come at play

when the response of a system upon which an external force is acting may not be approximated by a linear relation. In the case of optics, it is the electric field of the light wave that interacts with the atoms of the medium through which it is propagating. The light from ordinary lamps induces an electric field of about $E \approx 1$ V/cm, which is negligible compared to the Coulomb force between the electron and the nucleus of $E = e/4\pi\epsilon_0 r_{Bohr}^2 \approx 6 \times 10^{11}$ V/m. However, with regard to high-power lasers this relation changes considerably, and one could even reach the field strength within the atom by focusing the Teramobile beam at a distance of a few meters.

The following section will give an introduction to the propagation of light through a dispersive medium and present the specific phenomenon of light filaments. Then, the most contributing nonlinear effect, the optical Kerr-effect and its manifestations in the time and spatial domain - self-phase modulation and the self-focusing - will be presented. Thereafter, a section describing the generation of higher harmonics will be exposed although it is not directly connected with the filamentation process but one of the most important nonlinear optical effects. The last paragraph of this section will give an overview of the general properties of light filaments and the most important previous work.

2.2.1 The Rayleigh length diffraction limit

This section presents the processes that lead to the occurrence of filaments in air. In order to understand the peculiarity of this phenomenon, one has to consider, how a laser beam propagates through a medium.

An ordinary laser beam can be described by the so-called Gaussian modes, for which the simplest case, the Gaussian zero-mode (TEM_{00}) is expressed by [EE98]

$$I(z, \rho) = I_0 \exp\left(-\frac{\rho^2}{w_0^2(1 + \frac{(z-f)^2}{z_0})}\right), \qquad (2.22)$$

where ρ is the distance from the beam axis, f the focal length and w_o the beam radius at $z = 0$. Then, the parameter that indicates in which area the beam can be treated as a plane wave, is the Rayleigh-zone z_0. For the Rayleigh-zone, the following relation is derived in vacuum

$$w_0^2 = \frac{\lambda z_0}{\pi}. \tag{2.23}$$

This context is depicted in figure 2.4. Within the Rayleigh-zone $b = 2z_0$ the laser beam is regarded as a plane wave but diverges with the angle $\alpha = w_0/z_0$. The Rayleigh-zone for a laboratory laser with a typical beam diameter of 1 cm at $\lambda = 800$ nm is about 100 m.

This situation changes considerably when the beam is focussed by a convex lens. Classical ray optics fails in this case, as it predicts a beam diameter of zero in the focal point of the lens. The model of a Gaussian beam, however, allows the calculation of the diameter within the focus [Mes99]

$$w_{02} \cong \frac{\lambda f}{\pi w_{01}}, \tag{2.24}$$

where w_{01} and w_{02} are the beam radii before and after the lens, respectively. Focusing a beam with a lens with a focal length of f = 10 cm ($\lambda = 800$ nm, $w_{01} = 1$ cm) yields a beam radius at the position of the focus of $w_{02} \approx 5$ µm. Then, the corresponding Rayleigh-zone is only $z_0 \approx 100$ µm. This is of importance insofar as high intensities are commonly achieved by tight focusing.
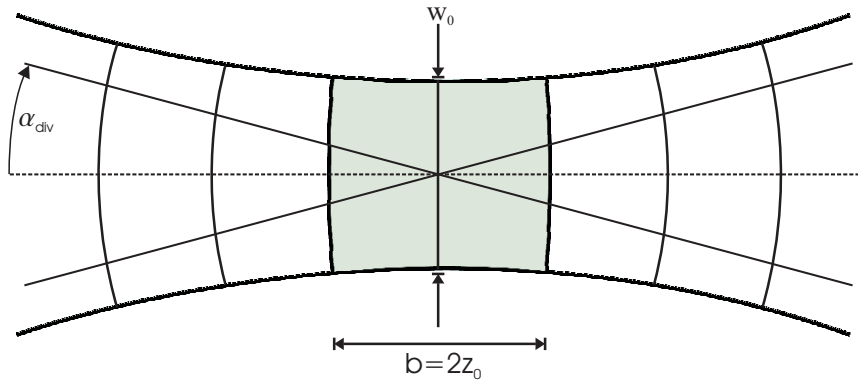

Figure 2.4: The Gaussian zero-mode TEM$_{00}$

Beyond the Rayleigh length

The occurrence of a laser filament, however, seems to be a violation of this law. Its light is confined in area not greater than 100 - 150 µm, but can reach a length of several meters in the laboratory and up to several hundred meters in the atmosphere [LVJ⁺99, MDA⁺05]. In air the phenomenon was observed for the first time by A. Braun *al.* in 1995 [BKL⁺95], using 200 fs pulses with energies up to 50 mJ. A single filament was developing above an energy threshold of about 5 mJ, and multiple filament were observed starting at 20 mJ. The beam was not focussed by a lens, focusing was exclusively achieved by the so-called self-focussing effect, which will be discussed in detail in the next paragraph. Since then, the occurrence of filaments has been confirmed in a multitude of experiments.

The effect, leading to the formation of filaments, has been intensively discussed throughout the last decades among two competitive theories. The moving-focus theory [BCI⁺97, LGR⁺98, LS69, SC94] assumed that the nonlinear focus of the beam "propagates" along the beam path in front of the pulse due to nonlinear effects. After the detection of free charges within the filament [SS99, Tzo01, TFA⁺99], however, the theory of a self-guiding filament [BLG⁺68, BKL⁺95, NCG⁺96] is now commonly accepted.

The next paragraph will present the nonlinear processes leading to the formation of filaments.

2.2.2 The optical Kerr-effect

When light is propagating through a medium, the electric field causes a polarization

$$\vec{P}(\omega) = \vec{P}(\vec{E}(\omega)) \tag{2.25}$$

that depends on the frequency ω of the incident light. For low intensities, this relation can be linearized to

$$\vec{P}(\omega) = \epsilon_0 \chi(\omega) \vec{E}(\omega), \tag{2.26}$$

where ϵ_0 is the dielectric constant and $\chi(\omega)$ the electric susceptibility.

However, for high intensity laser pulses this approximation does not hold anymore, and the polarization, in general, has to be expanded into a power series of E

$$\vec{P} = \epsilon_0 [\chi^{(1)}\vec{E} + (\chi^{(2)}\vec{E})\vec{E} + ((\chi^{(3)}\vec{E})\vec{E})\vec{E}) + ...]. \tag{2.27}$$

The susceptibilities $\chi^{(1,2,3,...)}$ are tensors of the degree (n+1) for the order n of E. Their contribution remains negligible unless high intensities are at play. In centro-symmetrical media such as air or glass, it is $\chi^{(2n)} = 0$ for $n \geq 1$, so that the main contribution for filamentation are third order effects. These are the so-called *self-phase modulation* (SPM) in the temporal and *self-focusing* in the spatial domain. Both phenomena can be subsumed under the term *optical Kerr-effect.*

In general, $\chi^{(3)}$ is a tensor of 4th degree, but in isotropic media such as air, the susceptibility can be characterized by a single parameter n_2 at a given frequency, and together with the general expression for the refractive index $n = \sqrt{1 + \chi}$ one obtains

$$n = n_{linear} + n_2 I, \tag{2.28}$$

where

$$n_2 \propto \frac{\chi^3}{n_{linear}}. \tag{2.29}$$

As the intensity of a laser pulse is proportional to E^2, the nonlinear Kerr-effect, therefore, leads to a dependence of the refractive index on the intensity I. The contribution of the optical Kerr-effect in air was measured by Nibbering *et al.* to be $n_2 = 3 \times 10^{-19}$ cm^2/W [NGF$^+$97] for pulses with a duration on the order of 100 fs, whereas earlier a value of $n_2 = 5.6 \times 10^{-19}$ cm^2/W was

assumed [PHH89]. The latter value was measured for nanosecond instead of ultrashort pulses, however, leading to the measured discrepancies along with the small absolute contribution of n_2.

Since laser pulses exhibit intensity gradients in both the temporal and spatial dimension, the nonlinear Kerr-effect accordingly affects both domains. In the spatial dimension, this is the so-called self-focusing, whereas the temporal effect is called self-phase modulation (SPM). Both will be discussed in the next paragraphs.

Self-phase-modulation
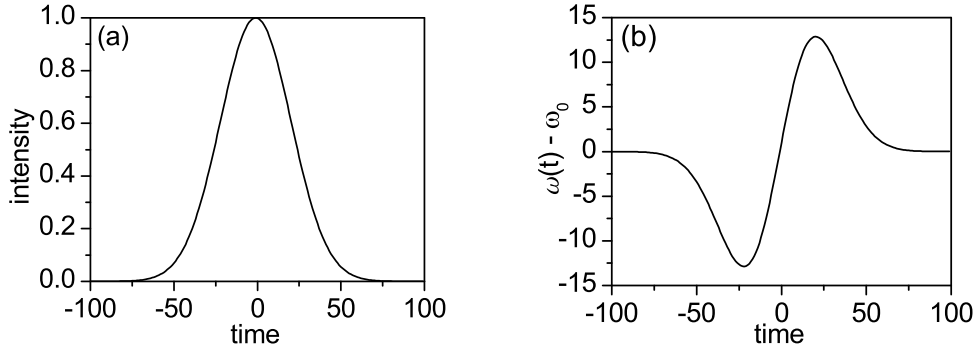
Figure 2.5: (a) the intensity of a Gaussian pulse in the time domain and (b) the instantaneous frequency $\omega(t)$ due to self-phase-modulation.

Even more evident than the spatial profile of a laser pulse is its Gaussian temporal shape as shown in figure 2.5(a). According to equation (2.28) for the optical Kerr-effect, the change of the refractive index due to a time-dependent electric field is

$$\Delta n(t) = n_2 E(t)^2. \tag{2.30}$$

After the propagation through a medium with the thickness z, this leads to an additional phase shift of

$$\Delta \phi_{SPM}(t) = \frac{z \omega_0}{c} n_2 E^2(t). \tag{2.31}$$

Along with $\omega(t) = \frac{d\Phi(t)}{dt}$ and $E^2 \propto I$, one obtains

$$\omega(t) = \omega_0 - \frac{\omega_0 n_2 z}{c} \frac{dI}{dt} \tag{2.32}$$

Therefore, a Gaussian pulse with an initially constant instantaneous frequency (figure 2.3(a)), shows now a time dependent frequency $\omega(t)$ as shown in figure 2.5(b) with the lower frequencies at the leading edge and the higher frequencies at the end of the pulse, *i. e.* its spectrum has been broadened. The self-phase modulation is regarded as the main contribution to the supercontinuum generation, as it has also been confirmed by numerical simulations based on the solution of the nonlinear Schrödinger equation [AIB+02, KKG+03, KKMW03].

Self-focussing

In paragraph 2.2.1 it has been pointed out that the spatial profile of a laser beam can be described by a Gaussian distribution, and according to the derived equation (2.28) for the optical Kerr-effect, the refractive index increases when approaching from the edges of the beam to its axis. The beam itself, therefore, acts as a convex lens, constricting its own diameter during propagation. In order to yield a net effect, however, the optical Kerr-effect must still overcome the linear diffraction, and it was shown by Marburger [DM69, Mar75] that this requires a critical laser power

$$P_{crit} = \frac{\lambda^2}{2\pi n_0 n_2}, \tag{2.33}$$

where λ is the laser wavelength and n_0 the linear refractive index of the medium. One has to notice that the critical power does not depend on the beam diameter and, hence, does not depend on the beam intensity. For $\lambda = 800$ nm the critical power in air is $P_{crit} \approx 3$ GW. Marburger also calculated the nonlinear focal length $z_f(P)$ arising from the self-focusing effect

$$\frac{1}{z_f(P)} = -\frac{1}{R} \pm \frac{\sqrt{(\sqrt{P/P_{crit}} - 0.852)^2 - 0.0219}}{0.367 k a^2}, \tag{2.34}$$

where R is the initial curvature of the wave-front, k the wave-vector and a the beam radius (1/e). For a typical femtosecond-laser with 10 mJ pulse energy at $\lambda = 800$ nm, delivering P = 100 GW, one obtains $z_f \approx 50$ m.

In order to be able to work on a laboratory scale, the beam, therefore, is often additionally focused by a lens, for which according to Marburger the simple lens equation holds

$$\frac{1}{z_{net}} = \frac{1}{f} + \frac{1}{z_f},$$ (2.35)

where f is the focal length of the focusing optics and z_{net} the resulting focal length of both contribution.

The Marburger formula (2.34), which was obtained empirically from rough numerical calculations in condensed matter, does not make a statement about the behavior of the beam diameter at the position at the focal point. Due to the very high intensity within the focus, it may come to optical breakdown of the ambient medium, eventually leading to its destruction. But under appropriate conditions, it may also be the onset of a filament. The mechanisms leading to the formation of the filaments will be discussed in section 2.3.

2.2.3 Air plasma

As addressed above, the self-focusing would lead to the collapse of the beam if there were no opposing effects. In the context of the self-guiding model [BKL$^+$95, BLG$^+$68, NCG$^+$96] it is the formation of a low density plasma that counteracts the effect of self-focusing. In contrast to high-energy laser pulses, ionization by femtosecond laser pulses is governed by Multi-Photon-Ionization or electron tunneling. The Keldish-parameter γ_k denotes which type of ionization takes place for a given laser-wavelength λ, intensity I and ionization potential U_{ion} of the corresponding atoms

$$\gamma_k = 2.3 \times 10^6 \sqrt{\frac{U_{ion}}{\lambda^2 I}}.$$ (2.36)

For $\gamma_k \ll 1$, ionization is dominated by the tunneling processes, for $\gamma_k \gg 1$ by MPI. For $\gamma_k = 1$, a laser wavelength of $\lambda = 800$ nm and a typical ionization potential of about 10 eV for air molecules, one obtains $I \approx 10^{14}$ W/cm^2. This value is on the order of the estimated, critical intensity within the filament of $I_{crit} = 4 \times 10^{13}$ W/cm^2 [BAV$^+$01, KSC00], meaning that the ionization process within the filament is a transition regime between Multi-Photon-Ionization and tunneling.

The generated plasma is able to counteract the self-focusing of the beam, since its contribution to the refractive index is negative, which can be derived from Drude's theory (see *e. g.* [AM76]) for the conductivity of electrons

$$n = \sqrt{1 - \frac{\omega_p^2}{\omega^2}}, \tag{2.37}$$

where ω is the angular frequency of the incident light, and

$$\omega_p = \frac{N_e e^2}{m_e \epsilon_0} \tag{2.38}$$

the so-called plasma frequency. Equation (2.37) shows that the refractive index becomes imaginary if the light frequency is lower than the plasma frequency, meaning that plasma becomes opaque. This is described by the critical plasma density

$$N_{crit} = \frac{\omega^2 m \epsilon_0}{e^2} \tag{2.39}$$

that is the electron density at which the plasma becomes opaque at a given wavelength ω. At $\lambda = 800$ nm, the critical density is $N_{crit} \approx 2 \times 10^{21}$ cm^{-3}, which is two orders of magnitude higher than the density of air molecules ($N_{air} \approx 2.5 \times 10^{19}$ cm^{-3}). Equation (2.37) can be expressed in the terms of densities

$$n = 1 - \frac{N_e}{2N_{crit}}, \tag{2.40}$$

where N_e is the plasma density, and the square root in equation (2.37) has been approximated, as the contribution of the quotient $\frac{N_e}{N_{crit}}$ is small.

2.2.4 Generation of higher harmonics

This section describes the generation of higher harmonics of an intense laser source within a medium. This effect is not directly associated with the filamentation process, however, it is one of the most important nonlinear, optical effects and encountered in many circumstances when working with high intensity laser pulses.

The generation of higher harmonics is the nonlinear response of a medium that is irradiated by intense light. Expressing the incident light by $E(t) = E_0 \sin \omega t$ leads to a nonlinear polarization according to equation (2.27)

$$\vec{P} = \epsilon_0[\chi^{(1)} E_0 \sin \omega t + (\chi^{(2)} E_0) E_0 \sin^2 \omega t + ...((\chi^{(3)} E_0) E_0) E_0) + \sin^3 \omega t + ...].$$
(2.41)

Restricting the expansion to the second order term $\chi^{(2)}$ leads to

$$\vec{P} = \epsilon_0 \chi^{(1)} E_0 \sin \omega t + \frac{\epsilon_0}{2}(\chi^{(2)} E_0) E_0[1 - \cos 2\omega t] + ...$$
(2.42)

Hence, apart from the linear response oscillating with the original frequency, a light wave with a doubled frequency is emitted. This effect is called *frequency doubling* or *second harmonic generation* (SHG). One has to remark that the second harmonic does not occur in isotropic media such as air. This is easily understood by comparing the second order polarization due to an electric field E and $(-E)$

$$-\vec{P}^{(2)} = \epsilon_0(\chi^{(2)}(-\vec{E}))(-\vec{E}) = \epsilon_0(\chi^{(2)} E) E = \vec{P^{(2)}}.$$
(2.43)

This requires that $\chi^{(2)} = 0$. However, second harmonic generation is exploited in crystals without inversion symmetry, for which well-known examples are the BBO and KTP [Mes99]. It allows, for example, the down-conversion of an infrared laser source to the visible spectrum.

The lack of inversion symmetry is not sufficient to effectively generate the second harmonic, as the refractive index of the fundamental wavelength $n(\omega)$ is,

in general, different from that of the second harmonic $n(2\omega)$, leading to destructive interference. The necessary identity $n(\omega) = n(2\omega)$, the so-called *phase matching*, is achieved in birefringent crystals by adapting their orientation to the incident light.

Although the second harmonic does not occur in air, the third harmonic has been observed in the supercontinuum of filaments created in the laboratory and in the atmosphere, which will be presented in the following section.

2.3 The properties of filaments in air

This section gives a brief summary of the main properties of air filaments and of previous work done about filamentation.

The filamentation process is depicted schematically in figure 2.6. At first, the self-focusing effect (paragraph 2.2.2) leads to a contraction of the beam diameter within the distance z_f, where the air is ionized. Owing to the opposite refractive index change within the plasma (paragraph 2.2.3), the beam is defocussed leading to a decreasing amount of plasma creation, and this dynamic balance allows the propagation of the filament beyond several Rayleigh-lengths. In the laboratory, with typical pulse energies of several mJ, lengths of several meters are observed when the beam is slightly focused [BKL$^+$95], whereas the Teramobile provides pulse energies on the order of several hundred mJ, being capable to produce filamentation over a length of up to several hundred meters
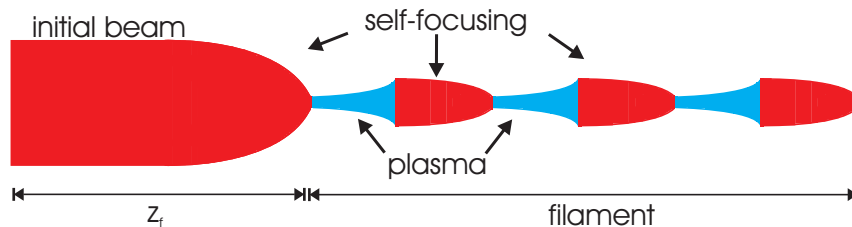

**Figure 2.6:** Sketch of the filamentation process.
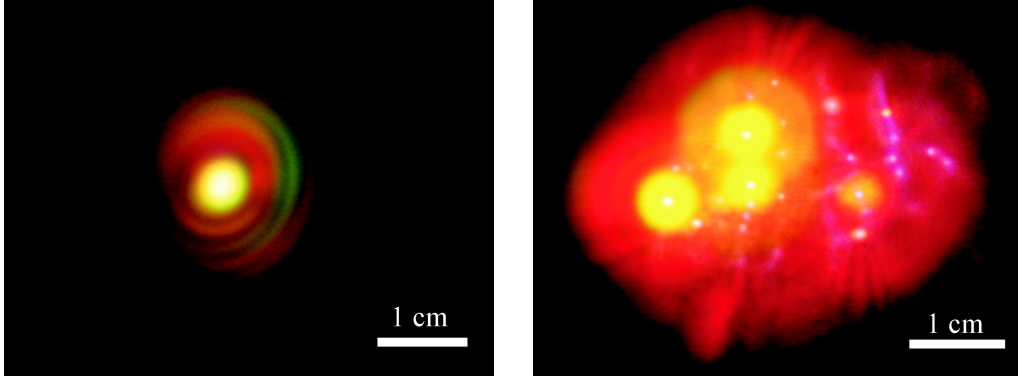
Figure 2.7: The supercontinuum emitted from a singe filament (left) and multiple filaments.

[LVJ$^+$99, MDA$^+$05].

A broad range of plasma densities within the filament has been reported, between $N_e \approx 10^{12}$ cm^{-3} [SS99] and $N_e \approx 10^{18}$ cm^{-3} [YZL$^+$02]. This discrepancy is related to different measurement techniques, such as optical or electric conductivity methods, which transversely average the electron density over the cross section of the beam, enclosing more or less the surface beyond the filament. Moreover, the high value of $N_e = 10^{18}$ cm^{-3} has to be questioned, since the measurements have not been performed on actual filaments, as a tightly focussed beam (f $\geq$ 40 cm) along with high pulse energies of up to 50 mJ were used. The most commonly accepted value is on the order of $N_e = 10^{15}$ - 10^{16} cm^{-3}. It has been obtained by interferometric measurements [Ack03] on a plasma focus of a femtosecond beam (f = 10 cm, E$_{pulse}$ = 6 mJ) and by shadowgraphy [TPFM00]. Numerical simulations yield a density of $n_e \approx 10^{16}$ - 10^{17} cm^{-3} [YZY$^+$01], and Kasparian *et al.* [KSC00] analytically estimated an electron density of $N_e \approx 10^{14}$ - 10^{15} cm^{-3}.

The relatively large uncertainty about the electron density within the plasma channel is mainly due to its low absolute value. The plasma dynamics, being outlined in section 2.5, takes place on a pico- and nanosecond scale, for which only optical measurement techniques offer an appropriate time resolu-
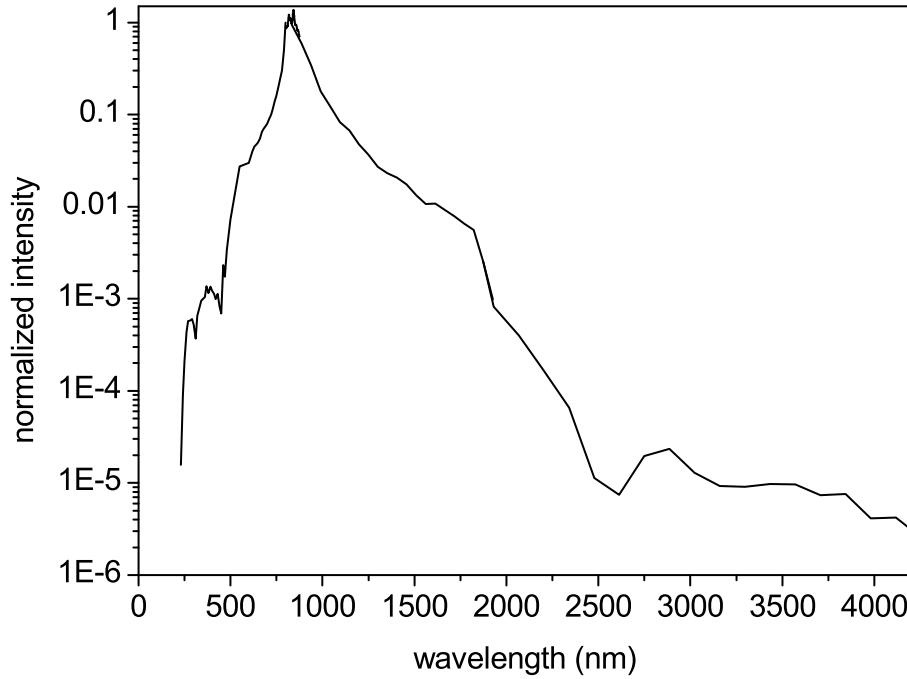
Figure 2.8: The spectrum of the supercontinuum emitted from filaments in the atmosphere [KSM$^+$00].

tion. Yet, according to equation (2.40), the change of the refractive index is only on the order of of $\Delta n = 10^{-5}$ for an electron density of $N_e \approx 10^{16}$ cm^{-3} at $\lambda = 800$ nm. On the other hand, it is remarkable that this tiny refractive index change is able to prevent the beam from collapsing due to the self-focusing mechanism.

The photo emission spectrum of N$_2$ and N$_2^+$ within the filament was detected by Talebpour *et al.* [TPC99]. A simple technique in order to determine the plasma density profile as well as the filament length was presented by J. Yu *et al.* [YMK$^+$03] via sonographic probing of the generated plasma. In contrast to filaments produced by lasers with a beam diameter of typically 1 cm, the Teramobile, having a diameter that is about three times larger at a peak power of several hundred P_{crit}, leads to multiple filaments, typically 10 - 20 filaments across the beam diameter. Multiple filaments arise from a non-uniform intensity profile, and numerical simulations [BSL$^+$04] are in good aggreement with
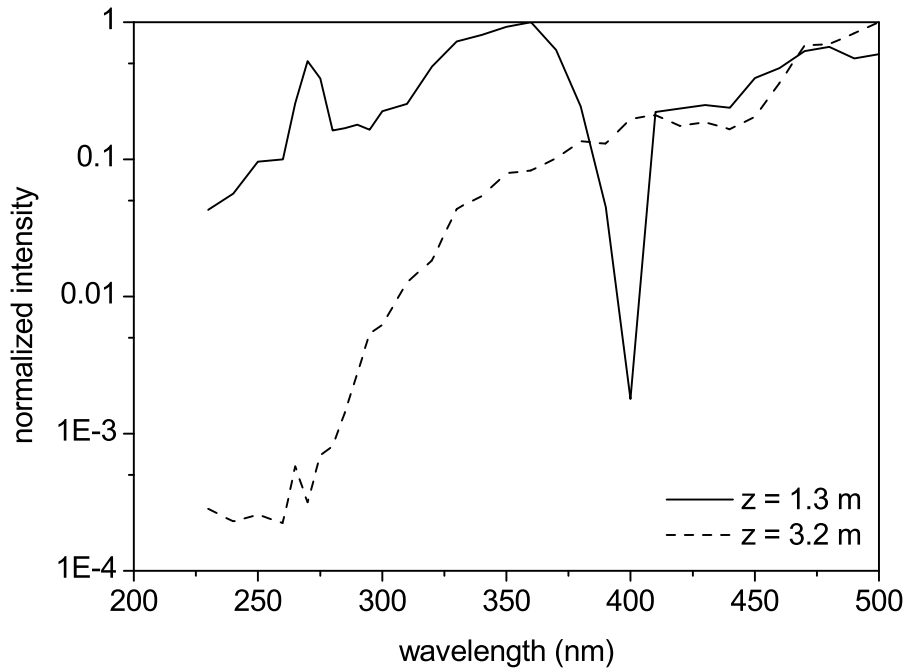
Figure 2.9: The UV-extension of the generated supercontinuum for two diferent distances z from the nonlinear focus.

measurements on the Teramobile beam.

The diameter of the filament was measured between d $\approx$ 50 µm [TFA$^+$99] up to d $\approx$ 380 µm [LGR$^+$98]. Most authors [BKL$^+$95, KSC00] report a diameter of about 100 µm. Along with the formation of filaments, a broadening of the original pulse spectrum is observed. Figure 2.7 shows both the supercontinuum emitted from a single filament (left picture) and from multiple filaments produced by the Teramobile beam. As mentioned above, the main contribution to the generation of the supercontinuum is the spectral broadening due to the self-phase modulation.

The spectrum of the supercontinuum (see figure 2.8), generated by terawatt-femtosecond pulses in the atmosphere was measured to span from the UV to $\lambda = 4.5$ µm in the infrared [KSM$^+$00]. Recent measurements in the laboratory that were also part of my work (see figure 2.9) [MKY$^+$06], showed an UV-extension of the spectrum down to 230 nm, limited by the atmospheric

transmission window. At short distance after the nonlinear focus, the generation of the third harmonic can be identified, whereas the spectrum shows a broadening in total for longer propagation distances.

The generation of the supercontinuum offers an opportunity to improve the LIDAR (LIght Detection and Ranging) technique [Mea84], which is even a commercially available method for the remote detection of pollutants and aerosols in the atmosphere. Classical LIDAR techniques detect the backscattered light of a monochromatic laser source and calculate the gas concentration from the absorbed laser light. Yet, the gas to be measured has to be known in advance in order that the corresponding laser wavelength within the absorption band may be chosen. Furthermore, additional scatteres or absorbers in the atmosphere lead to systematic errors of this classical technique. In the case of white-light LIDAR, however, the broad spectrum of the generated white-light even could allow the detection of unknown gases, and the deliberate choice of detection wavelengths within the spectrum of the supercontinuum may considerably advance the accuracy of the measurements. Moreover, the self-guiding effect of the filaments assures detection ranges on the kilometer scale. The capability of the white-light LIDAR technique has already been proven by the detection of atmospheric components [BMK+05, Méj05, Rod04] and bioaerosols [MKY+04].

Yet, the pictures in figure 2.7 show an additional feature of the emitted white-light, the so-called conical emission. The conical emission denotes the angle dependent spectrum of the emitted light, visible by the colored rings around the beam center. The phenomenon was already observed in 1968 by Sacchi *et al.* [STL68], but several interpretations remain. One explanation may be that the conical emission is generated by Cherenkov radiation. Cherenkov radiation is observed, when the radiation source moves faster than the phase velocity of the emitted light. The analogy to the conical emission is the pulse propagating at a higher velocity than the emitted supercontinuum because of normal dispersion. Numerical simulations of Nibbering *et al.* [NCG+96] and Kosareva

et al. [KKB+97] are in good agreement with the observed angle dependence of the conical emission.

An important feature of the conical emission is the fixed divergence angle of the emitted light of about 5 mrad (half-angle). In particular, it turned out that this angle does not depend on input parameters such as pulse energy or additional, geometric focusing. This property has been successfully exploited to determine the onset of filaments by photographing the projected white-light on a cloud layer in a known altitude and measuring their diameter [RBM+04]. This phenomenon is also visible on the right picture of figure 2.7, where some filaments appear as big yellow circles, meaning that they have developed early during the pulse propagation, whereas those appearing as small white spots are still in the state of formation.

2.4 The spatial light modulator

This section gives an introduction to the manipulation of the temporal pulse shape by a spatial light modulator that has been used for the optimization experiment discussed in chapter 6.

The idea of spatial light modulators (SLM) is to spatially separate the broad-band spectrum of an ultrashort laser pulse, allowing to independently manipulate the different spectral components. Then, the temporal pulse shape is affected via the Fourier-transformation, given by equation (2.4). There exist different implementations for the introduction of the phase shift on the spectral components, such as deformable mirrors [HCTS91, ZMB+99], acousto-optic modulators (AOM) [DTW97, HTG+94] and liquid crystal masks [WLPWI92, Wei00]. In our experiments, we used the latter type of implementation, whose mode of operation will be presented in the following paragraph.

Pulse shaping with liquid crystal light modulators

The principle design of a spatial light modulator is shown in figure 2.10.

It consists of two gratings, of which the first one spectrally disperses the incoming laser pulse in the horizontal plane. The cylindric lenses are placed such that the whole setup would work as a "zero-dispersion" compressor if there were no phase modulator installed. In other words, the first lens performs a Fourier-transformation of the incoming laser pulse, given by equation (2.5)

$$E_{out}^+(\omega) = F\{E_{in}(t)\}. \tag{2.44}$$

The pulse shaper mask, then, is placed in the Fourier plane in order that the spectral components are modulated as

$$E_{out}^+(\omega) = H(\omega)E_{in}^+(\omega) = E_{in}^+(\omega)R(\omega)e^{-i\psi(\omega)}. \tag{2.45}$$

Here, $R(\omega)$ represents the amplitude filter and $e^{-i\psi(\omega)}$ the phase filter. Finally, the second lens performs the inverse Fourier-transformation, and the reassembled beam leaves the setup. These considerations imply the approximation of thin lenses without chromatic aberration, which is valid for pulses with durations not shorter than 20 fs [Wei00].

The first experiments that applied this setup to femtosecond laser pulses, used fixed phase masks [WHK88], whereas the advent of programmable masks
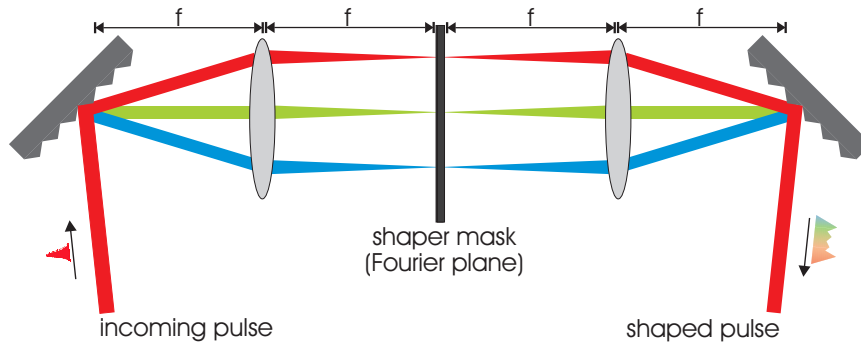

Figure 2.10: The basic setup of a pulse shaper apparatus in a 4f-configuration.
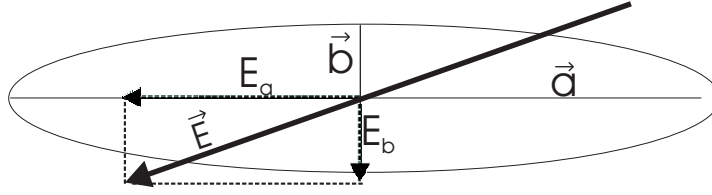
Figure 2.11: The orientation of incident linearily, polarized light with respect to the ordinary $\vec{a}$ and extraordinary $\vec{b}$ crystal axes.

[WLPWI92] offered the desired influencing of the different components. In the case of liquid crystal masks, the phase modulation is based on the birefringent properties of the liquid crystal. In contrast to a solid state crystal, in which both the orientation and the position of the molecules, or crystal basis, are fixed, in liquid crystals only the orientation is predefined. Birefringent crystals have anisotropic optical properties, and in the simplest case of only one anisotropic axis, two refractive indices, the ordinary index n_e and the extraordinary index n_o, can be assigned for light polarized along the corresponding axes.

The reference system for the two refractive indices are the ordinary and extraordinary crystal axes as shown in figure 2.11. The polarization vector of arbitrarily polarized light can be decomposed into components parallel and perpendicular to the ordinary crystal axis. Since the components are subject to different refractive indices, both the orientation of the polarization vector and as the phase of the light wave will have changed after propagation through the crystal. Both effects are subsumed under the term phase retardance. Well-known applications of these effects are $\lambda/2$ or $\lambda/4$ waveplates. The additional advantage of liquid crystals is their permanent dipole moment, allowing the variation of the orientation of the crystal and, thus, the amount of the induced phase retardance by the application of an external field.

A sketch of the principle design of a mask is depicted in figure 2.12. The liquid crystal layer is embedded between a brushed glass substrate and an electrode
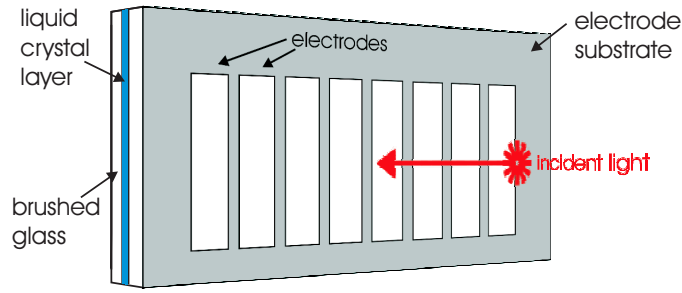
Figure 2.12: The design of a liquid crystal mask. The crystals are located in the grey area, whereas the voltage is applied on the different electrodes. Since the laser radiation is perpendicular to their surface, transparent electrode material is required.

substrate. The brushed glass determines the orientation of the crystal molucules if no electric field is applied. As the electrodes are to be independently driven, they are electrically isolated among each other by a gap of several micrometers.

There are several possible arrangements that can be employed for phase and amplitude shaping [WLPWI92]. The device used in our experiment, described in chapter 6, has an arrangement of two subsequent liquid crystal masks, placed between two polarizers (see figure 2.13), of which the first one only transmits the horizontally polarized component of the incident light. The ordinary axes of the crystals of the following masks have an angle of 45 ° with respect to the incoming light, but of 90 ° with respect to each other, meaning that the applied phase retardance of both mask is opposite. The exit polarizer transmits only the horizontally polarized component of the phase modulated pulse. The modulated electric field can be expressed as a function of the phase retardances of both masks by [WN95]

$$E_i^{out} = E_i^{in} \cos\left(\frac{\Delta\Phi^{(A)} - \Delta\Phi^{(B)}}{2}\right) \, \exp\left(\frac{i(\Delta\Phi^{(A)} + \Delta\Phi^{(B)})}{2}\right). \qquad (2.46)$$

From equation (2.46) one obtains the transmission filter T of the shaper

$$T = \cos^2\left(\frac{\Delta\phi^{(1)} - \Delta\phi^{(2)}}{2}\right) \qquad (2.47)$$
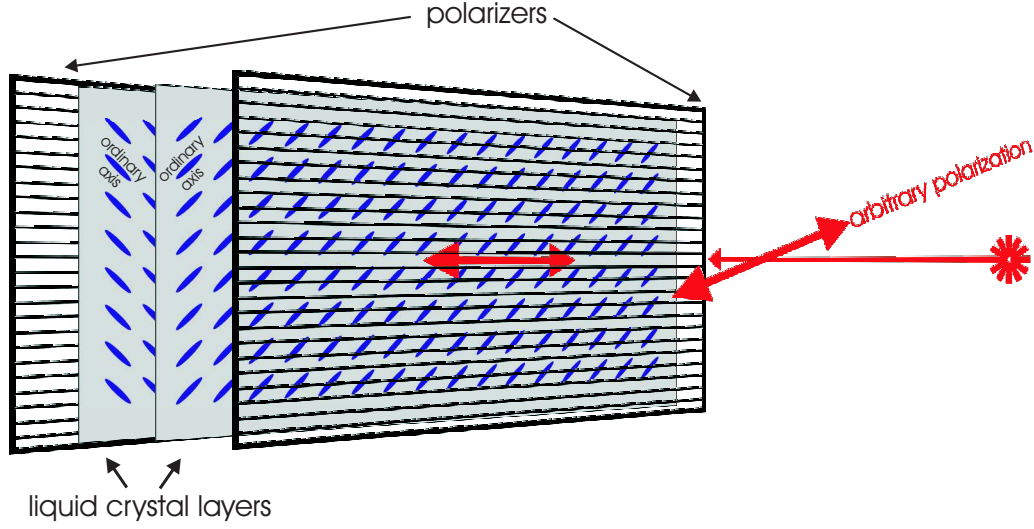
Figure 2.13: The arrangement of the polarizers and crystal masks of the pulse shaper used in our experiment [Cam04]. The first polarizer only transmits the horizontal component of arbitrarily polarized light.

and the phase filter ψ

$$\psi = \frac{\Delta\phi^{(1)} - \Delta\phi^{(2)}}{2}. \tag{2.48}$$

According to equation (2.47), pure phase modulation ($T = 1$) is achieved by the application of the same phase retardance to both masks.

The effects of pixelation

The modulation function $R(\omega)$ in equation (2.45) assumes a continuously varying phase function. However, in a real experiment the shaper only has a finite number of electrodes so that the modulation function is approximated by the device and equation (2.45) must be replaced by [WLPWI92]

$$M(\omega) = \left(H(\omega) \sum_{n=-N/2}^{N/2-1} \delta(\omega - n\delta\omega) \right) \mathrm{rect}\left(\frac{\omega}{\delta\omega}\right). \tag{2.49}$$

Then, the influence of the pixelated mask on the *temporal* pulse shape is found by Fourier-transformation [WLPWI92]

$$E_{out}(t) = E_{in}(t) * \left[\left(\frac{1}{\sqrt{2\pi}} \sum_{m=-\infty}^{\infty} h\left(t - m\frac{2\pi}{\delta\omega}\right) \right) \text{sinc}\left(\frac{\delta\omega t}{2}\right) \right], \qquad (2.50)$$

where $h(t)$ is the Fourier-transformation of $H(\omega)$. Equation (2.50) shows that the frequency stripes $\delta\omega$ lead to a series of replica pulses at a temporal distance of $\Delta t = \frac{2\pi}{\delta\omega}$. Because of the modulation by the sinc-function $(\text{sinc}(\text{x}) = \frac{sin(x)}{x})$ their intensity quickly goes to zero and only the first replica pulses are of importance.

Similarly, further replica pulses arise from (i) the finite extension of the frequency components in the focus of the cylindric lenses (see equation (2.24)), and from (ii) the gaps between the electrodes on the shaper mask, which behave as thin inactive pixels, subject to no electric field: the phase of the light passing through these gaps remains unchanged.

Apart from these geometric considerations, one has to consider that the application of phase functions $\Phi = \text{k } 2\pi$, k ϵ $\mathbb{Z}$, have the same effect. This means that the maximum phase shift between two adjacent pixels on the shaper mask is, therefore, $\Delta\phi = \pi$. This limits the phase jumps that can be implemented, as illustrated below in the case of a linear and quadratic phase function.

A linear phase function As already addressed in paragraph 2.1.1, the application of a linear phase function on the shaper mask

$$\psi(\omega) = b_1(\omega - \omega_0) \qquad (2.51)$$

causes a simple delay of the original laser pulse, and the coefficient b_1 determines the pulse delay. This linear function is represented by the discrete function

$$\psi_n = \delta\omega b_1 \left(n - \frac{N}{2} \right) \qquad (2.52)$$

on the shaper mask, where N is the number of its pixels. The condition $\Delta\Phi \leq \pi$ for the maximum phase shift between two pixels requires $\delta\omega b_1 \leq \pi$, yielding a maximum delay of

$$b_1^{max} = \frac{\pi}{\delta\omega}. \tag{2.53}$$

Note that the maximum possible delay is half of the temporal distance of the replica pulses. This can be easily understood, since in this case the original and the nearest replica pulse have the same intensity and cannot be distinguished anymore [WLPWI92]: the 2π indetermination has been transferred to the indetermination between the replica pulses.

A quadratic phase function - the linear chirp A basic phase modulation is the application of a quadratic phase, *i. e.* the application of a linear chirp. In the case of the Teramobile experiments, it is a indispensable parameter, allowing the variation of the filamentation onset. The quadratic phase function is expressed by

$$\psi(\omega) = \frac{1}{2}b_2(\omega - \omega_0)^2, \tag{2.54}$$

which is represented on the shaper mask by

$$\psi_n = b_2\delta\omega^2 \left(n - \frac{N}{2}\right)^2. \tag{2.55}$$

This leads to

$$b_2 = 2\frac{\delta\psi}{\delta\omega^2}. \tag{2.56}$$

The maximum linear chirp is determined by a phase jump of π from one pixel to another at both edges of the shaper mask, as the gradient of the quadratic function is at its maximum there. This leads to

$$b_2^{max} = \frac{2\pi}{(N-1)\delta\omega^2}. \tag{2.57}$$

Those estimations point out that generally a pulse shaper mask with a pixel number as high as possible is desirable in order to maximize the steepness of the phase gradients.

2.5 Discharges in long air gaps

As this topic is normally not among the subjects taught to laser physicists, this section gives an introduction into the physics of high-voltage discharges. At first sight, the approach to this subject appears to be quite easily comprehensible, as the phenomenon of lightning has probably been one of the first phenomena with which human beings were engaged, and even a laboratory discharge is an impressive and tangible phenomenon. However, if one begins to explore the underlying processes, this clearness is lost shortly after, and one has to admit that some of the fundamental processes are up to now not even qualitatively understood. This is on the one hand probably due to the expensive and time-consuming setups that often demand designs for very special purposes, *e. g.* lightning protection of airplanes, meaning that conclusions can be drawn for only particular experimental conditions. On the other hand, the physical mechanisms depend strongly on these conditions (polarity, electrode shape and distance, properties of the applied voltage), which makes the scientific progress so difficult in this domain. This is, for example, expressed by the multitude of different kinds of discharges, such as glow, corona, arc or spark discharge. The latter type will be the subject of the investigations of this work.

The following paragraphs will introduce the different processes involved in the development and propagation of discharges in long air gaps. Special attention is turned to strongly non-uniform gaps and fast rising negative voltage pulses, which have been the configurations used in the experiments reported in this work (chapter 5). *Negative* discharges mean that the high-voltage electrode is negatively energized. Besides, all experiments in this work have been carried out in this configuration. An important term is the *breakdown* of a gap. It is defined as the state, at which the electrical circuit of the gap is initiated.

The reader may be referred to the book "Gas Discharge Physics" of Y. P. Raizer [Rai97] for a more detailed and comprehensive discussion of all discharge

processes.

2.5.1 The Townsend ionization

A first mechanism for the discharge development was proposed by Townsend in 1900 [Tow00], who proposed that the discharge is driven by an electron avalanche, as it is shown in figure 2.14. The first electron is accidentally ejected from the cathode, *e. g.* by cosmic radiation, accelerated by the external electric field and hits a molecule afterwards, causing its ionization. If the field is sufficient, this ionization initiates the electron avalanche leading to breakdown. The growth of the free electron density N_e can be expressed as

$$dN_e = \alpha(E_{ext})N_e dx, \tag{2.58}$$

where α is the ionization coefficient that depends on the external electric field E_{ext}. This leads to the condition $\alpha(E_{ext}) \geq 1$ for an electron avalanche to be initiated. At standard temperature and pressure conditions (273 °K, 1 atm) the condition is reached for $E_{ext} \approx 30$ kV/cm in air. As a matter of fact, a field as high as 30 kV/cm is necessary for breakdown in gaps with a uniform field distribution in air.

However, soon after Townsend's publication, mainly two observations necessitated modifications of his theory. The first contradiction is the expected discharge velocity. As the ionization within the whole gap is driven by electron impact, the velocity must be on the order of the drift velocity of electrons v_e
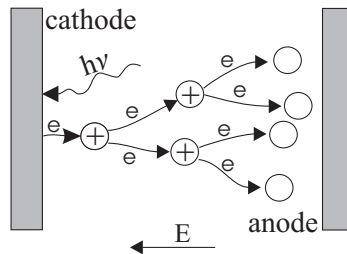

Figure 2.14: The Townsend mechanism.

in air, which is $v_e \approx 10^4$ m/s [NB37]. If the theory were valid for lightning, too, the stroke would need about 0.3 s to bridge the distance between the cloud at a typical altitude of 3 km and the ground, meaning one would see its propagation with the naked eye.

The second problem of Townsend's theory is that it always requires an electric field of 30 kV/cm, but in the first decades of the 20th century the first laboratory high-voltage experiments showed that the gap breakdown could occur at considerably lower voltages. For example, typical values of the electric field in the atmosphere during thunderstorms are on the order of 10 kV/cm [Uma01]. Therfore, another process was proposed by Loeb [Loe36] and Meek [Mee40] in the 1930s, governing the development process in non-uniform gaps.

2.5.2 The streamer

Loeb and Meek proposed that the electrons, produced by the avalanches, cause a distortion of the electric field between the electrodes, which allows to sustain the ionization process even in low external fields. This ionization wave is called a *streamer*.
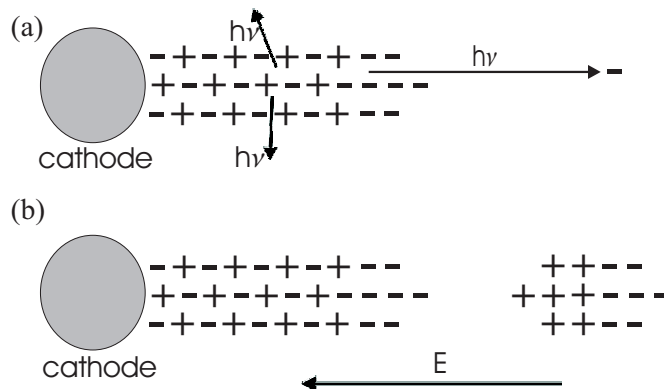

Figure 2.15: Sketch of the propagation of a negative streamer. The recombination of electrons and positive ions that result from the preceding propagation step creates photons (a) that accidently ionize a molecule in front of the streamer head, resulting in subsequent streamer propagation (b).

The propagation of a negative streamer is depicted in figure 2.15. Similarly to the Townsend mechanism, subsequent propagation steps are triggered by photoionization, however, the necessary photons originate from recombination processes of the preceding propagation step. The streamer velocity is considerably faster than the drift velocity of the electrons and has been measured to be in the range of 10^5 - 10^7 m/s [BR98], meaning that the upper bound of the observed velocity is already about 10 % of the speed of light.

In their original publications, Loeb and Meek regarded the streamer mechanism as sufficient for the breakdown of a gap, as they proposed that the streamer were a highly conductive channel. Yet, spectroscopic measurements revealed that streamers undergo "cold" ionization, and it is now generally accepted that there is only a significant electron density in the vicinity of the streamer head, where the ionization takes place. This is mainly due the fast attachment of free electrons to the oxygen molecules of the air, resulting in O_2^--ions.

This attachment to oxygen molecules, to which also electrons of the laser filament are subject, is a common thread of the experiments of this work. Therefore, the time dependence of the free electron density has been calculated from the following rate equations [YZL+02, ZDWE95]

$$\frac{\partial N_e}{\partial t} = \alpha N_e - \eta N_e - \beta_{ep} N_e N_p \tag{2.59}$$

$$\frac{\partial N_p}{\partial t} = \alpha N_e - \beta_{ep} N_e N_p - \beta_{np} N_n N_p \tag{2.60}$$

$$\frac{\partial N_n}{\partial t} = \eta N_e - \beta_{np} N_n N_p, \tag{2.61}$$

where $N_{e,p,n}$, respectively, denotes the density of electrons, positive ions and O_2^--ions. The necessary coefficients are collected in table 2.2.

These values are used by the majority of authors discussing the application of ultrashort laser pulses to the control of discharges [LFVC+99, YZL+02, ZDWE95, ZJD+06], assuming an electric field of E = 5 kV/cm.

This system of differential equations can easily be solved and figure 2.16 shows

α	7.4×10^4 s^{-1}
β_{ep}	2.2×10^{-13} m^3/s
β_{np}	2.2×10^{-13} m^3/s
η	2.5×10^7 s^{-1}

Table 2.2: The coefficients used for the calculation of the electron density [ZDWE95].

the dependence of the electron density as a function of time for two different initial values of N_e. The figure reveals that, even when the air has nearly been entirely ionized ($N_{N_2,O_2} \approx 10^{19}$ cm^{-3}), within 1 µs the electron density decreases by 10 orders of magnitude. Therefore, another process is necessary to provide a sufficient heating, maintaining the conductivity of the air. Due to the insulating tail of the streamers, a pure streamer breakdown is only possible in extremely high electric fields under low atmospheric pressure [BR98].
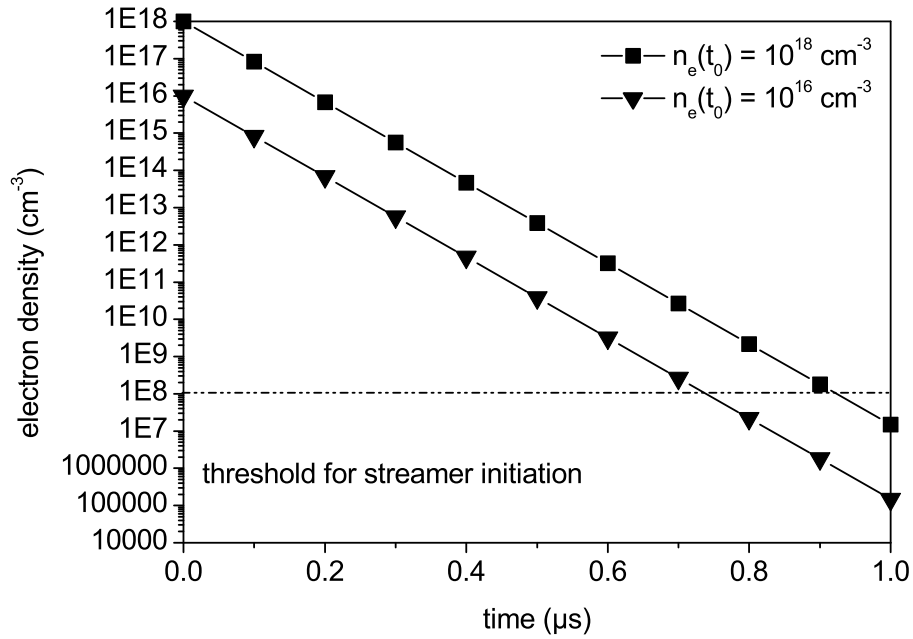

Figure 2.16: Calculated electron density as a function of time for two different initial electron densities. The threshold for streamer initiation is $N_e \approx 10^8$ cm^{-3} [BR98].

2.5.3 The leader

The process responsible for the heating is the so-called leader. A possible heating mechanism, which is commonly accepted in the literature, was proposed by Gallimberti [Gal79]. He proposed that the electrons of the continuously produced streamers, appearing in a thin bundle in the vicinity of the high-voltage electrode, lead to an increasing current, which heats up the air as a result of energy dissipation. When a temperature of 1500 °K is reached, the detachment rate becomes equal to the attachment rate, and a self-sustaining current is possible. The model of a leader is depicted in figure 2.17.

Within the leader channel the temperature is above the threshold of 1500 °K, and a conducting channel is created and maintained. The leader head is a transition region, where the air temperature is heating up, enabling further leader propagation. According to Gallimberti's theory, the following equations drive the evolution of the temperature of the air within the streamer-to-leader transition region [Gal79]

$$\frac{d}{dt} \left(\tfrac{7}{2} k T_h n_h \pi a^2 \right) = (f_e + f_k + f_t) E I + \frac{\pi a^2 (\epsilon_v(T_v) - \epsilon_v(T_v))}{\tau_{vt}} \quad (2.62)$$
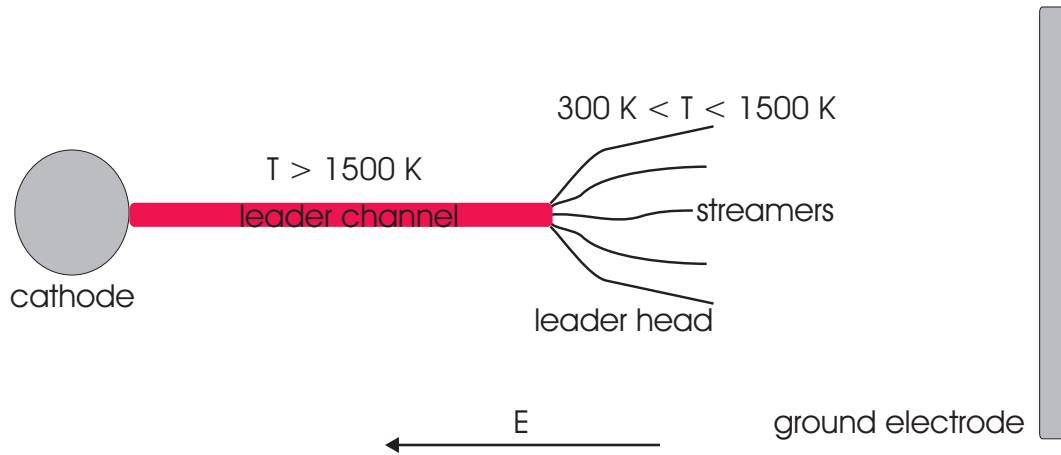

Figure 2.17: Sketch of a leader according to Gallimberti's model for the streamer-to-leader transition. In the leader channel the temperature exceeds 1500 °K, allowing a conductive channel. The leader head consists of a streamer bundle, in which the air is heated up.

$$\frac{d}{dt} \quad (\pi a^2 \epsilon_v) \quad = f_v EI - \frac{\epsilon_v(T_v) - \epsilon_v(T_h)}{\tau_{vt}} \pi a^2, \tag{2.63}$$

where n_h is the density of neutrals, T_h and T_v their translational and vibrational temperatures, a is the radius of the streamer bundle, ϵ_v is the vibrational energy per unit volume and $f_{e,k,t}$ are the fractions of the energy EI that is transferred to the molecules in the form of electronic, rotational, translational and vibrational excitation.

These equations show that the simulation of the streamer-to-leader transition is not trivial, and, *a fortiori*, the calculation of the influence of the laser filament is beyond the scope of this work. Yet, the results of our expriments may be qualitatively understood in the scope of Gallimberti's theory.

2.5.4 The different steps of a spark discharge

After the introduction of the basic mechanisms of the streamer and leader this paragraph presents the most important steps during the development of a long spark discharge in non-uniform fields.

When the negative high-voltage is applied to the gap, the first charges are injected by the *first corona*. Although one would not refer to as a Townsend discharge, the underlying ionization mechanisms are the same, as the corona occurs when the electric field in the vicinity of the electrode reaches 30 kV/cm. The electric field around a small spherical electrode can be estimated as

$$E(r) = \frac{U r_e}{r^2}, \tag{2.64}$$

by assuming that the high-voltage electrode is a sphere-capacitor with its counterpart in infinity. r_e is the electrode radius and U the applied voltage. For example, for an electrode radius of $r_e = 4$ cm, a field of 30 kV/cm is already reached at $U = 120$ kV. The electrons of the first corona screen the electric field in the vicinity of the electrode, decelerating the discharge development process for small electrode radii and fast rising voltage pulses.

Starting with the onset of the first corona, the streamers propagate into the gap. It is assumed that the gap breakdown is initiated when the streamers have reached the ground electrode. The moment of the arrival of the streamers at the ground electrode is called the *final jump*, as it is accompanied by a steep current rise that is injected into the gap. The final jump of a negative discharge always initiates a positive leader at the ground electrode, and its connection to the negative electrode leader initiates the breakdown of the gap.

The onset of the electrode leader depends strongly on the experimental conditions, especially for fast rising voltage pulses its onset is postponed by the shielding effect of the first corona and is normally observed just before the initiation of the final jump [Gro81]. However, even if no gap breakdown occurs, an electrode leader is initiated and propagates into the gap. The graphic on the next page (figure 2.18) may clarify the different steps of the discharge development in a nonuniform gap.
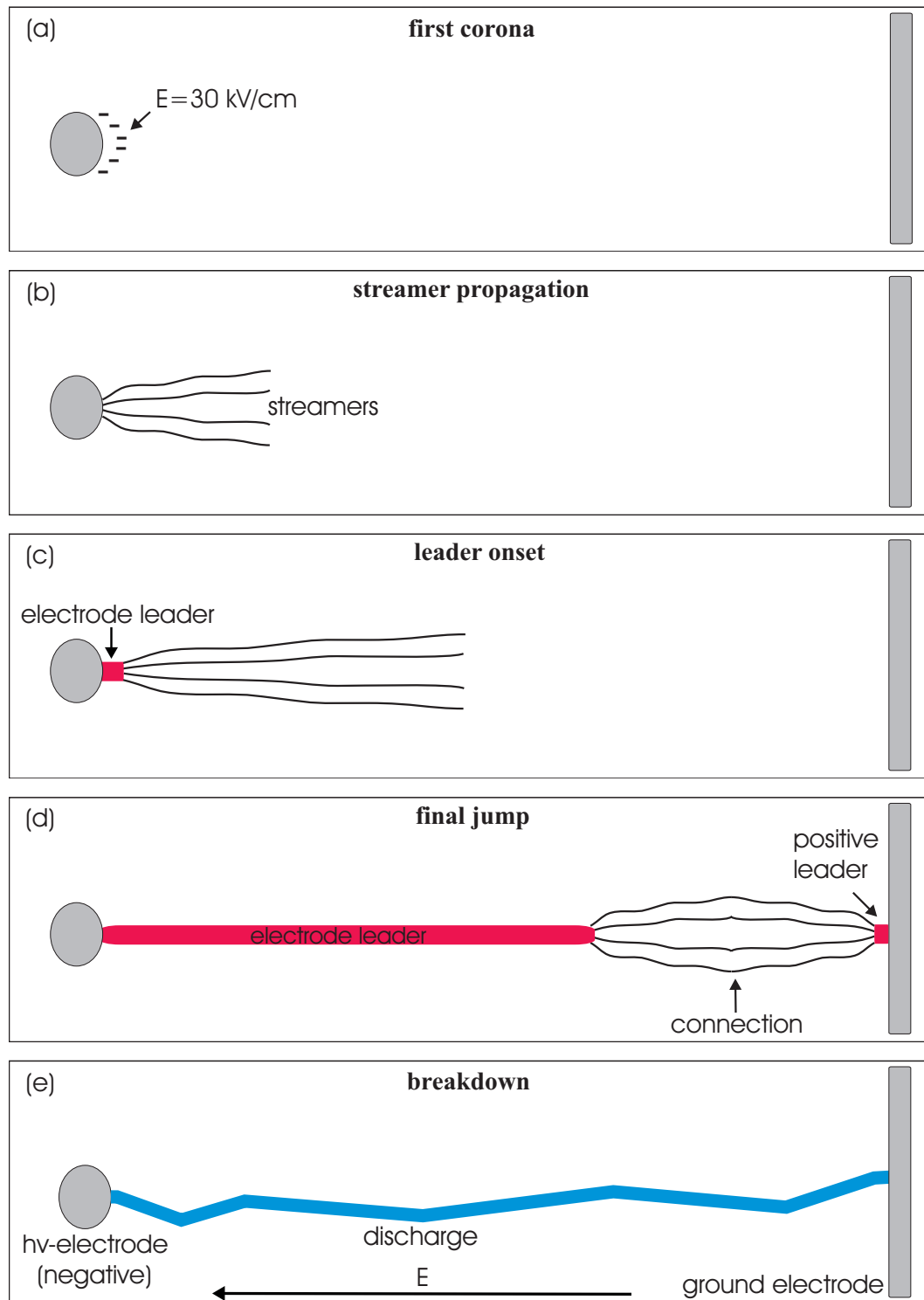
Figure 2.18: The different steps of a high-voltage discharge in a highly nonuniform gap. (a) onset of the first corona, (b) streamer propagation, (c) leader onset, (d) final jump and (e) the breakdown of the gap.

2.5.5 Negative discharges and the occurrence of space-leaders

Laboratory studies on negative discharges in the 1970s [GS76, GHJR75] revealed that the leader propagation of a *negative* leader may under certain conditions be even more complex than described above. It was observed that in gap distances of more than 2 m, the negative leader does not propagate continuously towards the ground electrode, but occasionally a leader, the so-called *space-leader* occurs within the gap (see figure 2.19), which starts propagating into the opposite direction towards the cathode. There, it connects to the negative electrode or the emerged electrode leader. The most comprehensive study on space-leaders was done by "Les Renardières" Group in 1981 [Gro81], and more recently by Ortega *et al.* [ODG+94] and Reess *et al.* [ROG+95].

A qualitative explanation for this phenomenon was proposed by Hutzler [Gro81] in the Renardières' publication. This interpretation is based on a different propagation mechanism of the negative and positive streamers. In both cases (see figure 2.15) new electrons are produced by photoionization, however, in the case of a positive streamer a new avalanche may be initiated directly within the streamer head, due to the high electric field caused by the *positive* ions. In the case of a negative streamer, a sufficiently high field exists only *in front* of
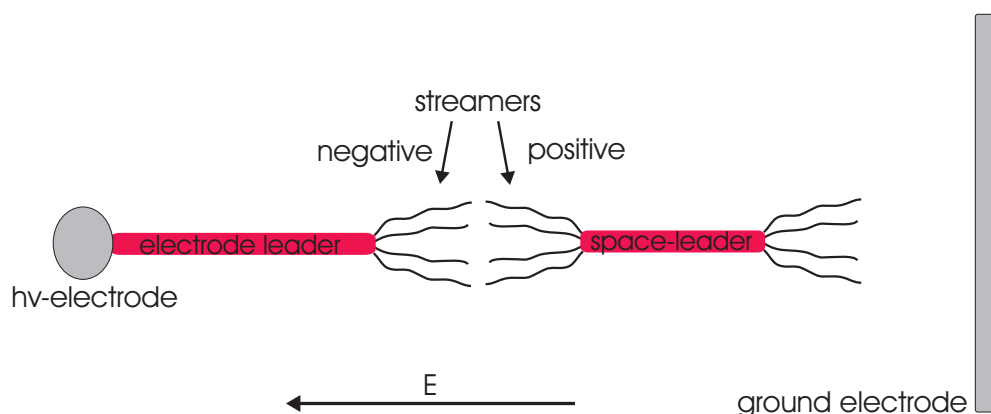
Figure 2.19: Illustration of a space-leader discharge.

the streamer head, as it is shown in figure 2.15. This leads to an isolated plasma region, called the *space-stem*, in which the external electric field causes a charge separation of the electrons and positive ions. This positive net charge, then, leads to the formation of positive streamers, branching towards the cathode, and, under certain conditions, this may lead to the initiation of a (positive) leader that propagates towards the cathode. On its anode directed side, also a negative leader develops, and the whole structure is called a space-leader.

A comprehensive modeling of the formation of a space-leader still does not yet exist, but particular results have been presented by Bacchiega *et al.* [BGB$^+$94].

3 The Teramobile laser system

Figure 3.1: The "Teramobile" container next to the faculty of physics of the "Freie Universität Berlin". The small hole serves as the beam exit, while the big one is normally used for the telescope detection.

Most of the experiments described in this work have been performed with the Teramobile laser system (see section 4.2, chapters 5 and 6). As it has already been the subject of a multitude of PhD-theses [Méj05, Rod04] and publications [KRM+03, WRK+02] that give a comprehensive description, only a brief overview of the Teramobile facility is presented in this chapter. The laser systems of those experiments that have not used the Teramobile (section 4.1 and chapter 7) are described in the corresponding "Experimental Setup"-section.

The basic idea that has led to the construction of the Teramobile in early 2000 was to provide a *mobile* laser system that takes advantage of the nonlinear optical effects described in section 2.2, in particular filamentation and con-
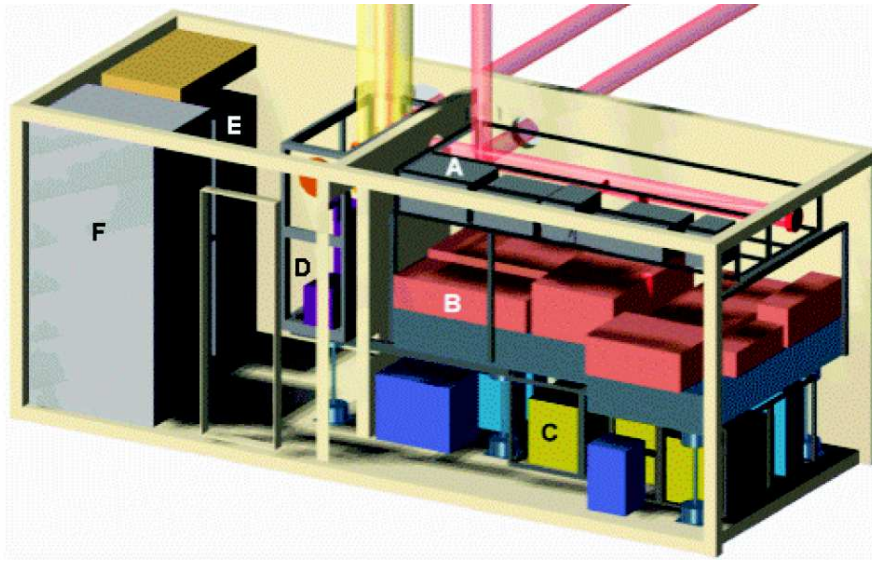
Figure 3.2: Sketch of the layout of the Teramobile. A - sending optics, B - laser table, C - power supplies and cooling devices for the lasers, D - detection unit, E - workstation for detection, F - air-condition/main electricity board.

tinuum generation, in order to introduce a novel "white-light" LIDAR technique. First successful atmospheric experiments had been performed at the "Friedrich-Schiller-Universität Jena" in 1997 by Wöste *et al.* [WWW+97], using a tabletop TW-femtosecond laser system that was propagated into the sky (see figure 1.1).

The whole Teramobile system is installed in an altered standard shipping container (see figure 3.2) that is divided into two sections. One room contains the laser table, devices and cooling systems, while the second room was designed to integrate various detection systems. An external cooling unit provides a closed-loop water circuit that acts as a secondary cooling unit for the inner cooling system that is directly connected to the laser heads and crystals.

Because of the closed-loop water circulation, an electric power supply, providing a 3 x 64 A connection, is sufficient in order that the laser can be operated. Moreover, during the campaign in the mountains of New Mexico (section 4.2) the laser even was self-sustainingly driven by a diesel power generator. This permits to operate the Teramobile in almost any place in the world.

3.1 Generation of TW-femtosecond pulses

High-power femtosecond laser pulses are produced by the generation of low energy pulses in a femtosecond oscillator and then by amplifying them by one or multiple, subsequent amplifier stages. One problem occurring with the amplification of short pulses is their high peak intensity, meaning that the damage threshold of the optical components is reached quickly. This problem is solved by the so-called "Chirped Pulse Amplification" (CPA) [MSB$^+$88, SM85, Tre69] technique. The original femtosecond pulse is strechted to several hundred picosends by a strechtcher grating setup. This lowers the peak intensity of the pulse by a factor ≈ 1000 and the temporally stretched pulse may now be amplified. The different steps of the amplification of femtosecond pulses are shown in figure 3.3. The low energy, ultrashort pulses are produced in the
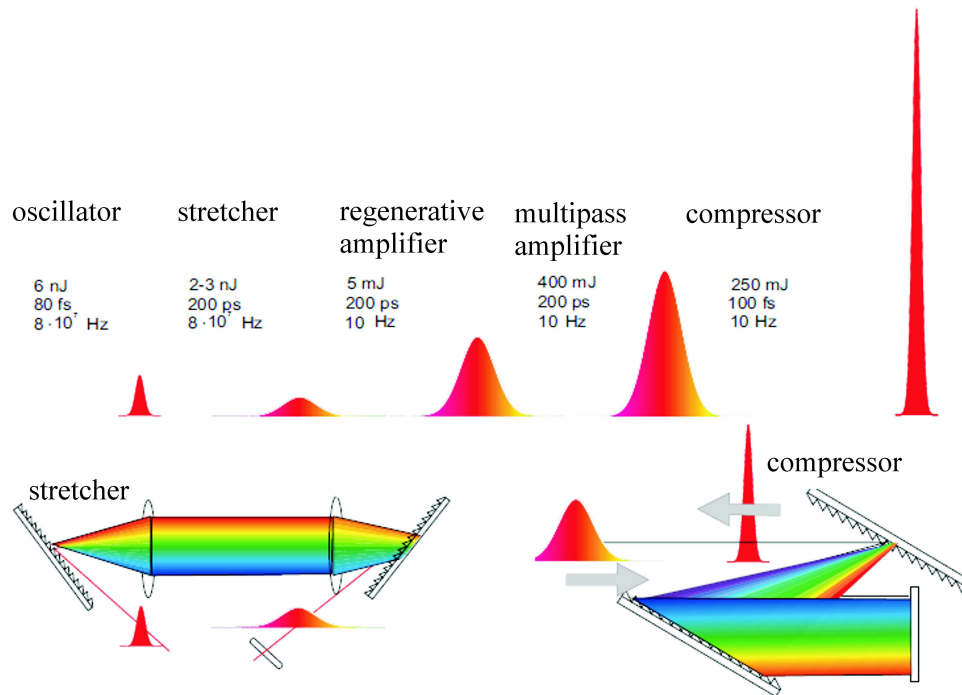

Figure 3.3: The different stages of the amplification of an ultrashort laser pulse in a terawatt laser system with typical values for the pulse energy, pulse duration and repetition rate.

oscillator. The ultrashort pulse duration is achieved by the Kerr-lens mode-locking technique (KLM) [SSP91, SKS91], where the Ti:Sapphire crystal itself acts as mode-locker owing to the optical Kerr-effect within the laser medium. The femtosecond pulse, then, is stretched and passes through a regenerative amplifier. The principle of regenerative amplification is to inject the seed pulse into a laser cavity and amplify it, until saturation is achieved. The extraction is performed by a Pockels-cell, where a high-voltage is applied between two electrodes on both sides of a birefringent crystal, through which the pulse is propagating in the cavity. Depending on the applied voltage, the light polarization is turned so that the pulse may be extracted by a polarizer plate. Pockels-cells have a very short response time on the order of several nanoseconds, shorter than a roundtrip of the pulse in the cavity, which is typically 13 ns for a meter-scale cavity. This "pulse-picking" of the oscillator pulses is one cause for a jitter of amplified laser pulses. Another source is the instability of the pump lasers, which is in the case of the Teramobile on the order of a few tens of nanoseconds.

The regenerative amplifier, then, is followed by one or more multipass-amplifiers, in which the pulse is sent several times (typically 3 - 8) through the laser crystal by a specific mirror arrangement. Finally, the pulse is recompressed and leaves the laser chain. One has to remark that the beam diameter has to be increased after each amplification because of the damage threshold, considerably affecting the costs of an amplified laser system due to the necessary large optics. Based on this general description of a femtosecond laser, the next section describes the particular chain of the Teramobile.

3.2 The laser chain of the Teramobile

Figure 3.4 gives an overview of the laser chain of the Teramobile.
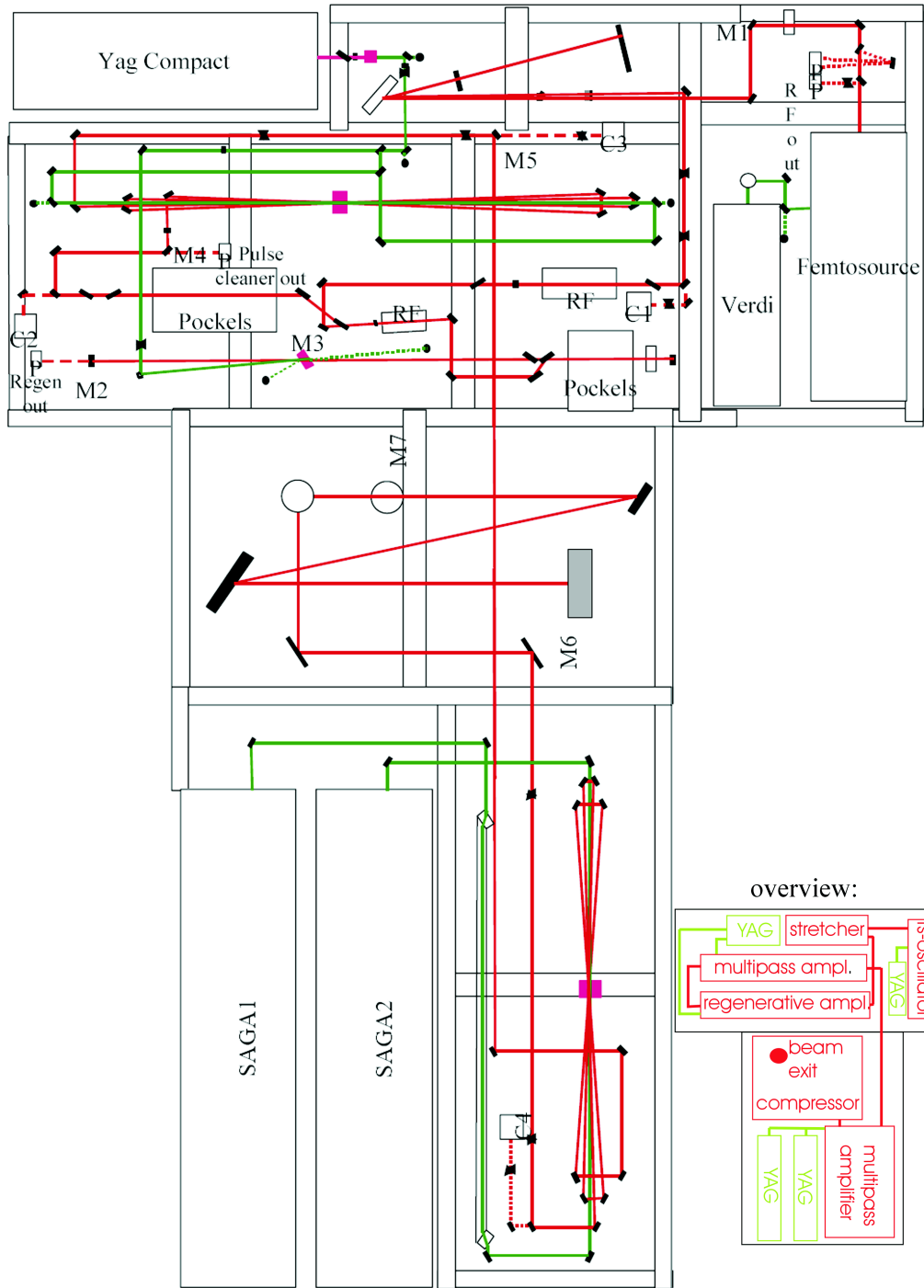
Figure 3.4: Scheme of the Teramobile laser chain (see text). The green lines represent the beam of the pump laser and the red lines the beam of the femtosecond pulses. The inset gives an overview of the installed devices.

The femtosecond pulses are produced by the oscillator ("Femtosource"), which is pumped by a cw-Nd:YAG laser ("Verdi"), providing pulses of 70 fs duration and an energy of a few nJ at 80 MHz. These pulses are injected into the grating stretcher that elongates the pulses to several hundred ps. One regenerative and a four-pass amplifier elevate the pulse energy to about 40 mJ. The repetition rate is now 10 Hz due to the Nd:YAG pump laser ("Compact"). The last four-pass amplifier that is pumped by two Nd:YAG lasers ("SAGA1" and "SAGA2") providing 800 mJ at 532 nm, delivers pulses with an energy of up to 600 mJ before compression. The final energy of the compressed pulses reaches up to 250 mJ. One grating of the compressor is mounted on a motorized translation stage that allows the application of a chirp during compression, leading to initial pulse durations between 70 fs and 2 ps. Then the beam can either be sent outside in a parallel configuration with a beam diameter of approximately 3 cm, or enter a telescope expanding the beam to about 15 cm. The range of its geometric focus can be varied by a motorized translation stage between less than 10 m and a slight beam divergence.

Exit ports in the wall (see figure 3.1) and the roof of the container allow to send the beam either horizontally or vertically. The chirp, the focus of the telescope and a mechanical laser shutter can be remotely controlled via a computer

center wavelength	793	nm
bandwidth	20	nm
minimum pulse duration	70	fs
maximum pulse energy	350	mJ
peak power	5	TW
repetition rate	10	Hz
range of initial pulse duration by application of a linear chirp	70	fs - 2 ps

Table 3.1: Main specifications of the "Teramobile" laser system. Note that the values mentioned in the text represent typical everyday experiences and are, therefore, slightly different from the specifications.

network, which was of indispensable use during the high voltage experiments, during which no operator is allowed to stay in the laser container. Table 3.1 collects the main specifications of the Teramobile laser.

4 Filamentation under adverse ambient conditions

As the Teramobile offers the opportunity to go beyond laboratory experiments, the influence of real weather conditions on the beam propagation, as well as on the system operation itself, is of special interest. In addition, applications as real lightning experiments will compulsorily take place under rainy and windy conditions. Therefore, it is one of the main objective of the research in this subject area to investigate how the formation and propagation of filaments is influenced by particular ambient conditions.

In this regard, we conducted two experiments, investigating the filamentation in turbulent air and in real, adverse atmospheric conditions that are being described in the following.

4.1 Filaments transmitted through turbulent air

The investigation of filamentation in turbulent air is of special interest, since the wave-front distortions induced by the tubulence may perturbate the balance between the self-focusing effect, which also arises from intensity gradients within the beam profile, and the plasma formation. Thus, one aim of turbulence experiments is to determine the threshold at which the formation of filaments is no longer possible and to compare it with the amount of turbulence that

may be encountered in the atmosphere.

Another parameter to be investigated is the pointing stability of the filament within the surrounding beam, since, for example, LIDAR experiments would undergo severe constraints if the pointing stability of the filament behaved very differently from that of classical light.

Several groups already investigated particular aspects of turbulent influences on the propagation of femtosecond pulses [KKT$^+$99, LKG$^+$02, Rob97]. Chin *et al.* [CTY$^+$02] investigated the influence of a moderate turbulence on the pointing stability of the filament, but up to now a characterization of the pointing stability and formation probability at rather strong turbulences had been missing in order to test out the limits of filamentation. Therefore, as a first step, we have investigated the influence of highly turbulent air on the formation and propagation of the filament in the laboratory.

The experiment has been published in *Optics Letters* [AMK$^+$05].

4.1.1 Experimental setup

Figure 4.1 shows a sketch of the experimental setup. For this experiment, we used the laboratory laser of our group. The femtosecond pulses are produced by an oscillator of similar type as in the Teramobile followed by a regenerative and a multi-pass amplifier. During the experiment, the compressed pulses provided an energy of up to 8 mJ at 22.5 Hz and a pulse duration of about 100 fs. By changing the time of the pulse extraction from the regenerative amplifier, the pulse energy could be reduced to about 1 mJ in order to have a reference beam without filamentation. As a further independent reference a red 5 mW He-Ne-laser was aligned bypassing the turbulent region. The femtosecond beam was focused by a spherical mirror with a focal length of 5 m leading to a filament onset at 2.5 m downstream from the mirror and a filament length of 2 m. For the following discussion the filament onset was chosen as the origin of the
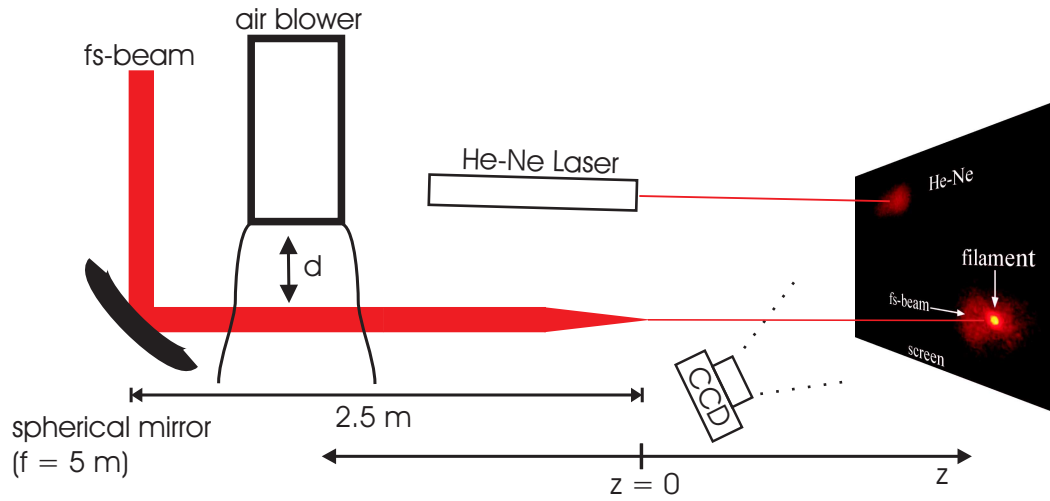
Figure 4.1: Sketch of the experimental setup. The laser beam is focused by a spherical mirror (f = 5 m) and the onset of the filament is chosen as the origin of the z-axis. The He-Ne beam is taken as an unperturbed reference beam.

z-axis.

The turbulence was generated by a hot air blower placed at different positions z perpendicular to the laser beam. The blower outlet had a diameter of 2 cm at 20° divergence angle, producing a flow with an estimated velocity of 20 m/s at temperatures up to 500 °C. This yields a Reynolds number of $\mathcal{R} \approx 15000$, which is well above the critical value $\mathcal{R}_{crit} \approx 3000$, and one can refer to as a *developed* turbulence. Distances between 1 mm and 2 m between the blower and the laser beam allowed to vary the magnitude of the turbulence.

If one wants to draw conclusions on atmospheric applications, an appropriate characterization of the laboratory turbulence has to be found. Atmospheric turbulence can be described by Kolmogorov's theory that defines two characteristic length scales:

- The *outer* scale of the turbulence $\mathbf{L_0}$.

- The *inner* scale $\mathbf{l_0}$, for which the energy of the turbulence fades to dissipation.

Typical values for atmospheric turbulences are on the order of a few mm for

l_0 and 10 - 1000 m for L_0 [CTY$^+$02]. For the given laboratory setup, l_0 is still on the same order of magnitude [CTY$^+$02], while L_0 can be estimated [Tat71] by

$$L_0 = 0.4H, \tag{4.1}$$

where H is the dimension of the turbulent region, *e. g.* 5 - 20 cm in this experiment.

The most important asssumption of Kolmogorov's theory is that, under the condition of a *developed* turbulence, the turbulent flow is locally isotropic for

$$l_0 \ll r \ll L_0. \tag{4.2}$$

The region in which equation (4.2) is valid, is called the *inertial* range. In this case, a relation between the standard deviation σ of the position of the laser spot on the screen and the so-called structure parameter C_n^2 can be derived [BKB04]

$$C_n^2 = \frac{\sigma^2 \phi^{1/3}}{2.91 l}, \tag{4.3}$$

where ϕ is the beam diameter and l the turbulent path. The value 2.91 is derived for plane waves and the structure parameter is defined by [Tat71]

$$C_n^2(r) = \frac{\langle (n(r) - n(r + \Delta r))^2 \rangle}{\Delta r^{2/3}}, \tag{4.4}$$

where r is the location of the perturbation, $n(r)$ the refractive index as a function of r and Δr is a length scale within the inertial range. Equation (4.3) assumes that $\phi \ll L_0$ as well as $l \ll L_0$, meaning that edge effects of the turbulent region have been neglected [Chi71, Tat71].

The pointing stability was measured by taking a series between 50 to 100 pictures of the beam profile on a screen, placed at a distance of $z = 7.6$ m. It was continuously moved in its plane during each acquisition in order that each filament hit a fresh screen region. The images were recorded by a commercial digital reflex camera, type Nikon "D70", using a macro lens with a focal length

of 105 mm, equipped with additional extension tubes with a length of 68 mm. This setup allowed a resolution of 10 µm/ pixel. The camera could be equipped with a RG780-filter (a list of all filters and their specifications used in this work can be found in appendix A) or a BG39-filter in order to block the supercontinuum and the fundamental wavelength, respectively.

4.1.2 Results and Discussion

As a first step, the pointing stability of the filamentary beam was compared to both the reference beam with reduced energy and the Helium-Neon-beam. All configurations showed the same pointing stability for a given turbulence, meaning that the nonlinear propagation does not lead to stabilization effects. Because of the analogous behavior of the three pointing stabilities, the femtosecond beam with the full energy itself was then used as a reference, while the Helium-Neon laser bypassed the turbulent region, serving as an indicator for perturbations not caused by the turbulence. The greatest of these perturbations was the movement of the laser spot on the rotating screen due to its small unevenness.

	pointing stability (μrad^2)	
	of unperturbed beam	in turbulence
whole beam	351	856
filament within the beam	243	224

Table 4.1: Standard deviation of the beam and the filament position releative to the beam on a screen at z = 2.6 m. The structure parameter of the turbulence was $C_n^2 = 6.6 \times 10^{-10}$ m$^{-2/3}$ placed at z = 1 m.

Table 4.1 compares the pointing stability of the whole beam with the filament position within the beam. The position of the filament was identified by calculating the center of gravity of the green layer pixels that exceed 70 % of the maximum intensity on the RGB-camera pictures. The corresponding magni-

tude of the turbulence was derived from the same pictures by determining, line by line, the pixel position where the intensity of the red layer reaches a predefined threshold. Then, the position of the beam has been defined by calculating the center of gravity of this area, after its edge has been smoothed. Comparing the values for the unperturbed and turbulent conditions in table 4.1, one can see that the filament position *within* the beam is remarkably unaffected by the turbulence.

Figure 4.2 displays the magnitude of the turbulence for three different filamentation probabilities as a function of the blower position z. The survival probability of a filament was determined from the green layer of the camera pictures as described above. Figure 4.2 shows a high probability of surviving the propagation through the turbulence if the filament has already developed ($z \geq 0$). This can be understood by comparing the influence on the refractive index induced by the turbulence with that of the changes of the nonlinear
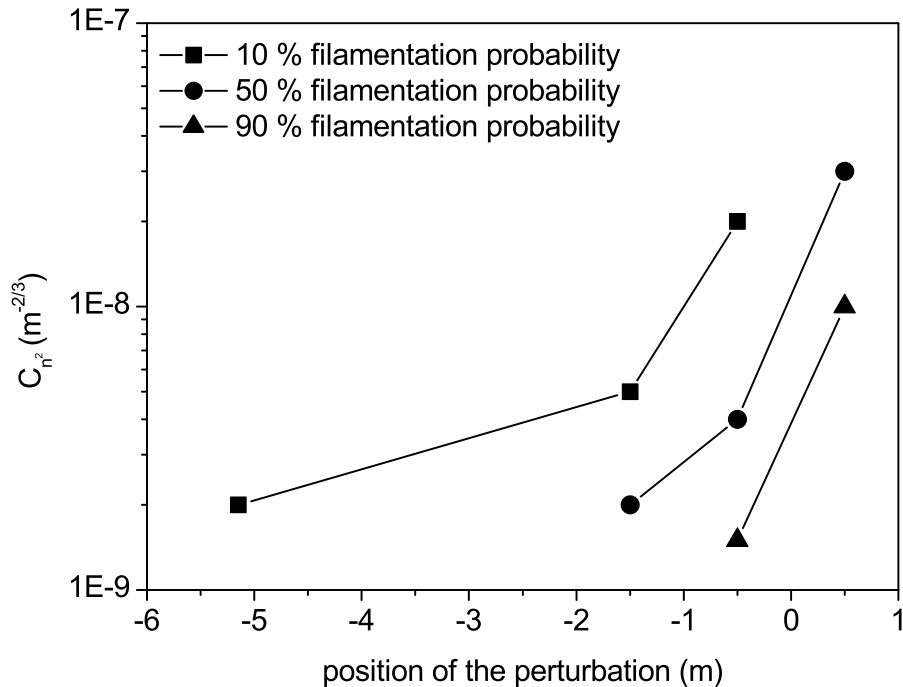

Figure 4.2: The structure parameter as a function of the position of the turbulent perturbation for a filamentation probability 10 %, 50 % and 90 %.

Kerr-effect. The latter influence can be expressed by

$$\nabla n_2 I/d, \qquad (4.5)$$

where $d \approx 100$ μm is the diameter of the filament and $I \approx 10^{14}$ W cm^{-2} the intensity within the filament. On the other hand, the influence of the turbulence can be estimated as

$$\nabla n_{Turbulence} \approx 9.1 \times 10^{-5} \times \frac{T_S}{T \Delta r}. \qquad (4.6)$$

The factor 9.1×10^{-5} stems from the Rank formula [Ran59] and T_S =288.15 K is the standard temperature. Inserting T = 500 °C as an upper limit and $\Delta r \approx 1$ cm, the comparison of the two influences leads to

$$\nabla n_{Turbulence} \approx 6 \times 10^{-3} m^{-1} \ll \nabla n_{filament} \approx 0.3 m^{-1}, \qquad (4.7)$$

meaning that refractive index changes due to the nonlinear Kerr-effect are nearly a factor of thousand greater than those of the turbulence. This is even more remarkable, as the turbulence encountered in the atmosphere is several orders of magnitude smaller than the turbulence which is investigated in this experiment. Typical values for the atmospheric structure parameter are in the range of $C_n^2 \approx 10^{-17} m^{-2/3}$ for weak turbulences and $C_n^2 \approx 10^{-9} m^{-2/3}$ as an upper limit.

However, if the turbulence is set upstream from the nonlinear focus, $i.$ $e.$ $z < 0$ in figure 4.2, the amount of turbulence preventing the formation of a filament decreases steeply. This can be understood by the effect that an early perturbation might persist and be amplified during the formation of the filament, owing to the nonlinear processes involved.

4.1.3 Conclusion

The influence of laboratory turbulence on the filamentation process has been investigated. Up to magnitudes possibly never encountered within the atmosphere, an already developed filament is able to survive the interaction with

the turbulence. An early perturbation significantly reduces this threshold that may be due to a magnification of the turbulent perturbation during nonlinear propagation. Furthermore, the stability of the filament position within the surrounding beam is not affected, making the white-light emission of the filament a suitable candidate for atmospheric detection applications, such as LIDAR.

4.2 Filaments in adverse atmospheric conditions

The previous section has shown that even strong laboratory turbulence is not a limiting factor for filamentation. However, turbulence is not the only perturbation with which a laser can be confronted in the real atmosphere. With regard to intended lightning experiments, the ability of a filament to develop and to propagate under rain conditions is another crucial point to be investigated [ASR+04, CBK+03]. Furthermore, the capability of the "Teramobile" to produce long filaments at distances on the order of kilometers [RBM+04], e. g. within thunderstorm clouds in a typical altitude of 3 km [Uma01], raises the question of the influence of reduced pressure on the filamentation process. In particular, because the atmospheric pressure affects the filamentation process in three different ways, by modifying the nonlinear Kerr-effect, the group velocity dispersion (GVD) and the plasma density in air (see chapter 2).

Both atmospheric phenomena have been approached during a campaign at the lightning research station of the "New Mexico Institute of Mining and Technology" (NMT). This installation in a mountainous region allowed to investigate the propagation of the filament under reduced atmospheric pressure and, additionally, under rain conditions.

4.2.1 Experimental Setup

The "Teramobile" has been installed on the Magdalena Mountain ridge in New Mexico, USA, at an altitude of 3230 m above sea-level, where the standard pressure is reduced to 0.67 atm. This corresponds to 6.8×10^4 Pa. The laser beam was propagated horizontally up to a distance of 325 m.

The beam profile has been characterized by taking pictures on a screen at different propagation distances, using a commercial digital camera, type Sony "DSC-F505V". The acquisition time was set to 1/8 s in order to photograph only a single laser pulse. The photos have been taken in three different configurations, by using a BG39-filter to record the supercontinuum, a RG780-filter for the fundamental wavelength and without filter. These picture sets have been used for analyzing the overall beam profile.

In addition, the beam profile has been registered with single shot burns on photographic impact paper, type Kodak "Linagraph 1895". As the filaments can be easily identified as small ablation spots on the paper, those burns have been used to evaluate the occurrence of filaments.

4.2.2 Results and discussion

Figure 4.3 shows photographs of the beam profile for three different distances. The filamentation process is identified by the high intensity spots that emerge at about 10 m and finally result in filaments. The observed multifilamentation
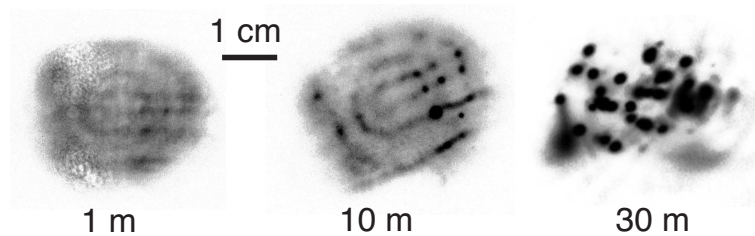

Figure 4.3: Pictures of the beam profile for three different propagation distances..
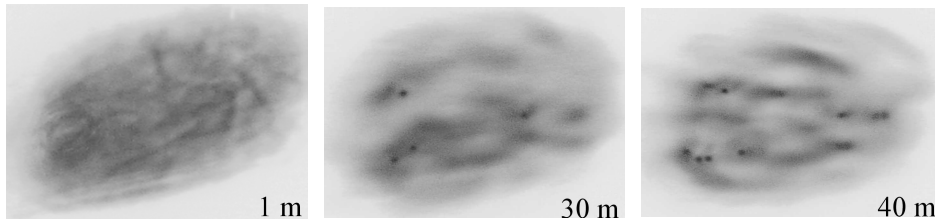
Figure 4.4: Beam profile of the Teramobile beam, taken at sea level at a distance of 1 m, 30 m and 40 m [BSL$^+$04].

is typical for laser beams far above the critical power [BSL$^+$04, Rod04], and the overall profile is qualitatively similar to the one at sea level [BSL$^+$04, MMA$^+$05], for which three examples at corresponding distances are shown in figure 4.4.

Figure 4.5 plots the number of filaments as a function of the propagation distance for different initial chirps. From the Marburger formula (2.34) one would expect an increasing distance to the nonlinear focus, but a pressure reduction of 30 % moves it only by an amount of 15 % upstream. This is below the range resolution of the measurements, which was about 5 m. Besides, for input powers far above the critical P_{crit} recent numerical simulations [CB06] predict a
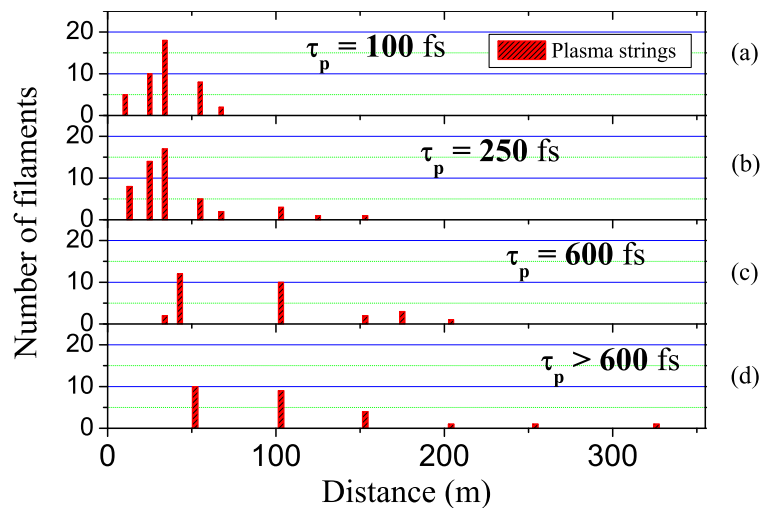

Figure 4.5: Number of filaments as a function of the distance for different chirps, corresponding to initial pulse durations of (a) 100 fs, (b) 250 fs, (c) 600 fs, (d) > 600 fs.
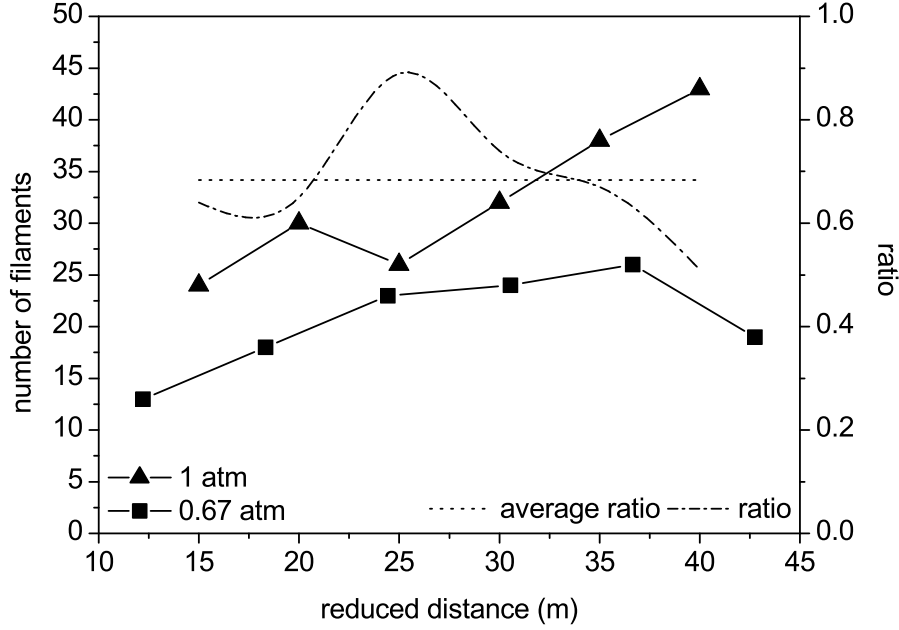
Figure 4.6: The number of filaments as a function of the reduced distance at 0.67 atm and 1 atm (taken from [MKY$^+$05]). The meaning of the reduced units for z are explained in the text.

pressure dependence $z_f \propto 1/p$ of the nonlinear focus, instead of $z_f \propto 1/\sqrt{p}$, which one would expect from the Marburger formula.

However, we observed that the filament length is unaffected by the lower pressure, as it is comparable to observations at sea-level [MMA$^+$05]. Especially, with regard to high-voltage and lightning experiments, the number of filaments is another key parameter, as it can be directly linked to the electric resistance of the whole filament bundle and, therefore, is a measure for its capability to trigger and guide discharges. Figure 4.6 compares the number of filaments as a function of the distance at 0.67 atm to earlier measurements at sea-level [MKY$^+$05]. The distance is expressed in reduced units, meaning $\hat{z} = z/\sqrt{p/p_0}$, where z is the propagation distance and p_0 the standard pressure. It reveals that the filament number at the high altitude is quite constantly reduced by 30 %, which corresponds well to the pressure reduction and, hence, to the higher critical power P_r.
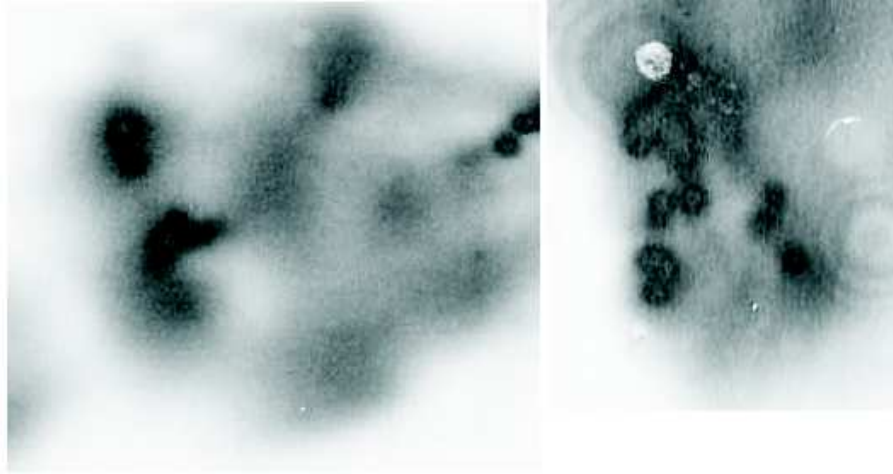
Figure 4.7: Single-shot beam impacts on photosensitive paper after 75-m propagation in dry air (left) and in rain.

Figure 4.7 compares two beam profiles that have been taken under dry and rain conditions at a distance of 75 m. The visibility was estimated to be 150 m, *i. e.* an extinction coefficient of 6.6 km^{-1}. Both impacts are qualitatively comparable, meaning that rain of this strength does not prevent the formation and propagation of filaments. Moreover, filaments could be observed up to a distance of 150 m.

During previous experiments [ASR$^+$04, MKY$^+$05] the filament had already formed, when it entered the rain zone, and its great robustness could easily be explained by the surrounding photons of the beam, delivering the amount of energy that is lost within the cloud [CBK$^+$03]. Yet, the conditions of this experiment are different, since the beam enters the rain just at the container exit, hence before the filament will have developed. However, the diffraction on the rain droplets, which can be identified by the interference fringes on figure 4.7, might balance the energy losses within the cloud by contributing to the self-focusing effect, due to the modifications of the refractive index gradient.

4.2.3 Conclusion

The formation and propagation of filaments under reduced atmospheric pressure conditions and natural rain has been investigated over a distance up to 325 m. We have shown that the filaments still develop and propagate at 0.7 atm in a similar manner as at sea-level. Simply, the filament number within the beam is slightly reduced by a factor of 30 %. Furthermore, natural rain up to an extinction coefficient of 6.6 km^{-1} does not considerably affect the filamentation process. These results are encouraging with regard to laser filament lightning control, as two of the main possible constraints have been proven to be uncritical.

5 High voltage experiments

After the previous chapter has discussed some aspects of the beam propagation with regard to the particular constraints of lightning experiments, this chapter will now be concerned with those experiments that explore directly the influence of these conditions on the triggering and guiding ability of the filament.

The idea of laser guided discharges is already about 30 years old. As it had become possible to ionize the air by focussed laser pulses, one was considering to utilize the air plasma for the drain of discharges. Phenomenologically, the laser-induced plasma can have two effects: guiding and triggering. The path of a free discharge is usually erratic, as shown on the left picture in figure 5.1. By contrast, the right picture shows a guided discharge, which has followed the beam path of the laser over the whole gap. It is also possible that the discharge is guided only over a fraction of the gap. Triggering means that the laser is able to lower the high-voltage level at which breakdown occurs, and it is usually characterized by the reduction of the voltage inducing 50 % breakdown probability (U_{50}).

At first sight, one might think that the ionized area acts simply as a conductor in air [LFVC$^+$99, ZDWE95]. However, the introduction in section 2.5 has shown that the propagation of discharges in air is a highly complex process, and it turned out that this simple model implies contradictions [LFCC$^+$00]. Therefore, a more sophisticated explanation, which is based on Gallimberti's model
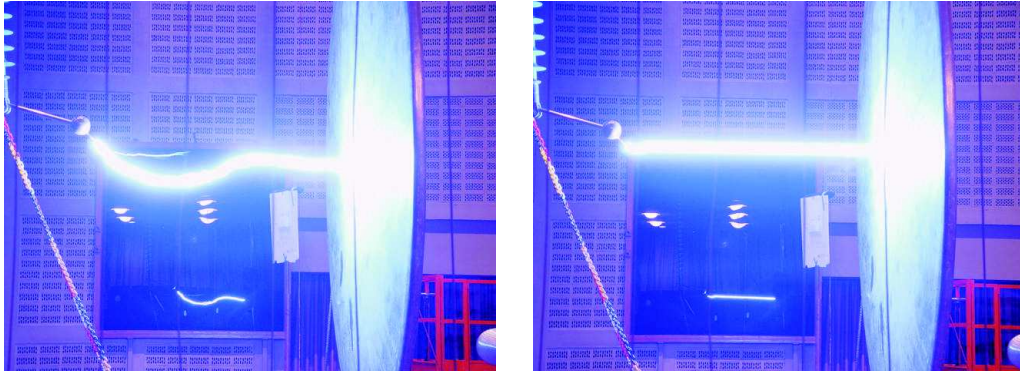
Figure 5.1: A free (left) and a laser-guided discharge in a 1.2 m shere-plane gap.

for the streamer-to-leader transition, is presented by Comtois *al.* [CPV$^+$03b].

Before the invention of ultrashort laser sources with pulse durations being short enough to produce an air plasma via Multi-Photon Ionization, high-energy CO_2-lasers had been used [MAS93, MSA96]. However, these types of lasers imply several disadvantages. In order to achieve an intensity high enough for ionization, the laser beam has to be strongly focused, geometrically limiting the extension of the ionized area. Moreover, both the high pulse energy and the strong focussing lead to high plasma densities on the order of $N_e \approx 10^{19}$ cm^{-3}, which means that the air is nearly entirely ionized. Calculating the critical plasma density (2.39) for the fundamental laser wavelength $\lambda = 10.6$ µm, it turns out that $N_{crit} \approx 10^{19}$ cm^{-3}. This means that the plasma is becoming opaque during ionization, and a considerable amount of the pulse energy is lost by absorption. Nevertheless, a laser guided lightning stroke is claimed to be observed, using a CO_2-laser with a pulse energy of 50 kJ, whose beam was focussed on the tip of a conventional lightning rod [USY$^+$99].

Due to the limitations of high-energy CO_2-lasers, the application of ultra-short laser pulses has become more popular in recent years [CM99, CPV$^+$03b, CPV$^+$03a, LFVC$^+$99, PCV$^+$01, RSW$^+$02], as they provide plasma generation via Multi-Photon-Ionization at moderate pulse energies. Besides, the opacity problem is avoided by typical laser wavelengths in the NIR or UV [MW96,

RSD01, ZDWE95], *e. g.* $N_{crit} \approx 10^{21}$ cm^{-3} at $\lambda = 800$ nm.

A first approach to trigger lightning is to replace or extend an existing lightning rod by the laser-induced plasma. As in this case the last step of lightning consists of the emergence of an upward moving positive leader [Uma01], most of the investigations have focussed on this type of leaders. It was shown [LFCC$^+$00] that a positive leader can be triggered and guided by an ultrashort laser pulse up to a length of 3 m, using a 400 mJ femtosecond pulse focussed by a lens with focal lengths between 4.7 and 8 m. It was observed that the laser reduces the U$_{50}$ to about 50 % of the value for free discharges. The setup could be improved further by using a bi-focal lens (f$_1$ = 4.4 m, f$_2$ = 6m), focussing the beam into a 2 m plasma channel in a 5 m gap [CPV$^+$03a, CPV$^+$03b].

However, as already discussed in the previous chapters, the Teramobile is able to produce long filaments at distances on the order of kilometers [RBM$^+$04], which offers the opportunity to intercept a descending lightning leader far above ground level. As 90 % of all lightning leaders have negative polarity [Uma01], the interaction of a filament with a negative leader is of special interest. A laser-triggered negative discharge was investigated by [LFVC$^+$99], using a lens with a focal length of 40 cm and 800 mJ pulse energy. This configuration is not capable to produce long filaments. A previous Teramobile campaign [RSW$^+$02] showed that it is possible to trigger and guide negative discharges in gaps up to 3.8 m. The laser reduced the U$_{50}$ by about 30 %.

The experiment described in the following section takes a step forward and explores the triggering and guiding of negative leaders in gaps up to 4.5 m. Special attention is turned to the constraints of the limited plasma lifetime of the filament and the peculiarities of negative discharges discussed in paragraph 2.5.4, *i. e.* the occurrence of space-leaders.

Yet, this experiment will confirm that the plasma lifetime is a crucial parameter for the prolongation of the guided lengths to an atmospheric scale. The main

reason is that the electron density in a *cold* plasma vanishes after about 1 μs. This difficulty is not restricted to laser-induced plasmas but concerns also the development of free discharges, as discussed in paragraph 2.5.2. There, it was pointed out that the main process for electron loss in air is the attachment to oxygen molecules. Several authors, therefore, proposed the use of a second, less intense laser-pulse to regain these electrons. This could either be a pulse from a separate laser [ZDWE95, YZL+02], aligned with the femtosecond beam, or a second, post-pulse from the femtosecond laser itself [HZL+05]. A separate laser source has the advantage of providing an independent choice of laser parameters, such as pulse duration, energy and wavelength, but the spatial overlap of both beams and the temporal synchronization of both pulses is delicate, especially when the geometry of filaments has to be considered. One or several post-pulses of the femtosecond laser are *a priori* aligned with their predecessors, however, the available laser energy must be shared among the two (or more) pulses, probably influencing the total triggering and guiding efficiency, too. Furthermore, the control and measurement of the pulse shape and energy of both pulses is not trivial, especially if the pulse splitting is performed before amplification [LWM+95]. We have tested both configurations and the results will be presented in section 5.2, discussing these issues in detail.

The last section of this chapter will discuss an experiment that is based on the encouraging results from the beam propagation experiments under rain conditions (section 4.2 and [CBK+03, MKY+05]). An artificial rain cloud has been produced between the two electrodes, and its influence on the triggering and guiding ability of the filament has been investigated. It will be shown that the rain does not stop the triggering and guiding ability of the laser filament.

5.1 Triggering and guiding of negative leaders

The results of a campaign at the high-voltage facility of the "Technische Universität Berlin" in 2001, where guided discharges in gaps up to 3.8 m could be observed, suggested subsequent experiments with longer gaps to demonstrate the full ability of the Teramobile to control discharges. As the high-voltage generator in Berlin was at 3.8 m already beyond its capability, it was decided to carry out this experiment at the "Centre d'Essais Aéronautiques de Toulouse" (CEAT) in Toulouse, France, where a more powerful generator is available with a specified maximum peak voltage of 5 MV and a stockable energy of 62.5 kJ.

The determination of the maximum possible guided length can on the one hand be achieved by increasing the gap distance up to the value, where the guided part cannot be extended further. Yet, the underlying physical parameter is the plasma lifetime of the filament, or more narrowly defined, the lifetime of *that* plasma state that allows triggering and guiding. The last formulation expresses the doubts of some authors that this might not necessarily be the free electron density but the O_2-ions instead [CPV$^+$03b]. Since the development of negative discharges is a highly complex process, the particular experimental conditions, such as the shape of the voltage pulse or the time when the laser pulse is sent, is likely to affect the guided length that can be achieved.

Another possibility of measuring the plasma lifetime is to send the laser pulse before the application of the high-voltage in order to determine the maximum time interval for which guided or triggered discharges occur. In the literature time delays between 3 µs [LFVC$^+$99] and several tens of microseconds have been reported [LFCC$^+$00]. However, those experimental conditions were different from ours, as lenses with short focal lengths along with slowly rising voltages pulse were used. Therefore, the determination of the plasma lifetime and the maximum guided lengths in a configuration allowing long filaments is still to be investigated. The measurement of both parameters is the main

objective of the following experiment.

The results of this experiment have been published in *Applied Physics B* [AMM$^+$06].

5.1.1 Experimental setup
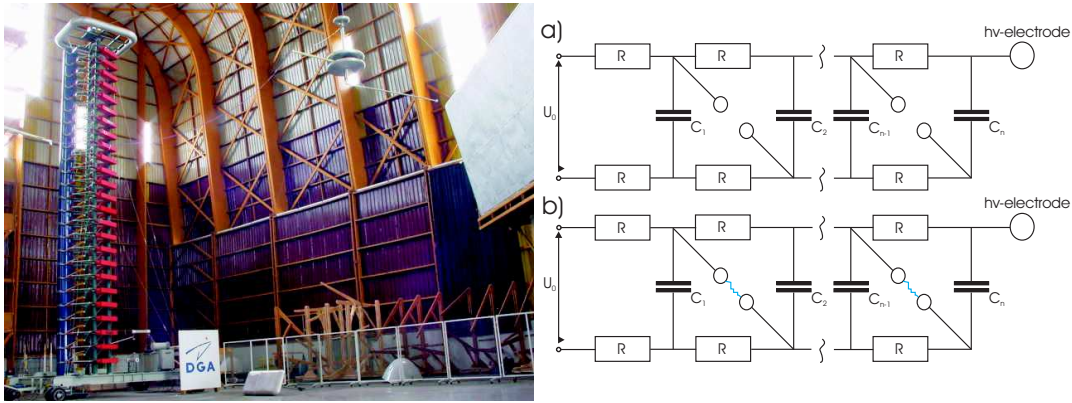
Figure 5.2: Picture of the high-voltage installation at the CEAT. The Marx generator with its 25 stages is on the left side and the both electodes on the right. In (a) a diagramm of a Marx generator is shown when being charged, and (b) shows the discharge situation when discharges within the different stages connect them in series.

We have installed the Teramobile in the high-voltage facility of the "Centre d'Essais Aéronautiques de Toulouse" (CEAT), France, that provides a high-voltage generator of the Marx-type with 25 stages. During the campaign the maximum peak voltage of the generator was 2.7 MV. The voltage pulses had a rising time of 2 µs and a decay time of about 50 µs.

The mode of operation of a Marx generator is depicted in figure 5.2. During the charging (a) all capacitors are connected in parallel and charged under a voltage U_0. When all stages are charged, the controllable small spark gaps connect the capacitors in series (b), providing a total voltage of nU_0, where n is the number of stages.

The applied voltage and the current at the high-voltage electrode have been

recorded as a function of time with a resolution of about 100 ns. Measuring the current in this way, provides information about the charge and current that is injected into the gap *before* breakdown and, hence, allows to draw conclusions on the discharge development. The high-voltage electrode was a sphere with a diameter of 8 cm, while the ground electrode was a plate with a height of 5 m and a width of 10 m. A small hole had been drilled into it in order to avoid ablation due to the high intensity of the filament.

The Teramobile was placed at a distance of about 23 m from the high-voltage electrode (see figure 5.3). The beam was sent outside by using the sending telescope, for which the focal length was chosen such that the filamentation started about 1 m upstream from the high-voltage electrode. The occurrence of filaments was checked by evaluating burns of the beam profile on impact paper, similarly to the procedure described in section 4.2. The pulse was negatively chirped, leading to an initial pulse duration of 500 fs, as this led to the maximum triggering efficiency.

The trigger of the laser was transmitted to the control room via an optical fiber
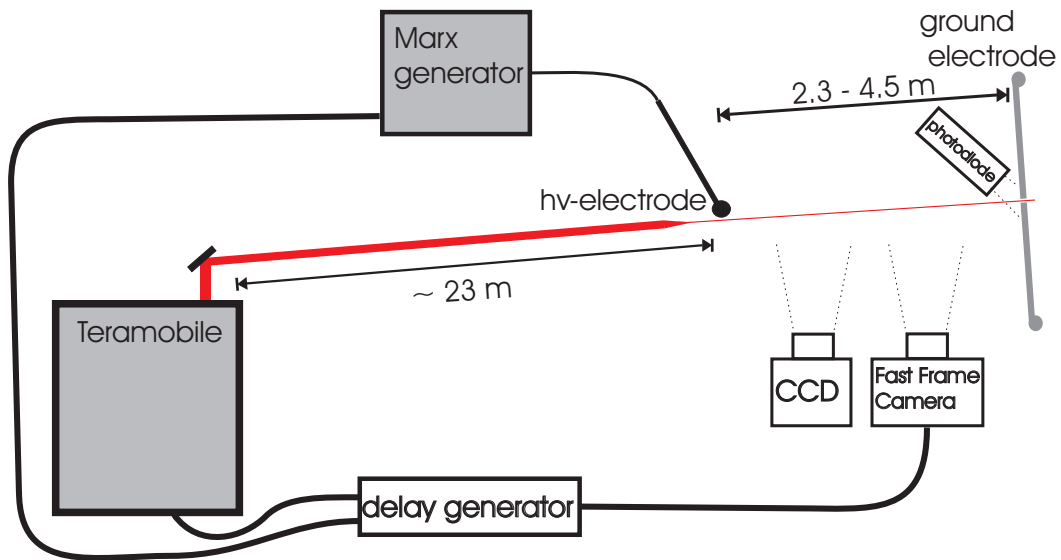
Figure 5.3: Sketch of the setup at the CEAT.

in order to synchronize it with the voltage pulse of the generator. The delay τ between the laser and the voltage pulse was adjusted between 1 µs *before* the voltage pulse and 2.6 µs *after* it. Here, the delay $\tau = 0$ corresponds to the laser pulse arriving simultaneously with the start of the voltage pulse, *i. e.* negative delays always mean that the laser arrives before the voltage begins to rise. The time at which the laser pulse arrived at the electrodes was recorded by a photodiode.

A fast-frame camera, synchronized with the voltage pulse, allowed to take pictures of the different steps of the discharge. Sets of 12 and 24 pictures with a total time window of 1.1 µs and 2.4 µs, respectively, were available. The acquisition time of each single picture was 50 ns with an interval of 40 ns between each. Additionally, still pictures of each discharge have been taken in order to evaluate its guided length.

5.1.2 Results and Discussion

Figure 5.4 shows a set of fast-frame camera pictures (a), the records of the high-voltage and current (b) and a still photograph of a partially guided discharge in a 4.5 m gap, which is far above the threshold of 2 m for space-leader formation [Gro81, BGB$^+$94]. The peak voltage was 2.2 MV, and the laser arrives 1.2 µs after the start of the voltage pulse. The total guided length was 1.9 m. Up to 2.7 MV, which was the limit of the generator performance, all discharges were at least partially guided. Therefore, it is reasonable to conclude that they were all laser triggered by the laser.

On the first fast-frame camera picture one can see that a space-leader has been developing about 1 m away from the high-voltage electrode. During the next 300 ns it is propagating towards the cathode and connects to the emerged electrode leader 2 µs after the application of the high-voltage. The fusion of both leaders causes a characteristic current peak [BGB$^+$94], reaching nearly
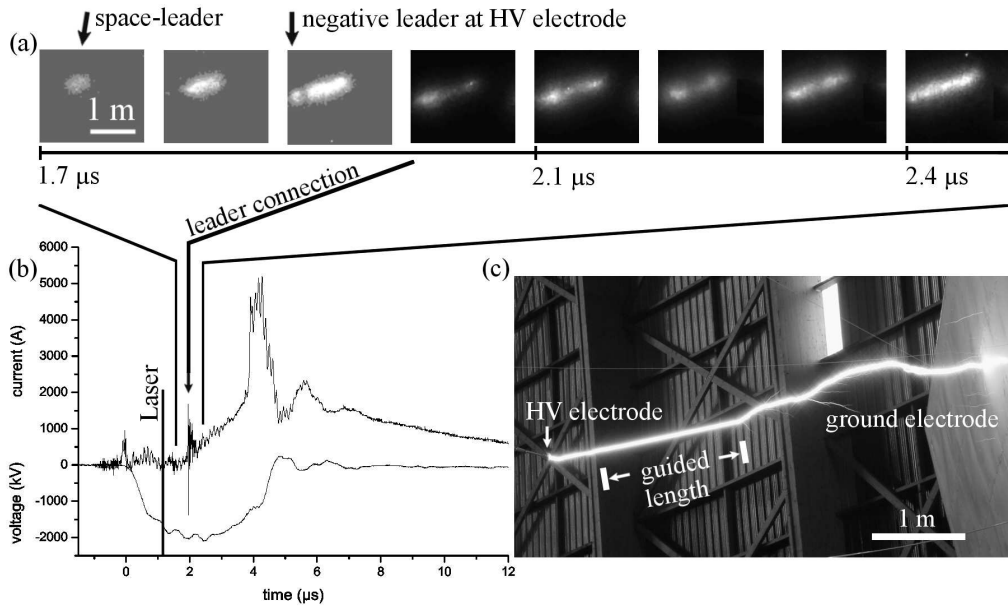
Figure 5.4: (a) a sequence of fast-frame camera pictures zoomed into the first part of the gap to show the space-leader formation, (b) the corresponding records of the high-voltage and current and (c) a still photograph of a partially guided discharge in a 4.5 m gap. The exposure time of each fast-frame picture was 40 ns with a delay of 50 ns each.

1 kA in this case. Moreover, an increasing current is flowing into the gap after the connection of both leaders, in consequence of which even the high-voltage falls to nearly half of its peak value *before* breakdown. We measured a charge consumption that reached up to 400 µC m^{-1} for guided discharges. An increased leader current is also observed for free space-leader discharges [Gro81].

The charge consumption for *free* discharges was determined in a 3.4 m gap because of a lack of generator performance. We have measured a value of (160 ± 30) µC m^{-1} for free discharges without space-leader formation, in line with the value of 158 µC m^{-1} reported elsewhere [ROG+95].

The evaluation of all available fast-frame picture sets, on which a space-leader can be identified, allows the determination of the mean value of the space-leader velocity. The propagation velocity of the cathode-directed, positive leader is
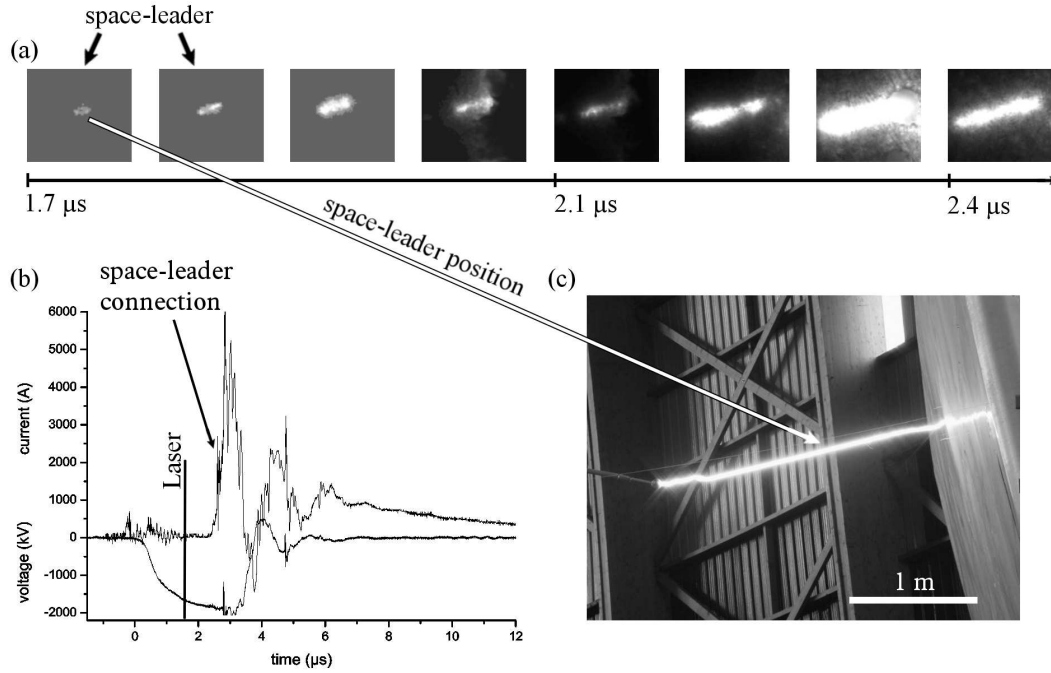
Figure 5.5: (a) a sequence of fast-frame camera pictures for a triggered space-leader in a 2.3 m gap, (b) oscillograms for a space-leader discharge under similar conditions for a laser delay of 1.7 μs and (c) a still photograph of the discharge.

calculated from 11 picture series and amounts to $(2.4 \pm 0.5) \times 10^6$m/s. This is on the same order of magnitude as previous measurements on guided leaders [CPV+03a, RSW+02].

Figure 5.5 shows a guided discharge in a 2.3 m gap. This distance is near to the threshold for space-leader formation. The peak voltage was 2.0 MV $\approx 1.2 \times U_{50}$ and the laser was shot 1.2 μs after the start of the high-voltage pulse. The mechanism of space-leader formation is similar to the one described above for the 4.5 m gap, however, the current peak in figure 5.5 is more difficult to identify due to the shorter time scale. One has to notice that the current and voltage oscillograms originate from a different shot than the pictures in (a) and (c), as there were no oscillosgrams available for the measurements on that day. In figure 5.5, it is clearly visible that the position of the space-leader formation does not coincide with the end of the guided part of the discharge, unlike obser-
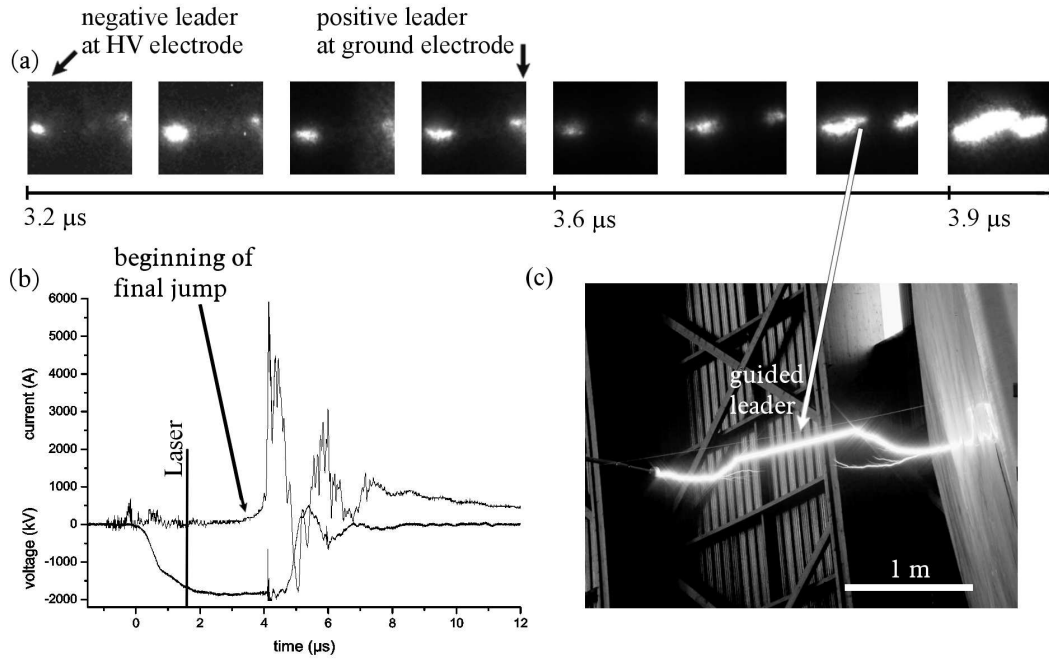
Figure 5.6: (a) a sequence of fast-frame camera pictures for a guided electrode leader in a 2.3 m gap, (b) oscillograms of a discharge with a guided electrode leader under similar conditions for a laser delay of 1.7 μs and (c) a still phtograph of the discharge.

vations reported in [LFVC$^+$99] in the case of a more focussed beam, resulting in a well localized plasma region. In that case a space-leader-like structure was developing at the borders of a 30 cm long laser plasma channel, whose dimensions where well defined, as a lens with a focal length of only 40 cm had been used. The authors explain the leader formation by the perturbation of the electric field induced by the plasma channel. In our case with long filaments, however, there is no defined channel end, so that the mechanism must be different.

Figure 5.6 shows a guided discharge in a 2.3 m gap under the same conditions as above in the case when no space-leader occurs. Here, the streamers have bridged the entire gap, leading to the initiation of the final jump (see section 2.5). As the dynamic range of the fast-frame camera is not sufficient to display
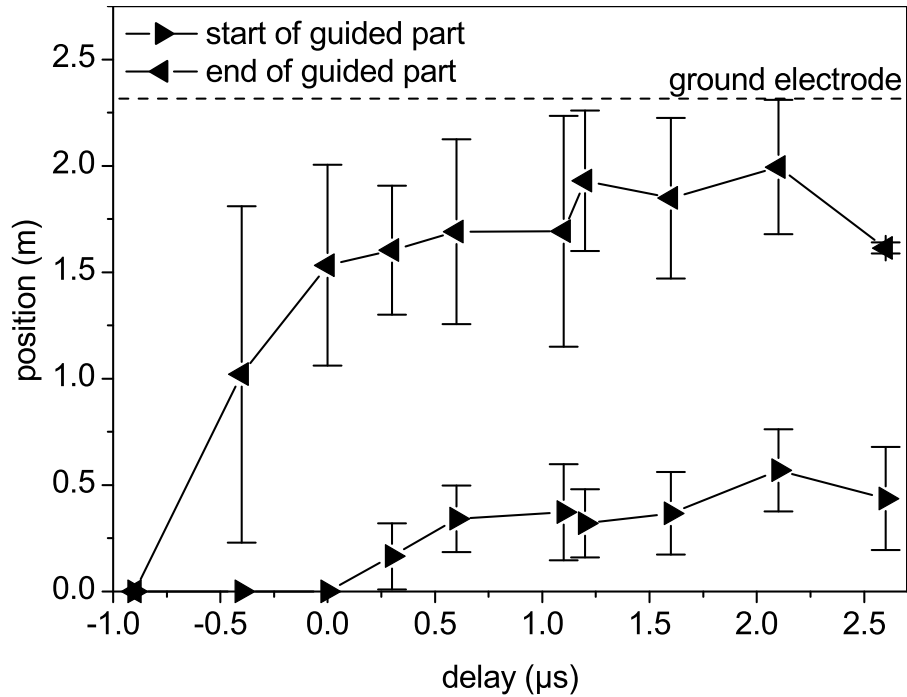
Figure 5.7: Parameters of the guided parts of the discharge in a 2.3 m gap at voltage levels of about 2.0 MV. The error bars indicate the standard deviation.

both the streamers and the more luminous leaders, the arrival of the streamers has to be identified by the positive leader starting from the ground electrode. The electrode leader and the positive leader, then, approach with an increasing speed, which is accompanied by a characteristic current rise (see section 2.5), and their connection immediately leads to the breakdown of the gap. At 3.8 μs after the the start of the voltage-pulse, the fast-frame pictures show that the electrode leader connects to the plasma channel, leading to guiding over a small fraction of the gap. This type of discharge is called a *guided electrode leader* in the following discussion.

In order to draw conclusions on the plasma lifetime, the laser was shot before the application of the high-voltage, and figure 5.7 displays the position of the guided parts of the discharge as a function of the laser delay. One can see that the guided lengths drop rapidly to zero for negative delays, and no triggered or guided event could be observed if the laser was shot more than 1 μs before
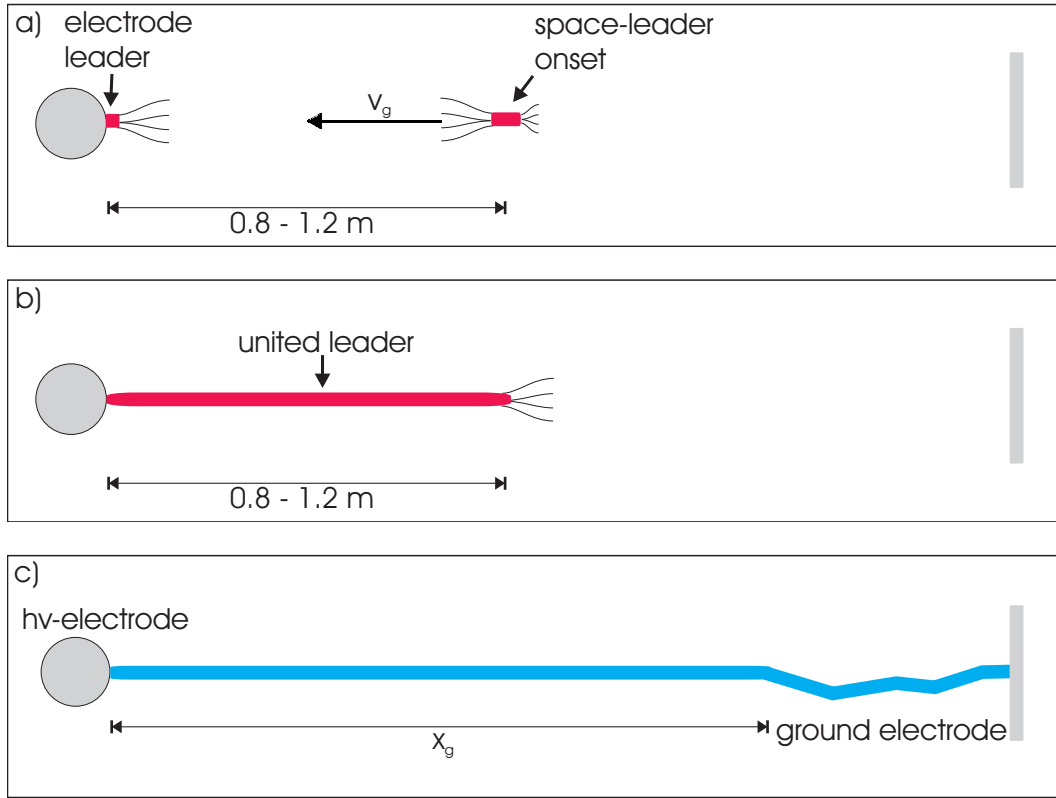
Figure 5.8: Sketch of the calculation of the plasma lifetime. After the space-leader has developed within the gap, it propagates with the velocity v_g towards the cathode (a). After the connection to the electrode leader, the united leader (b) continues its propagation within the filament, until the guiding stops, when the plasma lifetime is exceeded. The total guiding length x_g (c) can be derived from the still pictures.

the application of the voltage. This gives an estimation of the plasma lifetime, which has lost its capability after 1 µs to trigger discharges in the absence of an electric field. For increasing positive delays, the beginning of the guided part moves into the gap, as the space-leader connects to the emerged electrode leader, visible *e. g.* on the third fast-frame picture of figure 5.4(a).

The plasma lifetime is also confirmed by the analysis of the fast-frame camera pictures. According to figure 5.4(a), the propagation of the space-leader towards the cathode begins $t_d = 800$ ns after the arrival of the laser pulse. The high current flowing into the gap after the connection of the electrode leader to the space-leader (see figure 5.4(b)) is an indication that the discharge devel-

opment is accelerating, suggesting that a delay between the connection of the space-leader to the electrode leader and the further propagation of the now united leader, may be neglected. Therefore, the following equation holds for the plasma lifetime t_p

$$x_g = v_g(t_p - t_d), \tag{5.1}$$

where x_g is the guided length and $v_g = 2.4 \times 10^6$ m/s the leader velocity within the plasma channel that was determined above. The lifetime has been determined to be $t_p = (1.3 \pm 0.4)$ µs by evaluating seven events. The principle of the calculation is also sketched in figure 5.8.

In the following discussion, it will be pointed out that both the observation of a triggered space-leader as well as the observed guided lengths may be explained by a facilitated streamer-to-leader transition, provided by the electrons of the propagating streamers *and* of the filament.

Figure 5.9 shows the position of the end of the guided part of *guided electrode leaders* (figure 5.6) for 15 different shots, showing that the end position of the guiding is limited to about 1.5 m. The laser delay was $t = 1.2$ µs for all shots.
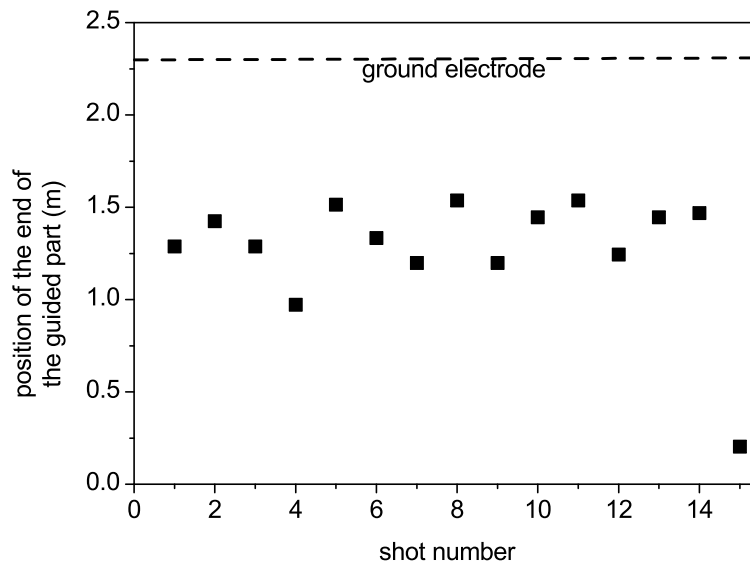

Figure 5.9: The guided lengths of all events for which a guided electrode leader could be proven by the fast frame pictures.

Since an interaction of the streamers and the filament shall be proven, one has to be able to make a statement on the streamer propagation. As mentioned above, the streamers and the space-stem are not visible on the fast frame pictures, but at least at lower limit for the streamer velocity v_s can be estimated, as being the time between the application of the voltage and the breakdown of the gap. This velocity is found to be not less than $v_s = 0.7 \times 10^6$ m/s. This means, when the laser arrives 1.2 µs after the application of the high-voltage, the streamers have propagated at least 80 cm into the gap. This coincides well with our observation that the space-leader occurred in an interval between 0.8 and 1.2 m downstream from the high-voltage electrode. Referring to Gallimberti's model for the streamer-to-leader transition, the transition is driven by the free electrons providing the necessary current for the heating process. Since the electron concentration is high only in the streamer head (section 2.5), the space-leader may be initiated where the sum of the electrons in the streamer head and of those of the laser-induced plasma channel provide the necessary current to initiate the development of a space-leader, *i. e.* starting at 80 cm downstream from the high-voltage electrode for a laser delay of $t = 1.2$ µs.

Starting from this time, the duration, in which an interaction between the streamer head and the filament may take place, is given by the plasma life-
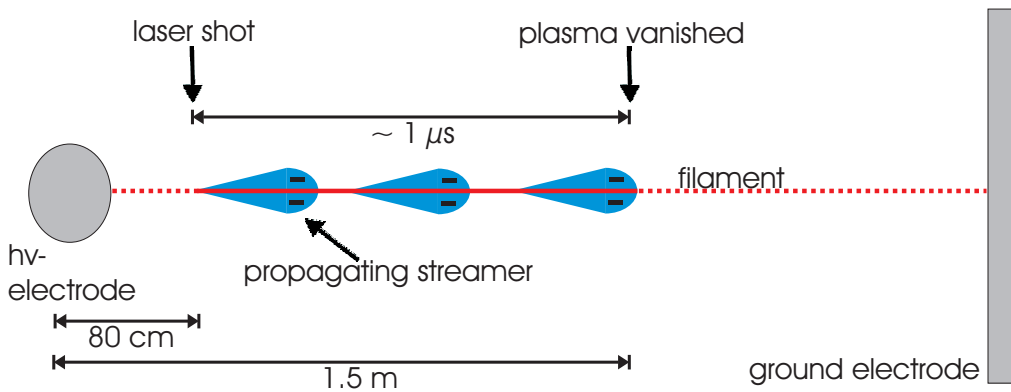

Figure 5.10: Illustration of the observed positions of space-leader occurrence and guided lengths due to an interaction of the streamers with the laser filament.
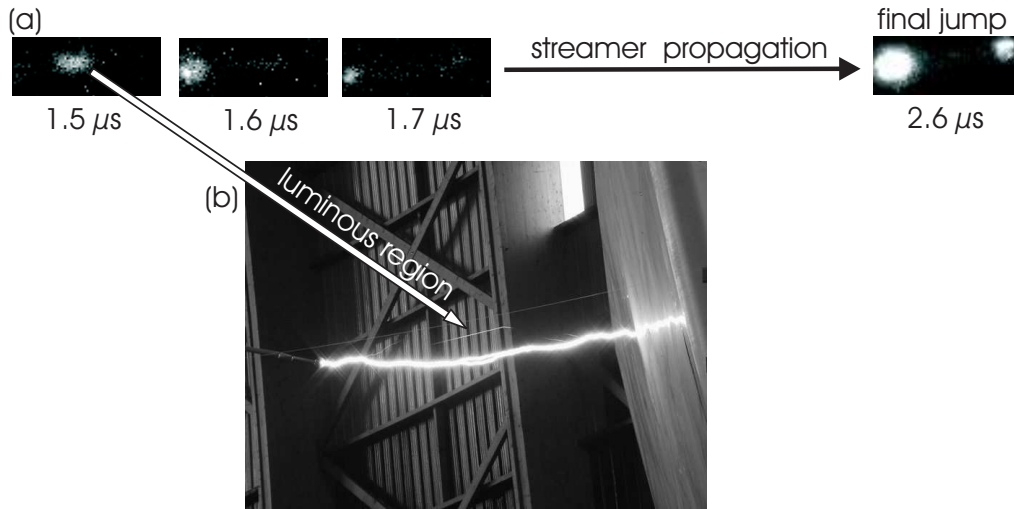
Figure 5.11: (a) fast-frame camera pictures and (b) a still photograph of an un-guided discharge. The luminous region on the first fast-frame picture that can also be seen on the still photograph indicates heating within the plasma channel.

time $t_p = 1$ µs, and during 1 µs the streamer propagates at least additional $v_s t_p \approx 0.7$ m. This yields the observed, maximum distance of the guided part from the high-voltage of 1.5 m in figure 5.9. The proposed mechanism may also be clarified by figure 5.10.

We were able to observe the proposed mechanism directly on at least one series of fast-frame pictures (figure 5.11), where the leader has not followed the guided streamer, preventing this region of the picture from saturating. The conditions were the same as for the two discharges above in the 2.3 m gap. On both the first fast-frame picture and the still picture a luminous region is visible in the middle of the gap. In contrast to the case shown in figure 5.5, the heated, luminous region does not develop into a space-leader, and after the initiation of the final jump, the eletrode leader chose a different path.

The observed plasma lifetime of about 1 µs is significantly shorter than that reported in the literature in the case of stronger focusing, where plasma lifetimes between 3 and several 10 µs were observed. Comtois *al.* [CPV+03b] propose that it is not the free electron density, but rather the increased density of

O_2^--ions that facilitates the streamer-to-leader transistion within the plasma channel. According to our observations, this is not the case for long filaments, as the experiments have revealed that it is the characteristic plasma lifetime of about 1 µs that allows triggering and guiding.

Apart from the plasma lifetime, the achievable guided lengths are of special interest with regard to atmospheric applications. Therefore, figure 5.12 shows the guided lengths as a function of the gap distance for laser delays between 0 and 2.6 µs. This chart only incorporates those shots for which the occurrence of a space-leader could be proven by the fast-frame pictures. The guided length reaches 1.4 m for the 2.3 gap and drops to about 1.2 m at 4.5 m gap distance. This difference can be explained by a delay that is oberved between the arrival of the laser pulse and the first occurrence of a space-leader. It was measured to be (800 ± 300) ns for the 4.5 m gap. Owing to the limited time window of the fast-frame camera, the corresponding value could not exactly be measured for the 2.3 m gap, but it could be estimated to be below 450 ns. As in the short gap the voltage level was significantly higher than at 4.5 m, *i. e.* compared to the corresponding U_{50}, this delay may indicate the necessary time to heat up the region, where the streamer-to-leader transition takes place. It is also consistent with the slightly lower value for the plasma lifetime if it is measured by sending the laser pulse before the voltage pulse (1.0 vs. 1.3 µs), as a similar heating mechanism probably takes place.

Figure 5.12 also shows results of the previous Teramobile campaign [RSW+02]. At that time, laser delays between 2.4 µs and 5 µs had been applied in gaps between 1.2 and 3.8 m. The rising time of the voltage pulses was 1.2 µs, slightly shorter than that of the present experiment leading to a further increase of the time between the high-voltage peak and the laser. The experiments were conducted at moderate voltage levels so that all observed discharges were at least partially guided and can be, therefore, assumed to be triggered by the laser. According to figure 5.12, the guided lengths increase linearly up to a gap dis-

tance of 2.4 m, where a saturation seems to occur. This distance corresponds well to the measured plasma lifetime of about 1 µs and the leader velocity of 2.4×10^6 m/s measured above if one assumes that the emerged electrode leader directly connects to the plasma channel. The above condition of moderate voltage levels is important for optimum guided lengths, as a propagating leader, generated by a stronger electric field, would connect to the filament somewhere between the electrodes.
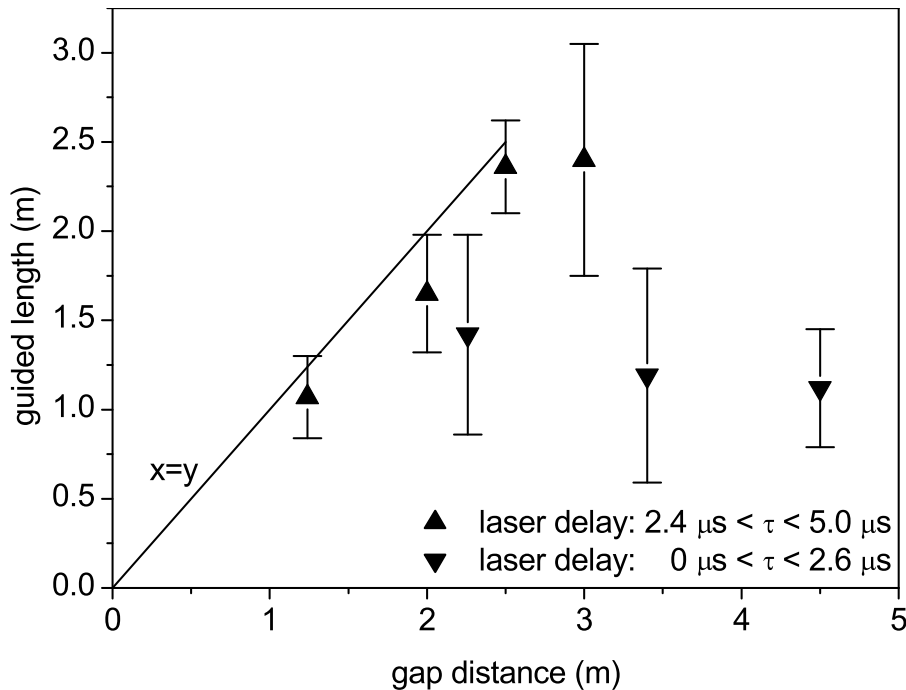
Figure 5.12: The mean values of the total guided lengths as a function of the gap distance. τ denotes the time delay between the laser and the beginning of the voltage pulse. The error bars indicate the standard deviation. The results for laser delays between 2.4 µs and 5.0 µs were obtained in a previous experiment [RSW[+]02].

5.1.3 Conclusion

We have triggered and guided negative discharges in gaps up to 4.5 m. The laser is able to trigger a space-leader discharge if it is shot before the initiation of the final jump. The lifetime is about 1 µs, corresponding to the character-

istic lifetime of a cold plasma in air. Therefore, the free electron density is responsible for the triggering and guiding process rather than the O_2^--ions as suggested before in the case of a focused laser geometry [CPV$^+$03b]. Along with the leader velocity within the plasma channel, which was determined to be about 2.4×10^6 m/s, guided leaders up to a length of 2.4 m can be expected. Aiming to real lightning control, these results show that new techniques will be required to enhance the plasma lifetime. This will be the subject of the experiment described in the following section.

5.2 Improved trigging with dual fs-ns pulses

The last section has revealed that the plasma lifetime of long filaments created by the Teramobile is about 1 µs, limiting the guided lengths of discharges to a few meters. This is a severe restriction, as on a short scale their properties are outperformed by a strong focussing of high-energy lasers, as they provide, in addition, a longer plasma lifetime leading to higher triggering probabilities.

Like for free discharges (see section 2.5) the main process for electron losses in air is the attachment of free electrons to the oxygen molecules, resulting in O_2^--ions. The use of a second laser pulse in order to enhance the plasma lifetime can mainly be based on two effects:

- plasma heating by inverse bremstrahlung

- electron detachment from the oxygen molecules.

In the following the implementation of a dual fs-ns-pusle experiment is described and the contributing effects are being evaluated. The experiment has led to a publication in *Applied Physics Letters* [MAK$^+$06].

5.2.1 Experimental setup

The experimental setup is very similar to that described in section 5.1 and sketched in figure 5.13. The Teramobile was installed at the high-voltage facility of the "Technische Universität Berlin". This installation is equipped with a 14 stage Marx-generator, whose mode of operation has been already depicted in paragraph 5.1.1. It provides a maximum peak voltage of up to 2 MV and voltage pulses with 1.2 µs rising and 50 µs decay time. The high-voltage electrode was a sphere with a diameter of 12 cm, while the ground electrode was a plane with a diameter of 3 m. A small needle was attached to the high-voltage sphere in order to have a defined position of the leader onset due to the high electric field at the tip. Gap distances up to 1.2 m have been investigated. The sending telescope focussed the beam such that the filamentation started about 1 m upstream from the high-voltage electrode. The pulse was negatively chirped leading to an initial pulse duration of 170 fs.

A Nd:YAG-laser, type Spectraphysics "Quanta-Ray", was installed behind the Teramobile container and its beam was combined with the femtosecond beam
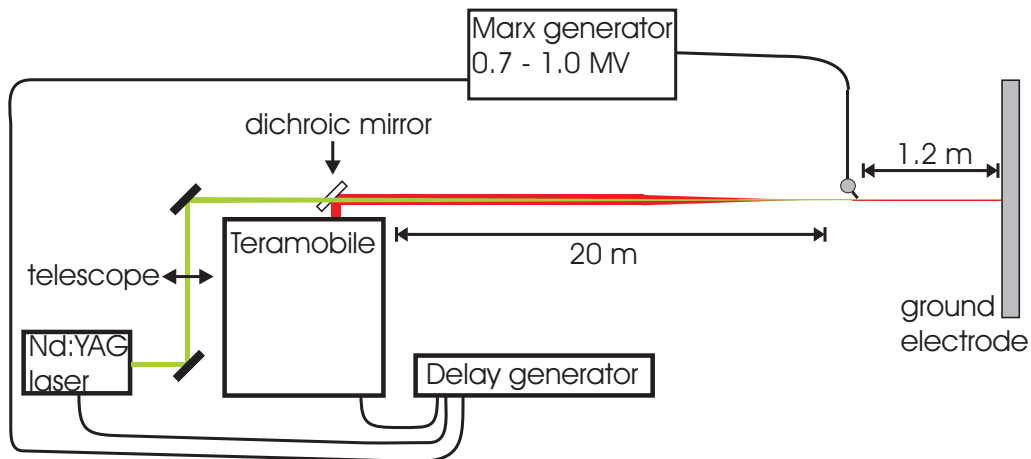

Figure 5.13: Sketch of the setup for the ns-fs experiment. Both the beam of the Teramobile beam and the Nd:YAG-beam have been focussed onto the high-voltage eletrode (f ≈ 20 m). The time delay between both pulses has been adjusted with a delay generator.

by a plane dichroic mirror on the container roof by using a periscope construction. The laser delivered pulses with a duration of 7 ns at 10 Hz, synchronized with the laser pulses of the Teramobile. The Nd:YAG was focused by a telescope so that the beam entirely covered the filamentation bundle (≈ 1 cm) at the high-voltage electrode. The overlap was monitored by using a small alignment laser that was installed upstream from the sending mirror of the Teramobile, by observing its reflex on a wall in the control room.

Both lasers have an inherent jitter on the order of several nanoseconds (see section 3.1). Therefore, only the shots for which the femtosecond and nanosecond pulses were temporally overlaped have been incorporated into the statistics. Doing so, about 30 % of all shots were discarded during the data analysis. The delay of both lasers was set about 6 µs after the start of the voltage pulse.

Alternatively from the fundamental wavelength of $\lambda = 1064$ nm with a pulse energy of 800 mJ, the laser provided also the second harmonic at $\lambda = 532$ nm with 400 mJ. The delay between the laser pulse of the Teramobile and the Nd:YAG-laser has been adjusted such that both pulses were sent at the same time. The time of arrival of the pulses was recorded by two photodiodes.

Both the Nd:YAG-laser and Teramobile laser have been equipped with ferites cores on critical elements, especially the Pockels cells, in order to reduce the electromagnetic perturbation by the high-voltage generator.

5.2.2 Results and Discussion

Figure 5.14 shows the triggering probability for both the femtosecond beam alone and for the fs-ns dual pulse as a function of the applied high-voltage. The nanosecond pulse significantly increases the triggering probability of the discharge at low voltage levels, and in the following the possible mechanism leading to this effect will be discussed.

As addressed in the introduction, the nanosecond laser pulse may heat the

plasma by inverse bremsstrahlung. Yet, it turns out quickly that the plasma density of the filament, being on the order of $N_e \approx 10^{16}$ cm^{-3} [SS99, TFA$^+$99], is too low for efficient plasma heating. The absorption coefficient for inverse bremsstrahlung is

$$\alpha = \frac{\nu_{ei}\omega_{p2}}{c\omega^2}, \qquad (5.2)$$

where ω is the laser frequency, ω_p the plasma frequency and

$$\nu_{ei} = \frac{3 \times 10^{-6} N_e \ln(\Lambda)}{T_e^{1.5}}. \qquad (5.3)$$

A typical range for the Coulomb integral is $1 < \ln(\Lambda) < 10$ [CPV$^+$03a]. Treating the plasma generated by the femtosecond laser pulse as an ideal gas with $N_e \approx 10^{16}$ cm^{-3} and assuming that all deposited energy is dissipated in plasma heating, an upper limit is a temperature rise of only 4 °K, for a heating pulse of the second harmonic of a Nd:YAG-laser at $\lambda = 532$ nm and 1 J pulse energy.
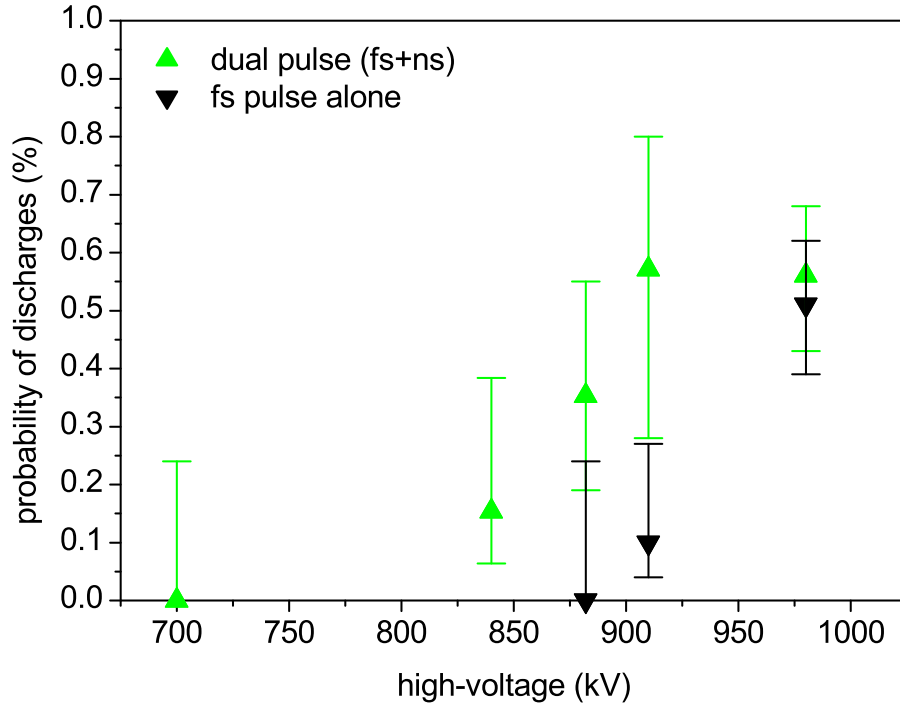

Figure 5.14: Triggering probability of high-voltage discharges with both a single femtosecond pulse alone and the dual, femtosecond-nanosecond pulse. The wavelength of the nanosecond pulse was 532 nm. The error bars indicate the confidence intervals at a level of 95 %.

Therefore, electron detachment from the oxygen molecules is the dominant process for the development of the leader in a free discharge. In order to calculate the effect to be expected from the nanosecond pulse, a detachment coefficient γ_l has to be added to the rate equations (2.59) and (2.60) [YZL$^+$02, ZDWE95]

$$\frac{\partial N_e}{\partial t} = \alpha N_e - \eta N_e - \beta_{ep} N_e N_p + \gamma_l N_n \qquad (5.4)$$

$$\frac{\partial N_p}{\partial t} = \alpha N_e - \beta_{ep} N_e N_p - \beta_{np} N_n N_p \qquad (5.5)$$

$$\frac{\partial N_n}{\partial t} = \eta N_e - \beta_{np} N_n N_p - \gamma_l N_n, \qquad (5.6)$$

where the detachment coefficient is defined as

$$\gamma_l = \frac{\sigma_{O_2^-} I_{Laser}}{\hbar \omega}. \qquad (5.7)$$

I_{Laser} denotes the intensity of the nanosecond laser pulse, ω its frequency, $\sigma_{O_2^-} = 1.5 \times 10^{-19}$ cm^2 at $\lambda = 532$ nm and $\sigma_{O_2^-} = 4.6 \times 10^{-21}$ cm^2 at the fundamental wavelength $\lambda = 1064$ nm, respectively. From equation (5.7) one concludes that a higher effect is observed for shorter wavelengths. Figure 5.7 displays the plasma density, calculated from the equations (5.4) - (5.6), for a femtosecond pulse alone, generating an initial electron density of $N_e = 10^{16}$ cm^{-3}, and of a nanosecond pulse, arriving simultaneously with the femotsecond pulse (Δ t = 0) and after a delay of 500 ns. The laser condition corresponds to the Nd:YAG-laser used in this experiment. One concludes that the electron detachment induced by the ns-laser, arriving simultaneously with the femtosecond pulse (Δ t = 0), may not be responsible for the observed improvement of the triggering probability. This is mainly due to the fact that the amount of the attached electrons is still too small for a sufficient laser detachment when both pulses arrive simultaneously. According to figure 5.15, a delay on the order of several hundred nanoseconds is, therefore, efficient. However, if the nanosecond laser hits an already formed electrode leader, it can effectively photodetach electrons from O$_2$-ions, since (see section 2.5)

- the plasma is already heated to a temperature between 300 - 1500 °K
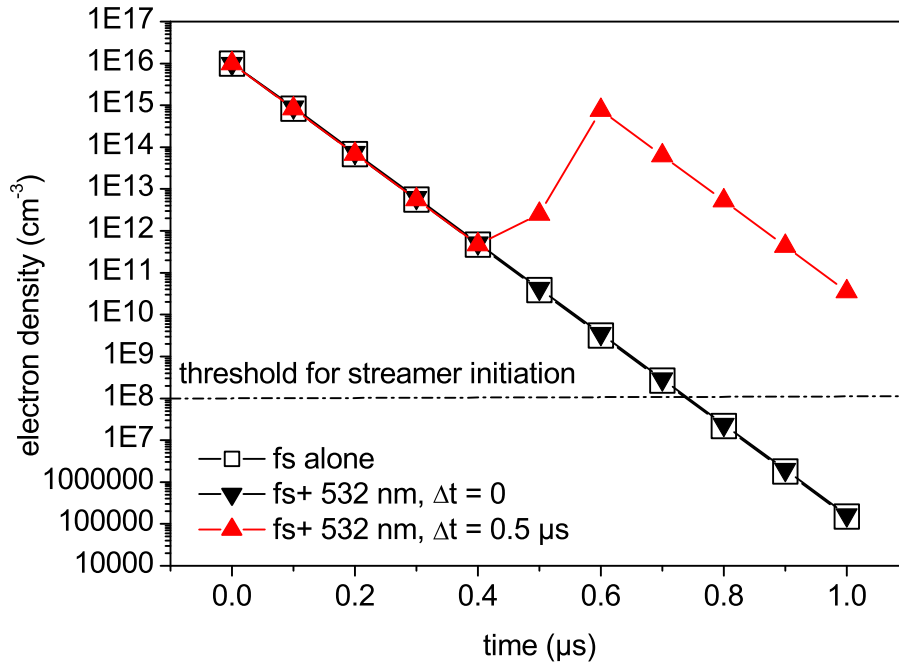
Figure 5.15: Calculated electron density for three different configurations.

- a considerable amount of O_2^--ions has been produced by previous streamers.

Experiments under similar conditions have shown that the electrode leader only propagates a few centimeters into the gap if *no* breakdown occurs [Gro81]. This means that, under the present conditions, the leader head is still in the vicinity of the high-voltage electrode when the laser pulses arrive several µs after the maximum of the voltage pulse, and electron detachment in the leader head is possible.

Yet, it is essential that the lasers are aligned such that the region is covered where the leader develops. Indeed, we have only observed an effect of the nanosecond pulse when the laser beams were aligned on the needle tip at the high voltage electrode. Due to the high electric field, the leader leaks from the needle tip (see left picture in figure 5.16), and the lasers have to be aligned on this area in order to observe an effect. Increasing the peak voltage results in longer propagation of the electrode leader and, therefore, reduces the proba-
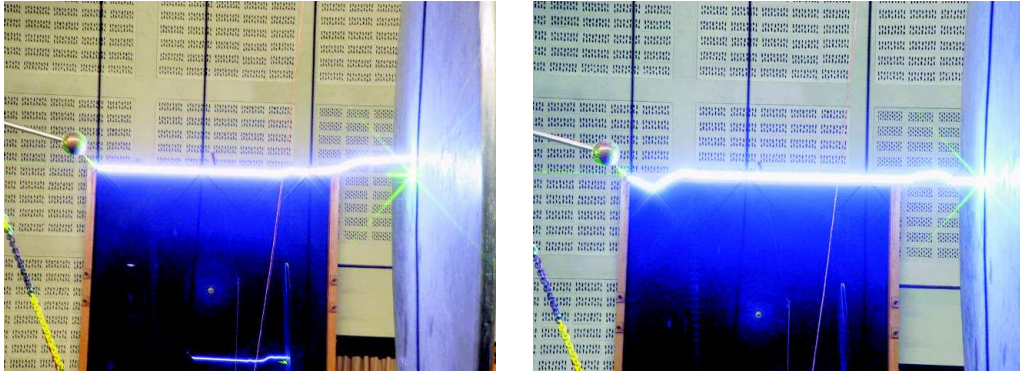
Figure 5.16: The left picture shows a triggered discharge at a voltage level of 910 kV. The laser beams were aligned onto the needle tip. The right picture shows a triggered discharge at a higher level of 980 kV, and the laser beams were aligned slightly higher.

bility that it comes across the filament. This may explain the significant effect of the nanosecond pulse only at low voltage levels.

When the lasers are not aligned on the needle tip (right picture in figure 5.16), there is no possibility of electron detachment in the leader head, and the nanosecond pulse has no effect. The corresponding triggering probability for a femtosecond pulse alone as a function of the high-voltage is shown figure 5.17. The chart exhibits a maximum at 1050 kV and then decreases again for higher voltages, in line with the argumentation above that the propagating electrode leader moves away from the beam path.

No effect has been observed when the fundamental wavelength at $\lambda = 1064$ nm was used, as one would expect from equation (5.7). Also, no effect has been observed, when the lasers were shot before the application of the high-voltage.
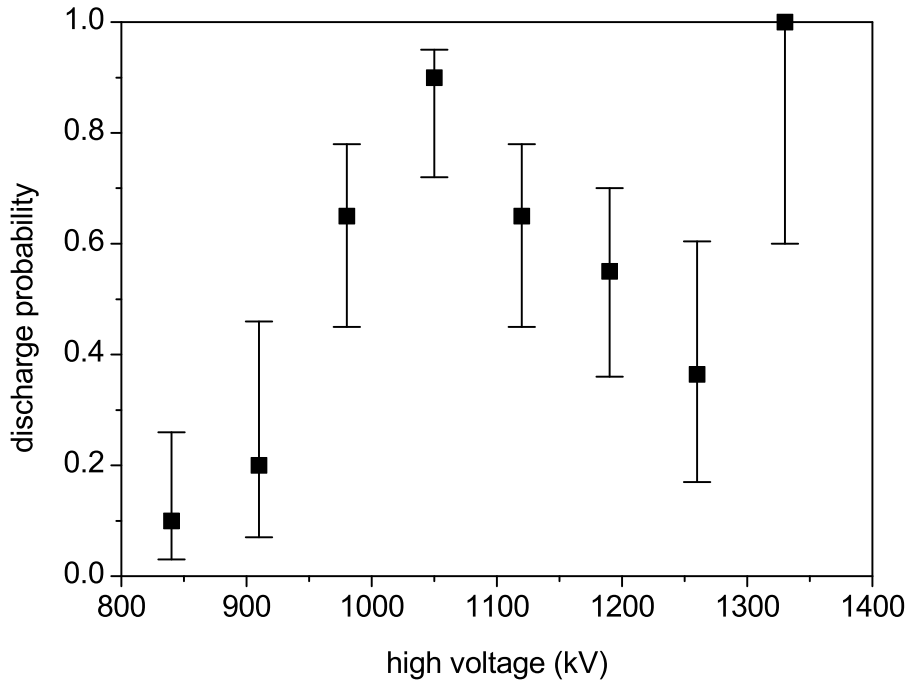
Figure 5.17: Triggering probability as a function of the high-voltage for a fs-pulse alone for the case that the laser beam is not aligned on the needle tip.

5.2.3 Conclusion

It has been shown that the triggering ability of laser filaments can be improved by a secondary nanosecond pulse, which is sent at the same time as the femtosecond pulse. The higher triggering probability can be explained by an accelerated streamer-to-leader transition within the head of the electrode leader, initiated by the photodetachment of the nanosecond laser. Therefore, it has been proven that an improved laser triggering and guiding by electron detachment is in principle possible.

Further experiments may confirm the effect at longer gap distances or by the observation of an enhancement of the plasma lifetime, by shooting the lasers *before* the application of the high-voltage pulse as described in section 5.1.

5.3 Triggering of high-voltage discharges with dual fs-ps pulses

As already mentioned in the introduction to this chapter, we also conducted a double-pulse experiment, where the original femtosecond pulse was splitted. However, those experiments were not successful, which was mainly due to technical problems with the setup. It is the aim of this section to address, at least, the problems that have been encountered.

The setup of the pulse splitting is shown in figure 5.18. The original pulse was divided by a 50:50 beam-splitter. The first pulse maintainted a duration of about 100 fs, whereas the other pulse was strechted to about 24 ps by propagating it through a highly dispersive glass block. It was installed downstream from the strechter but still before the first amplification stage. The material of the glass was "Ohara S-TIH53" that induces a chirp of $\psi'' = 218$ fs^2/mm at $\lambda = 800$ nm. The block had a length of $l = 20$ cm. The delay between both pulses could be adjusted between 0 and 1 ns. We also performed experiments with fs-fs-pulse pairs by removing the glass block.
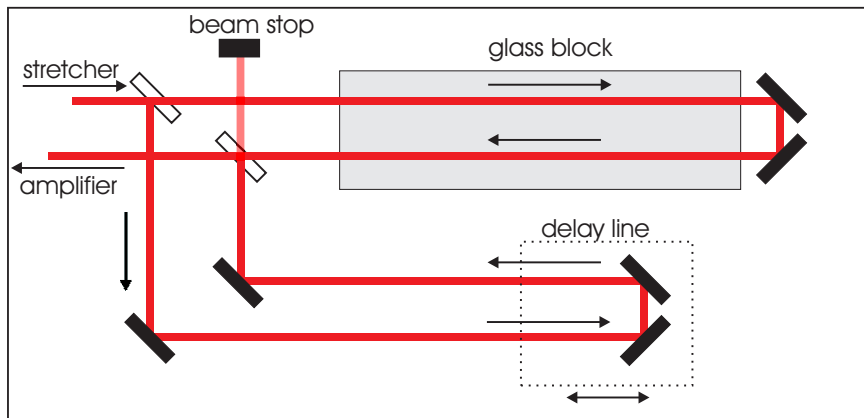
Figure 5.18: The pulse splitting setup.

With the double pulse setup installed, the Teramobile laser delivered double-pulses with a total energy of about 180 mJ after compression, which is considerably lower than the single-pulse specifications. This is mainly due to a degraded seeding of the regenerative amplifier, since the beam-splitter on the setup leads to a loss of 50 % of the original pulse energy. As the measured energy of 180 mJ is the sum of the energy of both pulses, the first femtosecond pulse, which generates the filament, has only about half of this energy, *i. e.* 90 mJ.

This reduced energy results in a strongly decreased triggering efficiency, as displayed in figure 5.19. This result is in contradiction with previous results [RSW+02], suggesting that the discharge probability remains constant when the threshold for filamentation is exceeded. The chart reveals an almost linear energy dependence of the triggering efficiency on the laser pulse energy. The decrease of the pulse energy by a factor of four in the double pulse configura-
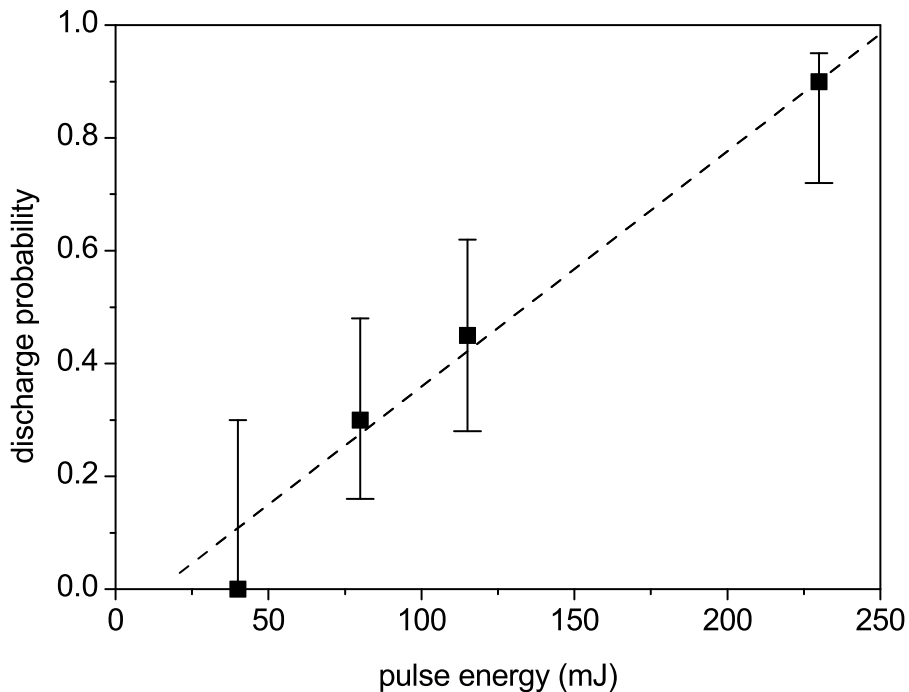
Figure 5.19: Triggering probability as a function of the pulse energy for a single fs-pulse. The linear fit yields a slope of 0.004 mJ^{-1}.

tion, therefore, drastically reduced the triggering efficiency, and the expected effect of electron detachment caused by the second pulse was not able to compensate for this energy loss. As for the pulse shaping experiments described in chapter 6, the pulse splitting *before* amplification leads to nonlinear effects within in the amplifiers, resulting in frequency shifts and additional sub-pulses [LWM$^+$95]. As there was no possibility of controlling the pulse energy of the first, femtosecond pulse as well as measuring its energy, not even a comparison with the results of single pulse experiments at the corresponding pulse energy was possible.

Yet, meanwhile the Teramobile has a more powerful femtosecond oscillator, giving rise to the hope to work at higher energy levels, at which the energy dependence of the triggering probability is less pronounced. A campaign will be dedicated to this objective in the near future.

5.4 Triggering and guiding under rain conditions

In chapter 4 we have shown that the filamention can survive in adverse ambient conditions, such as strong turbulence, reduced atmospheric pressure and rain. In the laboratory, it was shown that the filaments can survive the interaction with water droplets [CBK$^+$03].

However, these encouraging results do not assure that the filament also maintains its triggering and guiding ability of discharges. Only one publication, using a CO_2-laser, has investigated the influence of humid conditions on the triggering process [SMAW93]. This lack of investigations can be easily understood, as high-voltages along with water is a dangerous mixture, requiring a deliberate planning. Therefore, we performed experiments in this purpose. These experiments are up to know still the only ones available at this level of realism. They have been published in *Applied Physics Letters* [ASR$^+$04].

5.4.1 Experimental setup
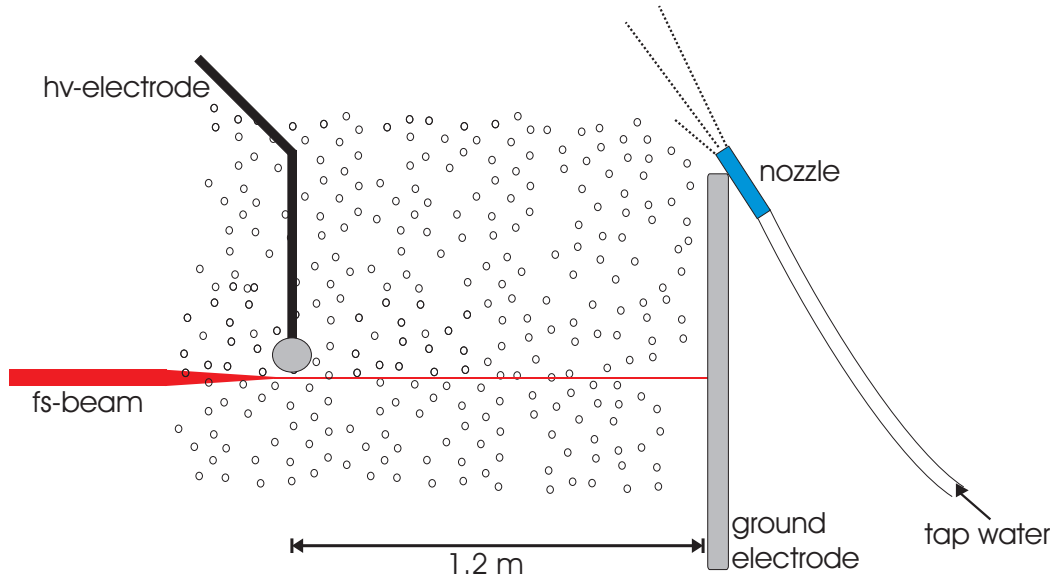
Figure 5.20: The setup of the high-voltage experiments under rain conditions. The water was sprayed into the gap by four nozzles, fixed at the top of the ground electrode.

The experimental setup is similar to that used in section 5.2. The laser was always shot about 6 µs after the start of the high-voltage pulse. Figure 5.20 displays the principle of the rain simulator. Four nozzles were mounted at the top of the ground electrode, producing on demand a water flow of about 1.4 mm/min. This corresponds to a heavy rain, occurring only in a thunder-shower for several minutes [Uma01].

The extinction coefficient of the cloud was measured with a powermeter at the position of the ground electrode, by comparing the transmitted energy of the laser beam with and without rain. The coefficient was measured to be $\alpha = 0.14$ m^{-1} over 3 m. The density of the droplets was estimated to be $N_d \approx 0.3$ cm^{-3}, leading to an average droplet diameter of about 0.5 mm. The relative humidity within the rain cloud and the temperature were 48 % at 19 °C, whereas the corresponding values without rain were 34 % at 22 °C. The

low humidity within the cloud is due to the fact that the rain is not initiated by condensation like in a natural rain cloud but sprayed into dry air, and the short falling time of the droplets lets them little time to evaporate.

5.4.2 Results and Discussion
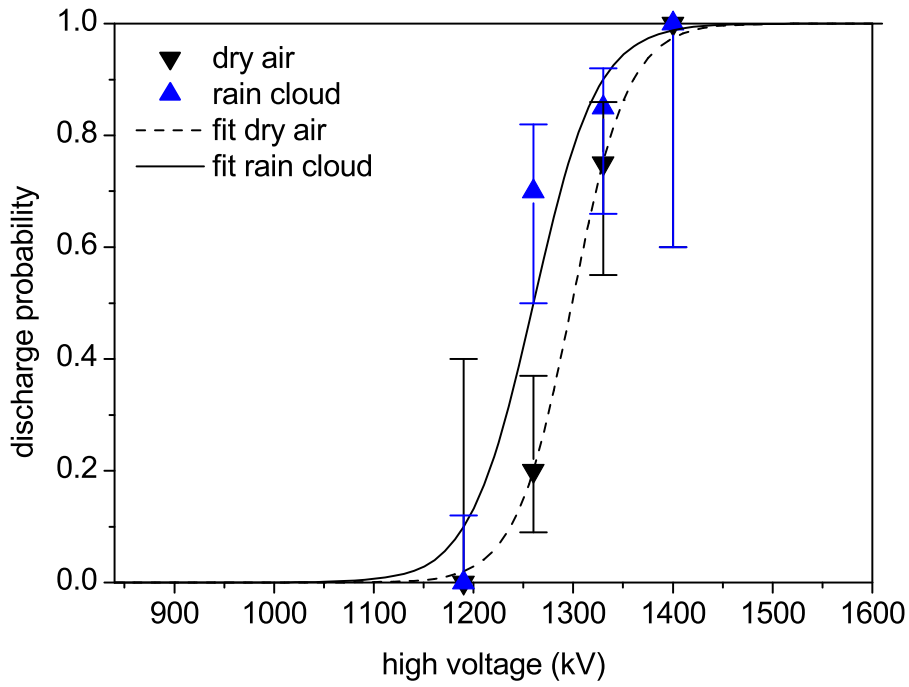
Figure 5.21: Influence of the water cloud on free discharges. The solid lines are hyperbolic fits used to determine the U_{50}. The error bars indicate the confidence intervals.

As the humidity has a great influence on the electric phenomena in air, we first characterized the discharge probability for the dry and rainy conditions without laser. Figure 5.21 shows the probability of a discharge event as a function of the applied voltage. One can see that the discharge probability is slightly higher under rain conditions. The U_{50} in rain is measured to be 3 % lower than in dry conditions. This might be due to slight perturbations of the electric field induced by the dipole moment of the water molecules. Figure 5.22 displays the influence of the rain cloud in the presence of the filament. The
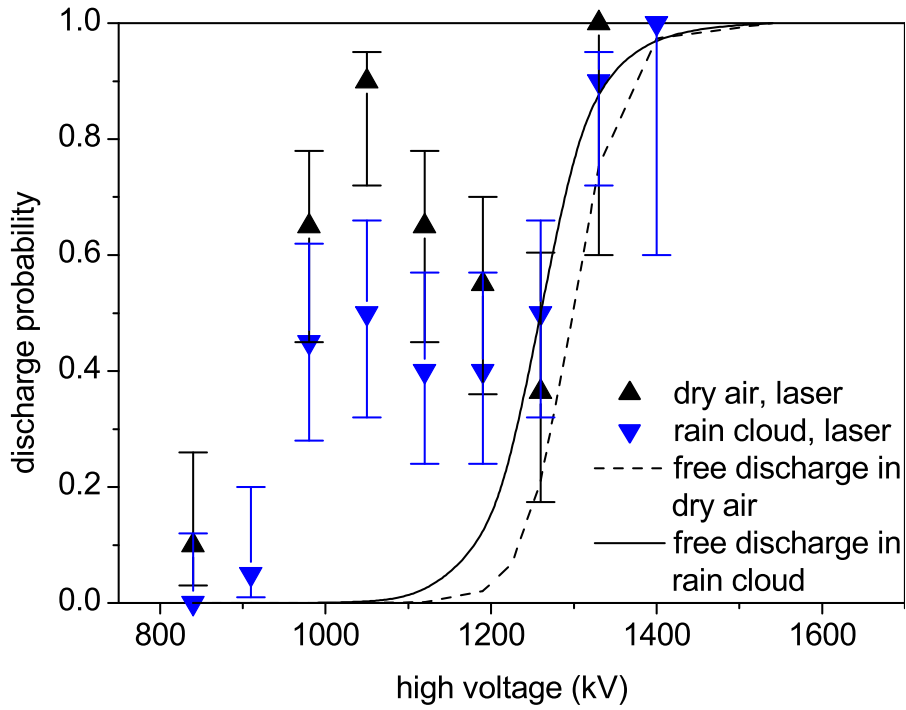
Figure 5.22: The discharge probability as a function of the high-voltage for both rain and dry conditions. The fitted curves without laser are plotted for comparison (see figure 5.21).

rain does not stop the laser triggering, and the dependence on the high-voltage is similar in both conditions. Solely, the triggering probability is reduced by about 30 %.
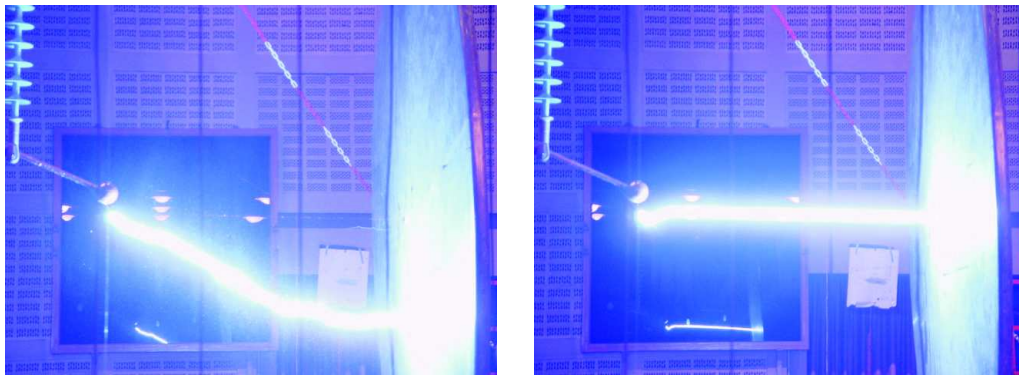
Figure 5.23: The left picture shows a free discharge and the right picture a partially guided discharge in rain. As one would expect, the discharge starts at the tip of the needle, leading to a descending path of the free discharge and the upturn of the free path before the connection to the filament on the right picture.
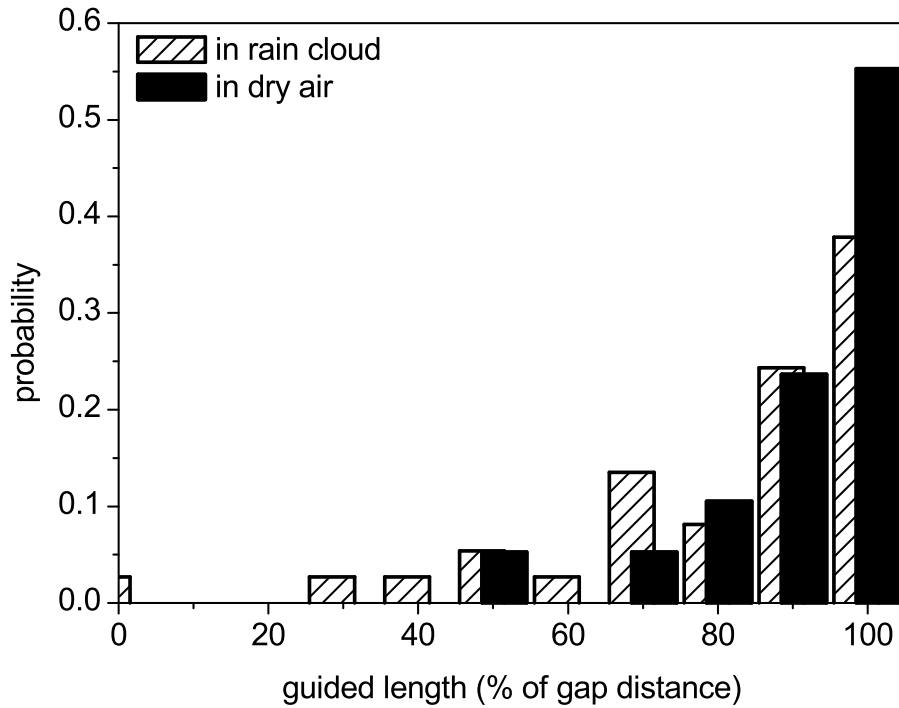
Figure 5.24: The guided lengths expressed as a fraction of the 1.2 m gap in dry air and in rain conditions for triggered discharges. The high-voltage level was 1260 kV.

As already addressed in section 5.2, the shape of the chart with a maximum of the triggering probability is due to a laser alignment slightly higher than the needle tip. At voltage levels above this maximum, the propagating leader is moving away from the laser filament and the probability of a connection to it is reduced (figure 5.23).

Once triggered under rain conditions, the guiding is almost as efficient as in dry conditions (figure 5.24). While the cloud slightly decreases the number of fully guided discharges and allows guiding over less than 70 % of the gap, 90 % of the triggered discharges are guided over at least 50 % of their length, and 60 % of them over more than 90 % of their length.

The triggering and guiding ability of the filaments in rain relies on their ability to survive the propagation through a rain cloud with a similar extinction coefficient [CBK⁺03]. The explanation for this robustness of the filament is
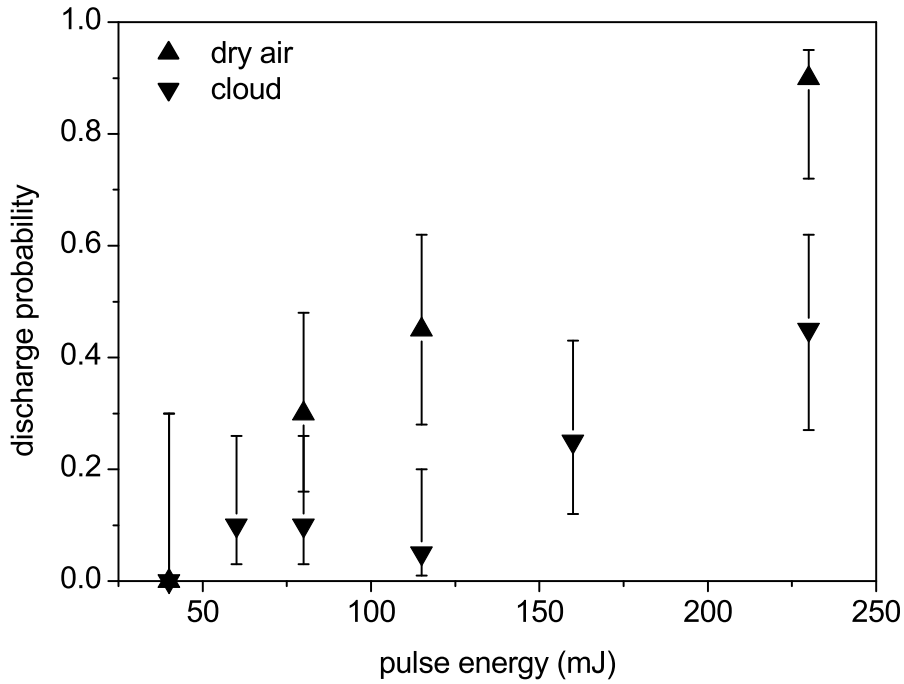
Figure 5.25: Laser pulse energy dependence of the triggering probability at a voltage level of 1050 kV.

the surrounding laser beam acting as an energy reservoir. It enables the reformation of a filament after the interaction with a rain droplet. Therefore, it is the linear extinction coefficient of the rain cloud that imposes the limitation for the triggering and guiding. In order to investigate this effect, the triggering ability in rain has been measured for different laser pulse energies. This is shown in figure 5.25, When reducing the laser energy, the decrease of the triggering probability is faster under rain conditions. However, triggering is possible down to a pulse energy of 60 mJ.

5.4.3 Conclusion

We have shown that an artificial rain cloud, corresponding to a heavy thundershower, does not abolish the triggering and guiding ability of the laser filament. Furthermore, the dependence of the triggering probability on the applied high-voltage is qualitatively similar to dry conditions, although the probability for

a given laser pulse to trigger a discharge is reduced by about 30 %. It can be concluded that the rain encountered in thunderstorms is not a limiting factor for lightning experiments. In addition, the reduced triggering probability will be compensated in the near future by higher laser repetition rates, for which the 100 Hz-regime is not far away from the state-of-the-art, meaning an increase by a factor of ten already.

5.5 Conclusion

Negative high-voltage discharges have been triggered and guided by laser filaments in gaps up to 4.5 m. The plasma lifetime, relevant for laser triggering and guiding, was determined to be about 1 µs. We have shown that the laser is able to trigger space-leader discharges, which could be qualitatively understood within the scope of Gallimberti's model for the streamer-to-leader transition.

In a subsequent experiment, we have shown the improvement of the triggering probability by a dual femtosecond-nanosecond pulse configuration. The results suggest that the effect is based on electron detachment within the leader head of the discharge. The technical problems of a femtosecond-picosecond setup could be identified.

Finally, we have shown that the filaments maintain their ability to trigger and guide high-voltage discharges under artificial rain conditions. The slightly reduced triggering probability will be compensated by higher laser repetition rates in the near future.

6 Optimal control of filamentation in air

After the experiments described above have investigated the capabilities of present techniques to generate filaments in the atmosphere, the next chapters will describe two experiments that will exceed them. This chapter concerns the influence of the optimization of the temporal pulse shape on the white-light and plasma generation.

Since the advent of ultrashort laser pulses (*e. g.* [FGS81]), there has been the wish not only to the accept the pulse "as it is" but to exert also influences on its properties in a desired way. Besides the long-known effect of an initial focusing of the beam [DM69], the effects of the initial pulse chirp [MCA+04, MMA+05, GKK03, RBM+04, WRK+02], spatial filtering [KAS+05], beam profile [FI00], pulse energy [MKY+05], initial focus [SBP+04], and polarization [YZZ+05] have been investigated.

The development of phase modulation masks, described in section 2.4, allowed more subtle influence on the temporal pulse shape via the Fourier-transformation, by introducing a deliberate phase shift on the different components on the broadband spectrum of the ultrashort pulse. However, those masks typically consist of 100 - 1000 pixels that can take several hundred different values, resulting in a search space of about 1000^{100} possible solutions. Thus, sophisticated optimization algorithms are required, and the great breakthrough

was achieved by the application of evolutionary algorithms [JR92]. The capability of this optimization technique was successfully applied in a multitude of experiments for coherent control of atomic and molecular interactions [DL04].

With regard to high-power, large-diameter laser pulses, as produced by the Teramobile, already numerical simulations of the pulse propagation in one given condition are time-consuming, and it is generally not possible to define *a priori* the best laser conditions to optimize a specific property of the filaments. Two easy accessible parameters, characterizing the properties of the filament, are the supercontinuum and the amount of plasma generation in air, and we therefore performed an experiment, using the white-light signal and the sound of the plasma generation, respectively, as the optimization parameters for an evolutionary algorithm. In laboratory, the optimization of the second-harmonic generation was successfully performed, using an evolutionary algorithm [BBS⁺97, BOSG00]. Recently, Heck *et al.* [HSL06] reported the use of a closed-loop optimization of the pulse shape to set the position of filaments in dye-doped water.

The results of this experiment will be published in *Applied Physics Letters* [ASL⁺06].

6.1 Experimental setup

The Teramobile has been installed on the campus of the "Université Claude Bernard Lyon 1" next to the "LASIM" laboratory, where a sufficiently wide area is available, permitting to propagate the beam safely up to a distance of nearly 40 m. The horizontal setup, in contrast to a classical LIDAR experiment, has been chosen in order to have access to the beam profile and to simplify the detection.
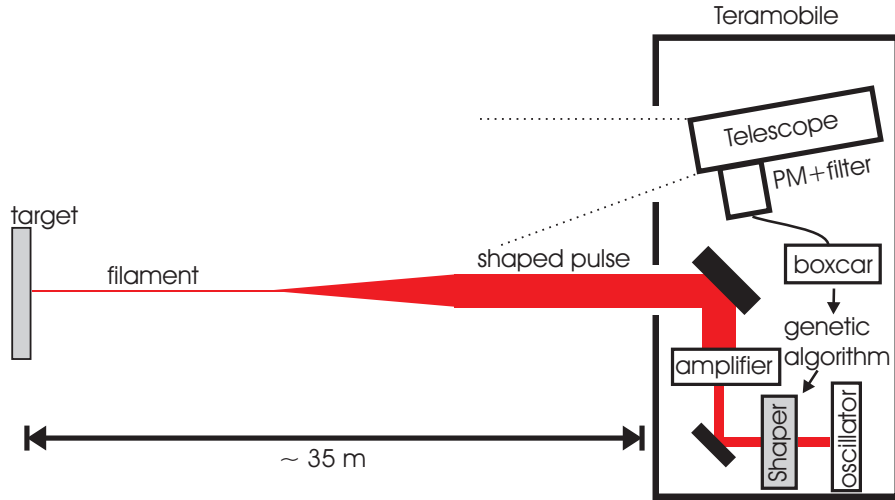
Figure 6.1: Sketch of the setup of the white-light optimization.

A sketch of the setup of the white-light optimization is shown in figure 6.1. The Teramobile laser beam has been shot on a stone that efficiently scatters the light with a fair homogeneity and generates little of nonlinear processes, such as the second harmonic. The beam was sent in the parallel configuration in order to minimize the parameter set for optimization. After each optimization, pictures of the beam profile on a screen have been taken by a commercial digital reflex camera, type "Nikon D70". It was equipped with a macro lens (f = 105 mm) and a RG780-filter that allows to block the continuum generated by the filament. The pictures were taken in 5 m steps starting from the Teramobile container for both the optimized and the unshaped pulse.

The detection system consisted of a commercial telescope, type Vixen "R200SS", with a focal length of 800 mm and a primary mirror diameter of 20 cm, *i. e.* f/4. The telescope was followed by a photomultiplier, type Electrontubes "9829QB", that provides a spectral sensitivity in the range between 160 and 630 nm and a relatively large photocathode surface of 46 mm. Narrow bandpass filters at a central wavelength of 360, 400, 500 nm and a bandpass BG40-filter

(see appendix A) could be inserted to select the wavelength of the continuum which should be optimized.

The photomultiplier signal was connected, via a boxcar integrator, to a personal computer that used the boxcar signal as the input parameter for the optimization, hence, for the control of the pulse shaper apparatus. Integration times of 5 s, *i. e.* 50 laser pulses, has led to the best compromise between signal stability and holding time.
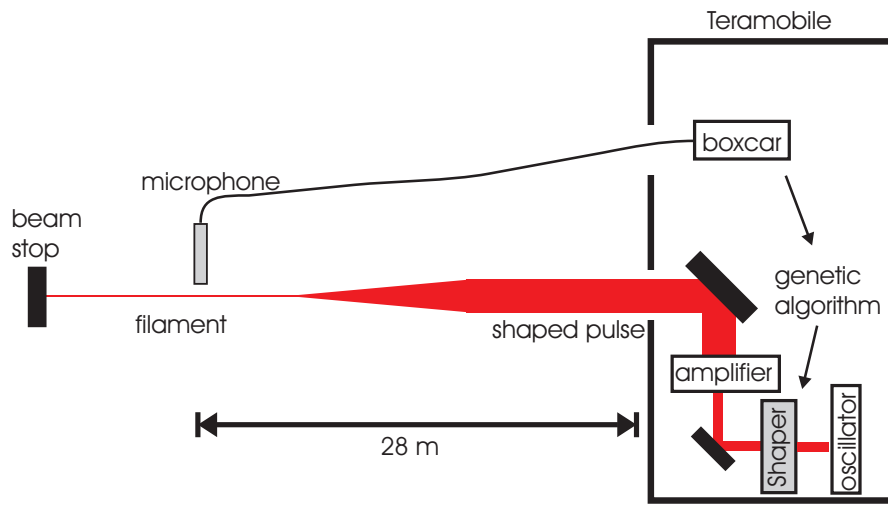
Figure 6.2: The setup for the sonometer optimization. The sonometer was placed at a distance of 28 m from the container.

The sketch of the setup for the sonometer optimization is shown figure 6.2. The "Teramobile" laser beam has been sent outside under the same conditions as described above. Although not necessarily required, the stone was left on its position for security reasons. The microphone that records the sound of the ionizing filament, was placed at a distance of 28 m from the container, and the amplified signal was directly connected to the boxcar integrator, now using the acoustic signal as the parameter to be optimized. The procedure of the picture acquisition was the same as above.

In this experiment, a mask consisting of liquid crystals, type "SLM-128" (Cambridge Research & Instrumentation, Inc.) [Cam04, Bar02] was used for the phase modulation, providing 128 pixels. As the damage threshold of those masks is on the order of a few milijoule per pulse, the setup had to be installed before the first amplification stage. We installed the shaper setup downstream from the pulse stretcher, shaping picosecond pulses with an energy of several nanojoule. Due to the limited space in the Teramobile container, the breadboard was installed above the pulse stretcher housing (see figure 3.4), using a periscope construction for the beam lift. Placing the setup before the amplification stages has the advantage that energy losses originating from a reduced transmission of the shaper masks, may be regained, as especially in a regenerative amplifier saturation occurs [Wei00]. On the other hand, an independent pulse characterization at the laser exit is indispensable, as it is probable that the amplification is dependent on the shaped input pulse. Those influences are up to know only rarely investigated. However, a simple double pulse setup [LWM+95] already revealed additional sub-pulses and a wavelength-shift of the spectrum after amplification. In order to prevent damage to the subsequent amplifiers, we restricted the shaping to pure phase modulations, which means $R(\omega) \equiv 0$ according to equation (2.45). The voltage applied to the electrodes can be adjusted between 0 and 10 V in 4096 steps. The dependence of the phase retardance on the applied voltage has to be calibrated, however, the experience has shown that, once calibrated, there is only a small difference, when the shaper is installed in another laser chain. Therefore, a previous calibration has been used [Lup04]. In order to avoid any amplitude modulation, due to a possible slight miscalibration, the entrance and exit polarizers have been removed.

The pulses were characterized by using a single-shot SHG-FROG [DTHW94] [TDF+97] setup, installed at the exit of the pulse compressor. The following

relation holds for the recorded FROG-trace

$$I(\omega, \tau) = \left| \int\limits_{-\infty}^{\infty} E(t)E(t-\tau)e^{-i\omega t} \mathrm{d}t \right|^2 . \tag{6.1}$$

As only a second order nonlinearity is utilized, it is a very sensitive technique, for which pulse energies in the picojoule regime are sufficient, but the sensitivity is purchased by two ambiguities [Tre00]. If two or multiple pulses are analyzed, the relative phases Φ_0 and $\Phi_0 + \pi$ yield the same FROG-trace. A more severe constraint is that also the original field $E(t)$ and its complex-conjugated, time reversed replica $E^*(t)$ yield the same trace. As $E^*(t)$ corresponds to $I(-t)$ and $-\Phi(-t)$, the original and the time-reversed replica cannot be distinguished, as well as the sign of the chirp. Nevertheless, a common procedure to solve this problem is to modify the chirp of the test pulse in a known manner, *e. g.* by acquiring an additional FROG-trace, after the test pulse has propagated through a dispersive medium. Only one of the retrieved pulses is then consistent with this precondition, and this, in turn, allows to draw the inference which solution for the unmodified pulse has to be chosen.

Due to the limited space in the Teramobile container, the FROG-apparatus had to be reinstalled and aligned for each pulse characterization. Therefore, the FROG-traces have been recorded for only a few selected pulses. The free software package "FROGGUI", which makes use of the "Generalized Projections"-algorithm [DFT$^+$94], has been employed for the pulse retrieval.

The optimization algorithm

We used the implementation of a genetic algorithm close to the one that has been successfully employed for the feedback control of molecular processes [Lup04, Web03]. As the algorithm has been adopted without any principle modifications, only a qualitative overview is given in this paragraph. For a comprehensive description of the particular implementation used in this ex-

periment the reader is referred to the Master thesis of S. Weber [Web03].

The term "genetic" already indicates that the algorithm is based on analogies of biological evolutionary strategies, which are in particular the combination of randomness with the principle of the "survival of the fittest". There are different kinds of possible variations for the implementation of a genetic algorithm, but in principle they all work as follows: At the beginning, a generation of n individuals is created randomly. In this experiment, an individual corresponds to the array of 128 different phase modulations that are applied to the pixels of the shaper masks. We chose a number of 30 individuals per generation. Then each individual is tested for its fitness, hence, the intensity of the detected white-light signal and the amplitude of the recorded noise of the plasma generation, respectively. A predefined percentage of individuals that have shown an insufficient fitness, are discarded, and the remaining individuals are crossed among each other in order to form the next generation. Optionally, the individuals' properties can be modified to a certain extent by random mutation processes.

The actual implementation used the *adaptive mutation* along with the *linear cross-over* strategy. *Adaptive mutation* means that each individual has an additional mutation parameter that specifies its variability to mutation, and with a growing optimization success the mutation parameter is decreased.

Linear cross-over means that for each property (or gene), the parent from which it is inherited, is randomly chosen. In the case of the pulse shaper, a gene corresponds to the phase modulation that is applied to an *individual* pixel. As the linear cross-over mechanism simply selects the parents' genes, new properties, *i. e.* new values of the phase retardance, may only be created by mutation processes.

Two slight modifications of the original algorithm were implemented: The possibility to replace a certain number of individuals after each generation by new

randomly created ones, so-called "aliens", whose number we have set to one per generation. This procedure is to avoid that the algorithm runs into a local extremum too quickly.

Secondly, the signal of a *reference* mask, applying a zero phase shift to all pixels, was recorded after each generation in order that laser fluctuations during the optimization could be identified.

6.2 Results and Discussion
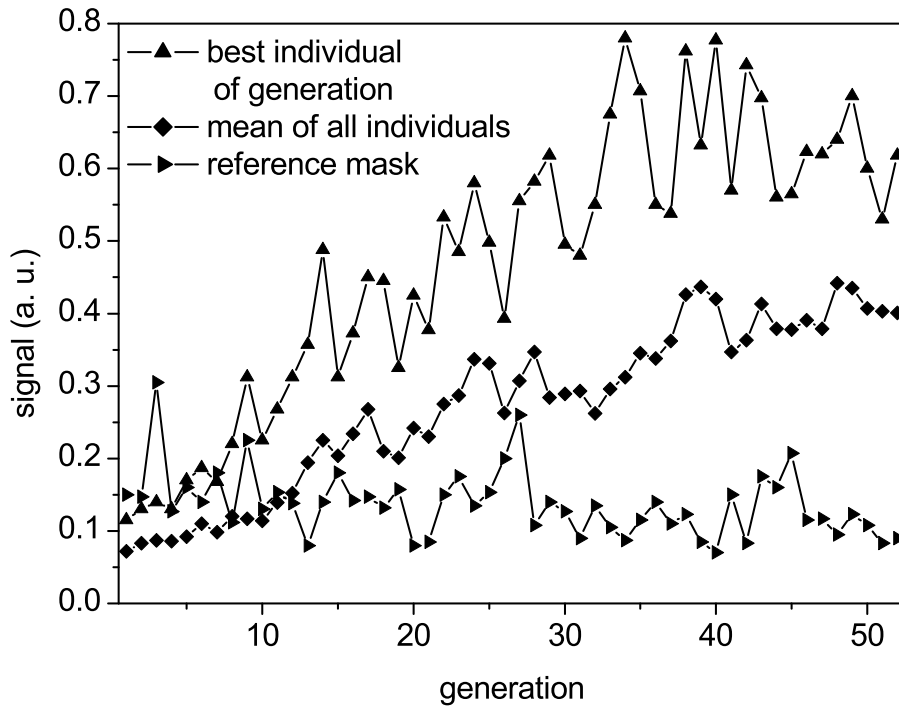
Figure 6.3: History of an optimization with a 360 nm filter.

We first performed optimizations using the full resolution of the SLM and narrow bandpass filters at 400 and 500 nm and a broadband BG40-filter. In all cases, the white-light signal first disappeared after the launch of the optimization due to the randomized phase masks. It turned out that the search space was too large for the random mutation to identify regions where the sig-

nal would reappear within a reasonable time. Therefore, we virtually reduced the number of pixels by grouping neighbouring pixels and assigning them to the same phase shift. We started with a binning of the pixels 16 by 16, *e. g.* 8 virtual pixels, and subsequently reduced this number if the algorithm had converged. We found a convergence down to a binning of 4 pixels, *i. e.* 32 logical pixels, and we, therefore, decided to continue in this configuration.

Figure 6.3 shows the history of a successful optimization with a 360 nm filter. The algorithm converges within 30 generations (2 hours), after which the constant signal ratios indicate that convergence has been achieved.

The signal of the best pulse is four times higher than the signal of the applied reference mask. The laser fluctuation during this time is indicated by the slight
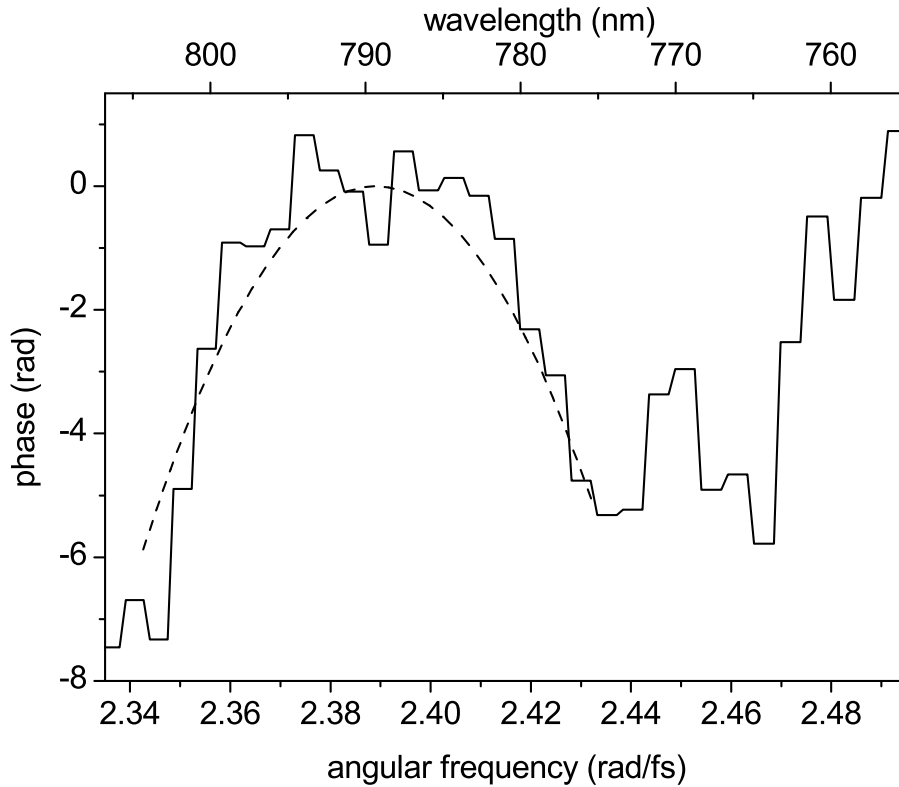
Figure 6.4: Unwrapped phase mask of the optimized pulse for an optimization with the 360 nm-filter. The laser spectrum was centered at $\omega_0 = 2.4 \times 10^{15}$ s^{-1} $\equiv$ 785 nm.

decreasing trend of the signal of the reference mask.

The corresponding optimized mask is presented in figure 6.4. The laser spectrum of the amplified pulses at the compressor exit was centered at $\lambda = 785$ nm, i. e. at $\omega_0 = 2.4 \times 10^{15}$ s^{-1}, whereas the spectrum of the pulses from the oscillator, incident on the pulse shaper, was centered at $\lambda = 795$ nm. The spectrum of the compressor exit depended strongly on the laser alignment, and therefore the exit spectrum was not always in the center of the shaper mask. The unwrapped phase around the center wavelength suggests that the pulse shaper has applied a quadratic phase function, i. e. a linear chirp, for which the fit yields b$_2$ = - 5.4 $\times$ 10^3 fs^2.

The application of a negative chirp is confirmed by the Wigner-plots of both the initial and the optimized pulse shown in figure 6.5 [Wig32]. The Wigner distribution $S(E^+; \omega, t)$ is calculated from the pulse spectrum by [Pay92]

$$S(E^+; \omega, t) = \int_{-\infty}^{\infty} E^+(\omega + \Omega)[E^+(\omega\Omega)]^* e^{2i\Omega t} \mathrm{d}\Omega \qquad (6.2)$$

or the temporal electric field by

$$S(E^+; \omega, t) = \int_{-\infty}^{\infty} E^+(t + \tau)[E^+(t - \tau)]^* e^{-2i\omega\tau} \mathrm{d}\tau. \qquad (6.3)$$
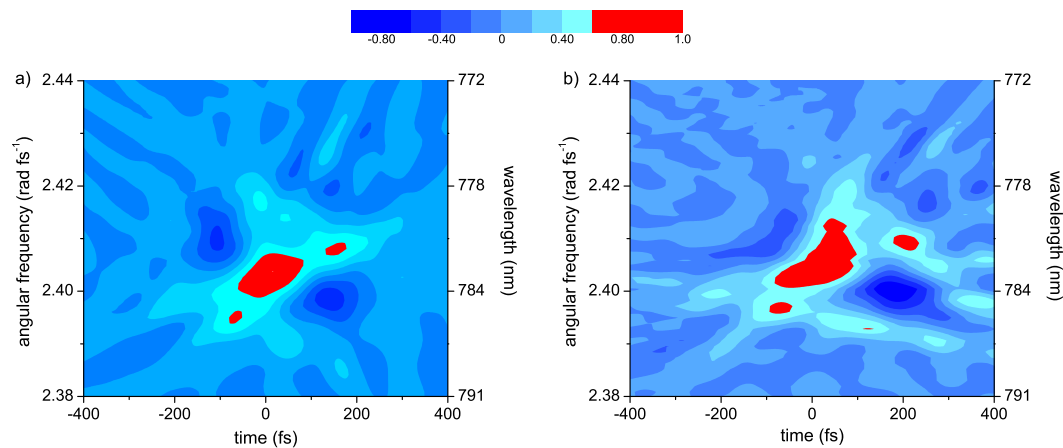
Figure 6.5: Wigner plots of the initial (a) and the optimized (b) pulse for the optimization with the 360 nm filter.
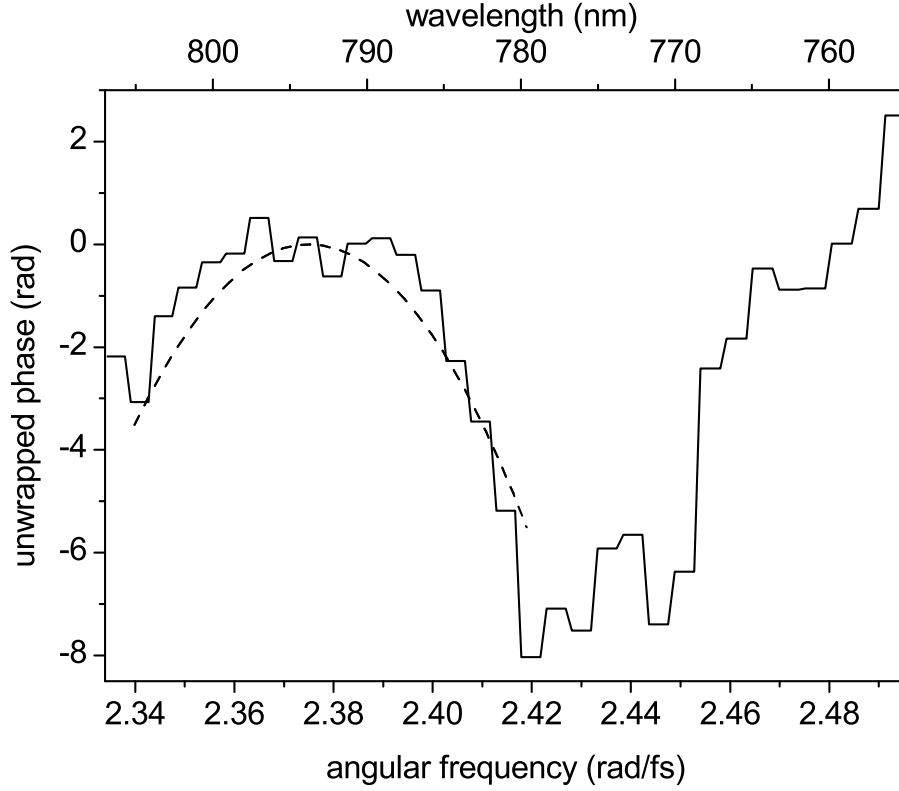
Figure 6.6: Unwrapped phase mask of the optimized pulse for an optimization with the sonometer. The fit yields a linear chirp of $b_2 = -5.68 \times 10^3$ fs^2.

The negative chirp can be identified by a slight counter-clockwise tendency of the *main* pulse, marked as the red area, in figure 6.5(b). The plot of the initial pulse is based on the pulse retrieved from the FROG-trace and the plot of the optimized one is obtained by applying the optimized phase mask on the initial pulse. Actually, moving the compressor grating by 1 mm yielded the same signal improvement as the optimized pulse. According to the compressor calibration, this corresponds to a chirp of $b_2 = -5 \times 10^3$ fs^2, in line with the value obtanied by the fit function.

A similar optimization mask as for the 360 nm optimization has been obtained with the sonometer optimization (figure 6.6), which also indicates the application of a linear negative chirp by the pulse shaper. This is confirmed by the photos of the beam profile taken along the beam path.
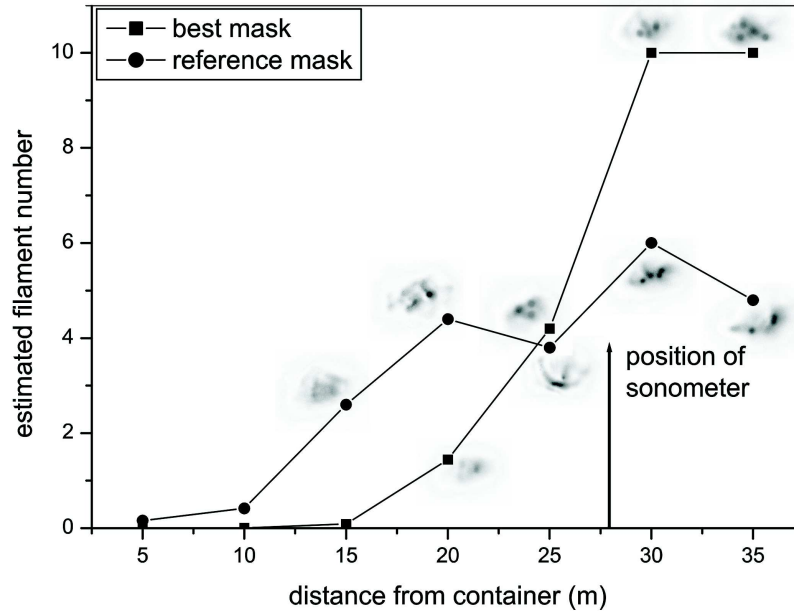
Figure 6.7: The estimated number of filaments as a function of the propagation distance for the reference and optimized mask. The pictures show the inverted, blue layer of the pictures of the beam profile, taken on a screen along the beam path.

The estimated filament number as a function of the propagation distance is shown in figure 6.7, indicating that for the optimized pulse the filaments are created at a greater distance from the container than for the reference mask.

The above results suggest that for the optimization of the supercontinuum as well as of the ionization the optimization mainly results in an application of a linear chirp. However, the decrease of the pixel number to 32 logical pixels also affects the maximum linear chirp that the pulse shaper is able to apply. According to equation (2.57) it amounts to $|b_2| = 8.5 \times 10^3$ fs^2, which is on the order of the chirp that the optimization algorithm finds. This means that, apart from the applied chirp, the original pulse is accompanied by replica pulses, as discussed in section 2.4. Indications for replica pulses are indeed found on the recorded FROG-traces. Figure 6.8(a) shows the FROG-trace of the initial pulse and in (b) the trace of the optimized pulse is shown for the sonometer
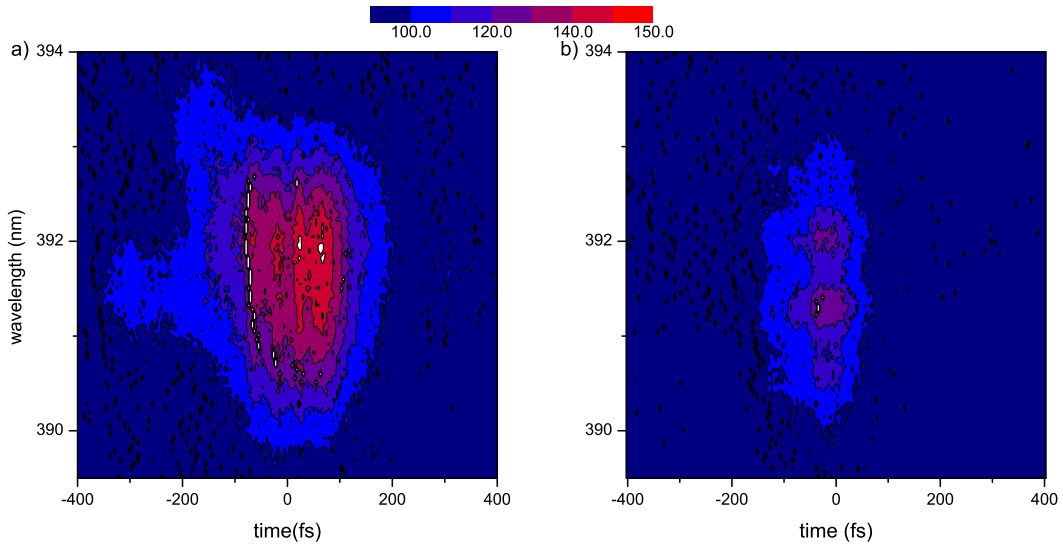
Figure 6.8: Recorded FROG-trace (a) of the unshaped pulse and of the optimized pulse for the optimization with the sonometer (b).

optimization. The horizontal stripe structure in the spectrum of the optimized pulse is a typical sign of multiple pulses [Tre00], but owing to the small time window of the SHG-FROG these pulses were not recorded. Furthermore, the intensity of the trace for the optimized pulse is lower.

The replica pulses mainly introduce two counteracting effects, since on the one hand they decrease the intensity of the main pulse. On the other hand, the intensity gradients of the replica pulses may favour the filamentation process. Therefore, the result of the optimization is most probably a compromise between the application of a linear chirp and these two effects. This assumption is supported by the observation that the optimization with the sonometer yielded an *increased* filament number (see figure 6.7), although one would expect a reduction in the case of the application of a linear chirp due to the reduced intensity.

Furthermore, one optimization with a 400 nm-filter has shown that the algorithm is able to find an optimized pulse shape, whose white-light signal surpasses any application of a linear chirp. This is displayed in figure 6.9. The optimized pulse yielded a signal that is about 30 % higher than that achievable

by adjusting the linear chirp.
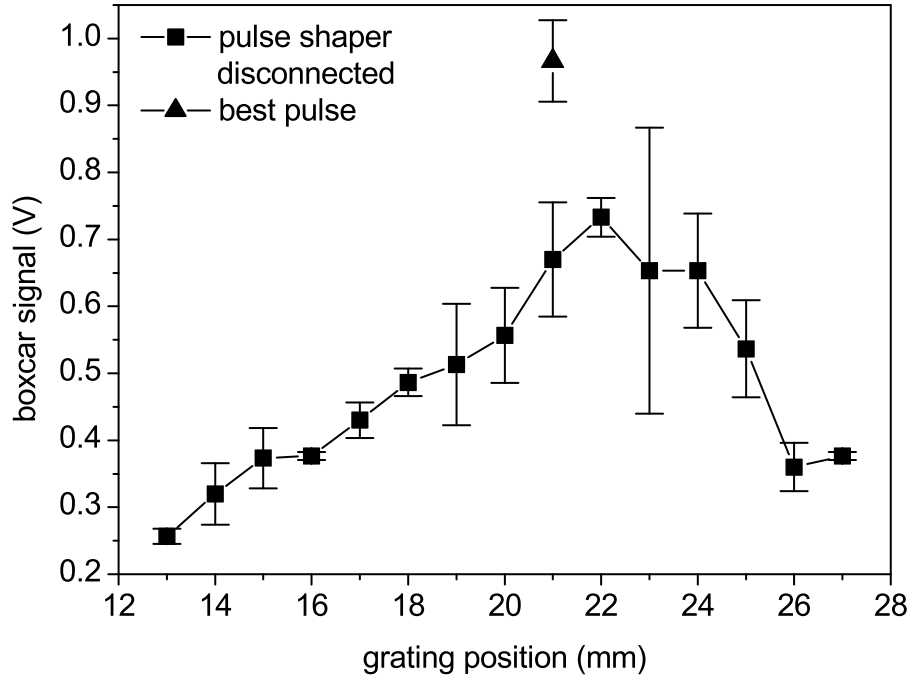
Figure 6.9: The signal at 400 nm for the best pulse and for the pulse shaper disconnected as a function of the linear chirp

6.3 Conclusion

We have shown that both the white-light and plasma generation of a TW-femtosecond laser in atmospheric conditions can be optimized by using a liquid crystal pulse shaper combined with a genetic optimization algorithm. The effect of the optimization seems to be a compromise between the application of a linear chirp and the occurrence of replica pulses.

It has turned out that the laser repetition rate of 10 Hz along with the uncertainty of the initially applied linear chirp restricts the realization of pulse shaping experiments with the Teramobile. In order to achieve convergence of the optimization algorithm in a reasonable time, the pixel number had to be reduced to 32 pixels, severely confining the applicable phase functions. There-

fore, a higher spectral resolution of the pulse shaper may lead to more complex phase compensations than the linear chirp found in this experiment. Yet, such an experiment would necessitate a considerably higher laser repetition rate than provided by the Teramobile.

Further improvements of the experiments with the *present* setup may include the use of a parametric instead of a free optimization, implying the disadvantage that the optimization functions are predetermined. In order to reduce the phase difference between adjacent logical pixels, the binning could be improved by linearizing the phase function between the master pixels. This procedure decreases the intensity of the replica pulses but does not allow to introduce phase functions of higher orders.

7 White-light generation of a 30 TW laser in the atmosphere

The experiments with the Teramobile during the last six years have proven its capability to be successfully employed in experiments on an atmospheric scale [KRM$^+$03]. However, especially the results of the high-voltage experiments (chapter 5) have also revealed its limitations, *e. g.* the possibility to produce long plasma channels with a sufficient lifetime in order to guide a lightning stroke over a large distance. Therefore, there is still a persisting interest to explore the effects of even more intense pulses propagating in the atmosphere.

In order to address the above questions, we conducted an experiment at the CEA/CESTA laser center near Bordeaux, where the *Alisé*-facility provides a multijoule-ultrashort laser system. It surpasses the Teramobile laser in pulse energy by a factor of almost 100 and offers the opportunity to gain new information about the propagation of filaments at long distances. Moreover, its center-wavelength in the infrared ($\lambda = 1053$ nm) may also lead to a significant change of the filament properties, such as the width of the emitted white-light spectrum and the critical power for filamentation. However, one of the most important questions is whether an increase of the pulse energy leads to a significant extension of the filamention length, since the higher energy may also lead to an increased filament number within the beam or even to the beam collapse, forbidding filamentation at all. The experience with the Teramobile

indeed showed that higher pulse energies may lead to the occurrence of multiple filaments due to refractive index gradients in the beam profile [BSL+04].

The pulse propagation and white-light emission of the *Alisé*-laser have been characterized by a combined LIDAR and camera detection. The setup is based on earlier, successful measurements with the Teramobile at the German observatory "Thüringer Landessternwarte" near Jena. In those experiments, the capability of the white-light LIDAR technique provided by the Teramobile could be proven by determining the altitude dependence of the relative humidity [BMK+05]. Furthermore, new insights in the control parameters for the filamentation were gained by taking images of the generated white-light on cloud layers and determining the filamentation onset, as being described in section 2.3 by taking advantage of the fixed divergence angle of the conical emission imaged on clouds. The generated white-light of the filaments was detected up to an altitude of 18 km, and it was measured that, by adjusting the chirp, filaments were generated up to an altitude of 2 km [RBM+04].

By comparing those results with the propagation of the high-intensity pulses of the *Alisé*-laser, the effects of increasing both the pulse energy and intensity have been be evaluated. The first results of this experiment have been submitted to *Nature Physics*.

7.1 Experimental Setup

Like the Teramobile, the Nd:glass-laser at CEA-CESTA Bordeaux is a chirped pulse amplification system, but with six subsequent amplification stages at a center-wavelength of $\lambda = 1053$ nm. The pulse duration during the experiments could be varied between 550 fs and 60 ps by the movement of one of the compressor gratings. The maximum pulse energy of the laser was 26 J, leading to a peak intensity of 32 TW for the shortest pulse. Due to thermal effects

within the laser chain, the time between two successive shots of the laser depended on the pulse energy of the preceding shot. A shot with the full energy of 26 J led to a delay of about 1 hour until the next event, whereas the minimum delay was 15 minutes for pulse energies of 300 mJ. The beam has been directed from the laser hall into an auxilliary room, where the beam diagnostics and the pulse compressor were installed, and the beam exited the room through a port in the roof.

The backscattered white-light signal was detected by a LIDAR system, consisting of the telescope (20 cm, f/4) described before (chapter 6). It was equipped with three photomultipliers, two of them providing a spectral sensibility between 300 and 650 nm (type Hamamatsu "H7826"), and one in the range of 300 - 850 nm (type Hamamatsu "H7826-01"). These models have a large photocathode diameter of 15 mm, providing a field of view as large as 20 mrad. In order to select the detected part of the supercontinuum, dichroic mirrors followed by narrow bandpass and/or broadband filters were inserted (see appendix A). The telescope was placed at a distance of about 50 cm from the sending mirror. Since it was not possible to adjust this mirror, the LIDAR signal was aligned by the motorized tripod of the telescope.

Simultaneously, the beam was photographed from the side at off-axis distances between 5 and 30 m by a ICCD camera, type Andor "DH734" that provides a resolution of 1024 x 1024 pixels. The camera was connected to a home-made telescope with a focal length of 1.2 m and a primary mirror diameter of 40 cm, *i. e.* (f/3). The spatial resolution of this setup was 1 µrad, providing a field of view of about 10 mrad. Pictures were acquired either without or with a broadband BG39-filter, respectively.

Additionally, the beam was photographed by a commercial digital reflex camera (type Nikon "D70"), equipped with a f = 105 mm lens. Alternatively, the beam profile was recorded by taking burns on photosensitive paper after about
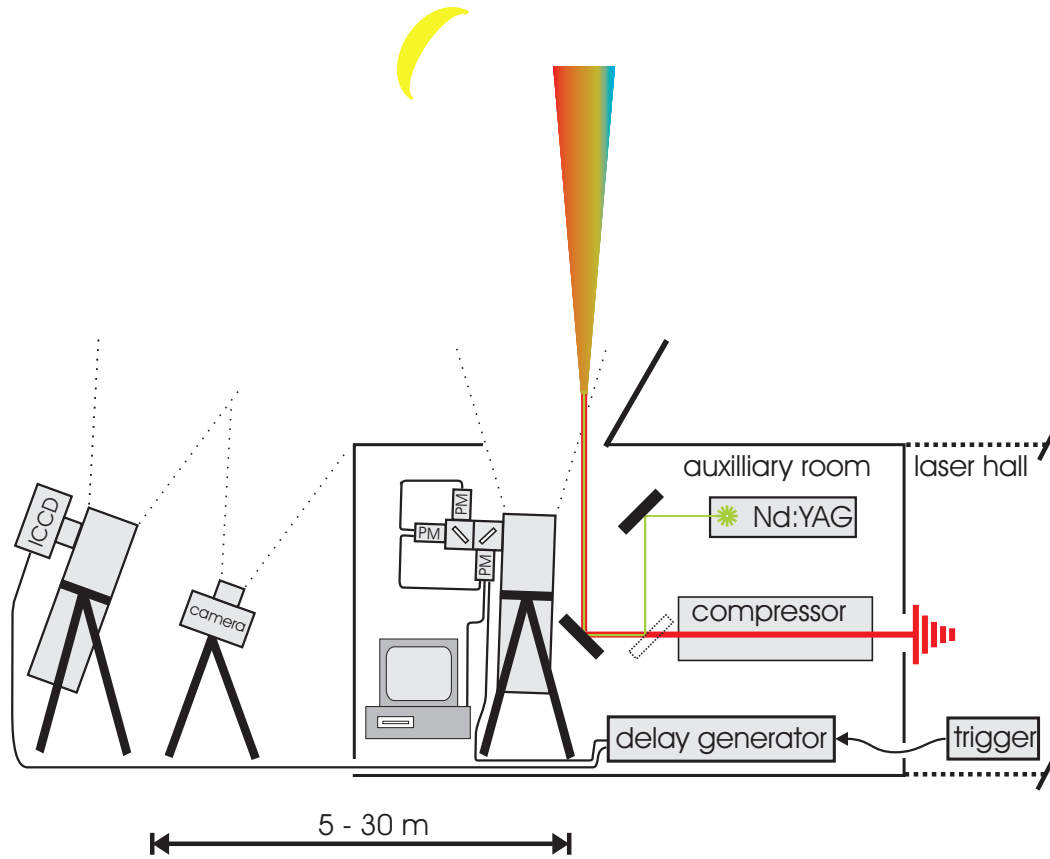
Figure 7.1: The setup of the detection at the CEA-CESTA laser facility. The LIDAR-telescope was placed at a distance of 50 cm from the sending mirror.

10 m of propagation of the compressed pulse. The whole setup of the detection is sketched in figure 7.1.

Owing to the single shot experiments, the detection had to be aligned on a green Nd:YAG-laser working at $\lambda = 532$ nm, providing a pulse energy of up to 200 mJ at 10 Hz. In addition, the femtosecond laser could be operated as a "pilot" in a low energy mode at 1 Hz, with which the overlap of the Nd:YAG was aligned on the exit window on the roof. The estimated uncertainty about the overlap of both lasers is $\Delta l \approx 2$ mrad, *i. e* is 5 - 10 times smaller than the field of view of both telescopes.

A secure triggering is crucial for single shot experiments. The LIDAR detection and the ICCD camera were sent a laser trigger that could be adjusted in a range

of several hundred microseconds, before the laser pulse arrived in the auxilliary room. For the LIDAR detection, the correct delay was checked by using the photodiode signal of the laser working in the low energy mode. The altitude recorded by the ICCD-camera was calibrated by relating the position of the Nd:YAG laser pulse on the picture to the position time window of the camera.

7.2 Results and Discussion
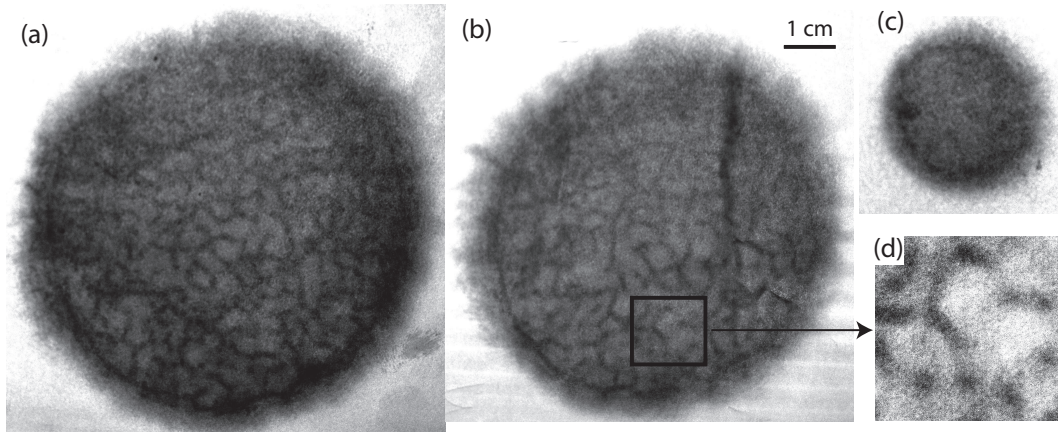
Figure 7.2: The beam profile after a propagation of about 10 m. In (a) the beam was sent in parallel configuration, in (b) and (c) the geometrical focus was set to f = 300 m and 15 m, respectively. (d) shows a zoomed part of the filament structure.

Fiugre 7.2 shows the beam profile on impact paper for different laser energies, geometric focus and chirp. In 7.2(a) the pulse has the maximum energy of 26 J at 800 fs. As in the case of the Teramobile, multiple filaments develop due to refractive index gradients within the beam profile. Yet, while within the Teramobile beam typically 10 - 20 filament develop, we have counted more than 400 filaments here. The filaments appear along linear structures, and the high intensity of the individual filaments is confirmed by their capacity to locally ablate the surface of the paper within a single shot. Typically one filament is observed for each 3.5 to 7.5 critical powers P_{crit} (equation (2.33)) that is compa-
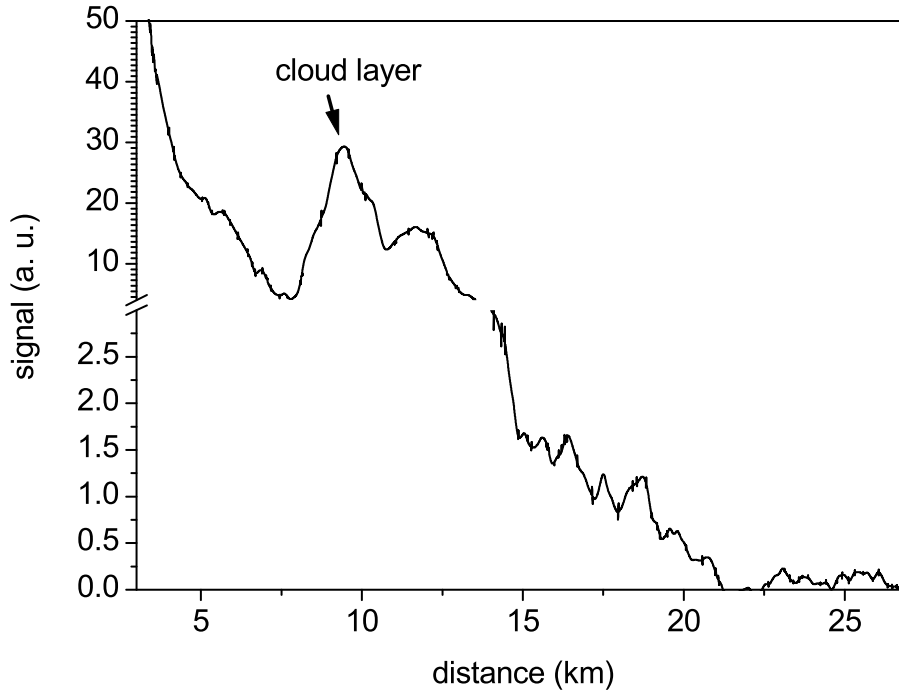
Figure 7.3: Detected LIDAR-signal for a laser shot with an energy of 26 J and a duration of 800 fs between an altidude of 3 and 25 km. The small peak at 10 km arises from a thin cloud layer. Due to the high dynamics of the signal, the vertical axis is shown discontinuously.

rable to the Teramobile beam [MKY$^+$05], where a value of 5 P_{crit}/filament was measured. In Figure 7.2(b) the geometric focus was set to 300 m at about 2200 critical powers, leading to a reduction of the number of filaments to 290. At a geometric focus of 15 m and 3200 critical powers (figure 7.2(c)) no filaments have been observed. These results show that, in spite of the high-intensity of the *Alisé*-beam, the beam does not collapse but allows the formation of filaments as in the case of lower intensies.

The ability of filamentation to prevent the beam from collapsing due to the self-focusing effect is confirmed by the detected LIDAR signals. The signal was detected over the whole visible spectrum from 360 nm to 850 nm. Figure 7.3 shows the LIDAR signal generated by the white-light laser beam in the 300-475 nm band, as a function of altitude. The signal can be clearly observed up to more than 20 km, although the considered spectral region is in the visible
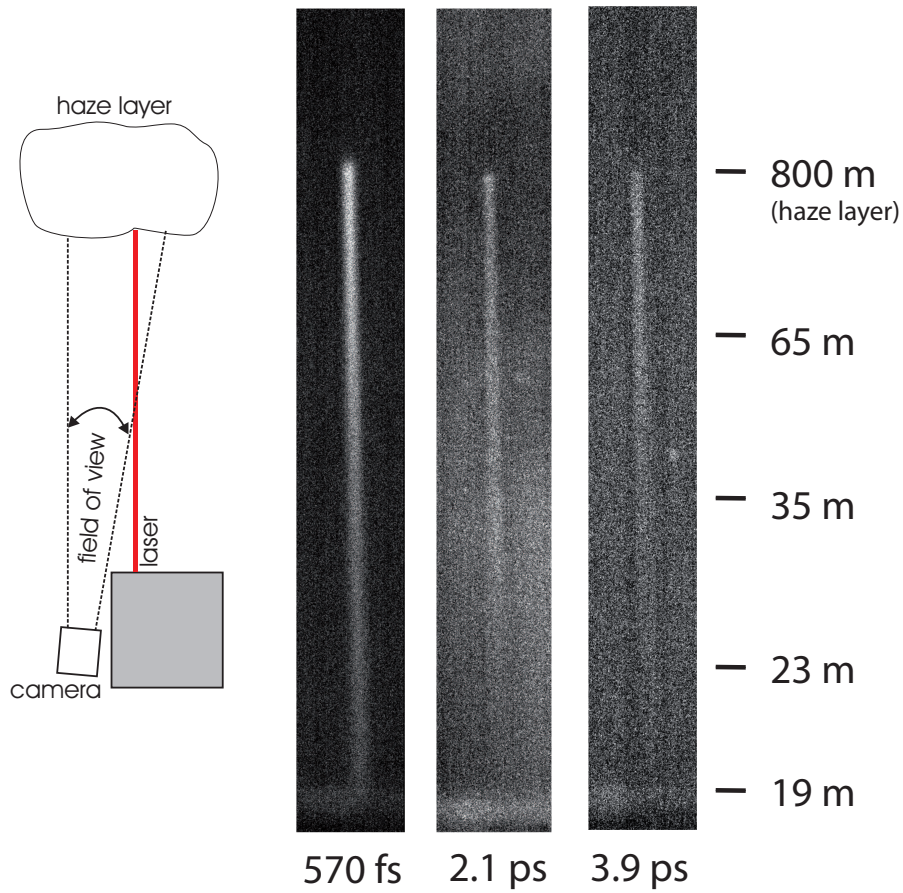
Figure 7.4: Photographs of the emitted white-light for three different chirps.

and more than 600 nm away from the fundamental infrared wavelength. So far, this is the highest altitude at which a white-light LIDAR signal has been detected.

Another key parameter for the application of ultrashort-terawatt lasers in the atmosphere is the control of the filamentation onset by the variation of the initial chirp as demonstrated at lower power [RBM+04, WRK+02]. This has been measured in two ways. In figure 7.4 pictures of the emitted white-light are shown for three different initial chirps. It is remarkable that even for a pulse duration of 6 ps the filamentation starts below an altitude of 19 m, which is below the field of view of the detector. This short self-focusing length z_f may be explained by recently reported numerical simulations that it scales

with $1/P_{in}$ for high power lasers, in contrast to the Marburger formula (2.34), where $z_f \propto 1/\sqrt{P_{in}}$ [CB06, FEI$^+$05].

A quantitative analysis of the emitted intensity, by normalizing the emitted light with the photos of the linearly propagating Nd:YAG beam, indicates that for the shortest pulse ($t_d = 570$ fs) the filaments stop at an altitude of 100 m, whereas pulse durations of 2 and 4 ps led to a filament length of 350 and 200 m, respectively. These lengths are comparable to the lengths measured on the Teramobile beam [MDA$^+$05] for similar peak powers, although the energy is much higher in the present experiment.

The dependence of the filament length on the initial chirp is also confirmed by the LIDAR measurements shown in figure 7.5, where the shift of the filament end, convolved with the vertical evolution of the geometrical overlap between the beam and the LIDAR detector, results in a shift of the maximum of the LIDAR signal to higher altitudes.
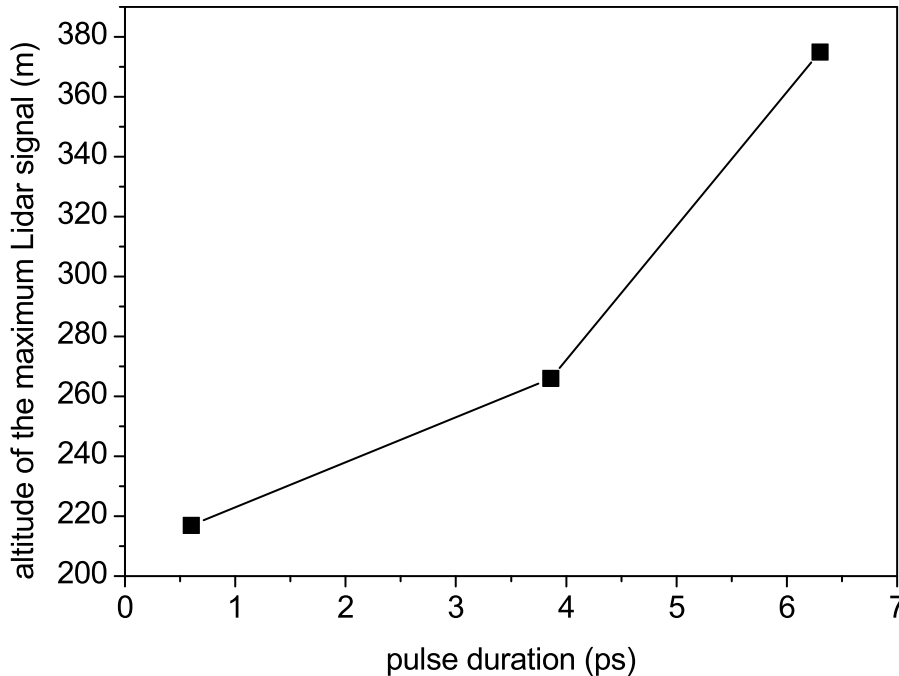
Figure 7.5: The maximum of the detected white-light emission as a function of the initial pulse duration.

7.3 Conclusion and Outlook

We have shown that ultra-intense laser beams with a peak power of up to 32 TW and pulse energies beyond 20 J do not collapse during their propagation through the atmosphere, but generate multiple filaments through processes similar to those observed for sub-Joule pulses. The produced supercontinuum propagates up to the stratosphere, *i. e.* beyond 20 km, constituting the highest power "white-light laser" to date. Also, filamentation can be controlled by varying the chirp and energy of the emitted pulses.

However, the résumé of these experiments still may be more an outlook rather than a conclusion, as the analysis of the results is still in progress at the time of the completion of my thesis. Quantitative statements on the generated white-light spectrum may be achieved, based on the evaluation of the LIDAR signals for selective wavelengths within the supercontinuum. The photos of the ICCD+telescope detection that took pictures of the white-light projected on the cloud layers, may also allow to draw more precise conclusions on the filamentation onset along with the possibility of a precise determination of the filament lengths by means of the LIDAR measurements.

8 Conclusion

This work has investigated the development and propagation of laser filaments in the atmosphere, and their application to the triggering and guiding of high-voltage discharges.

We have shown that the filaments survive the propagation through turbulences with magnitudes that are higher than may be encoutered in the atmosphere, and it was measured that the pointing stability of the filament behaves simelarly to the surrounding beam. In addition, we have proven that the filaments are able to develop at a reduced pressure of 0.7 atm and that the achievable filament lengths are comparable to results at sea-level. Furthermore, the formation and propagation of filaments in rain under these conditions have been shown. These results have confirmed the ability of long filaments to be employed for LIDAR measurements on a large scale and encourage further research aiming at the control of lightning.

With regard to the application of filamentation to the triggering and guiding of discharges in air, its capabilities and limitations have been determined more precisely. We have shown that in the case of long laser filaments, it is the free electron density, which is responsible for the triggering and guiding process. The electron density decay time has been measured to be about 1 µs. The triggering and guiding mechanism, as well as the ability of the filament to trigger space-leader discharges, are qualitatively understood in the scope of Gallimberti's theory for the streamer-to-leader transition.

In order to enhance the limited plasma lifetime, we successfully increased the triggering probability of laser guided discharges, by a dual fs-ns laser pulse setup. Although, in our case, the effect of the nanosecond laser might have been restricted to a facilitated streamer-to-leader transition within the leader head of the discharge, the general possibility of an improved laser triggering and guiding by electron detachment has been proven. With regard to thunderstrom experiments, it has been shown that the filament maintains its triggering and guiding ability under rain conditions, solely leading to a reduced triggering probability of about 30 %.

The improvement of the white-light generation as well as the plasma generation by a closed-loop pulse shaping optimization has been successfully performed for the first time at the terawatt power level, in spite of the strong experimental difficulties due to the low laser repetition rate. Although the present setup seems to restrict the optimization to the application of a linear chirp, there is evidence of possible nonlinear optimization processes.

Finally, by investigating the propagation of a multijoule-terawatt laser pulse in the atmosphere, we have shown that filamentation is still possible at these extreme power levels and that the increase of the pulse energy and intensity is a possibility to enhance the application range of filamentation experiments.

9 Outlook

The results of this work have led to more or less concrete plans for further experiments.

Concerning the filamentation under adverse conditions, a major issue is to perform turbulence experiments under more realistic conditions. This means to enhance the turbulent perturbation from a laboratory to an atmospheric scale, investigating its influence on the Teramobile beam.

With regard to the high-voltage experiments, the encouraging results of the femtosecond-nanosecond configuration suggest further experiments, investigating systematically the influence of the energy of the nanosecond pulse and the delay between both pulses. The femtosecond-picosecond setup will be still an alternative when it is possible to compensate the decrease of the triggering probability due to the energy losses. A campaign that will address these issues is scheduled for autumn 2006 at the high-voltage facility of the "Ecole centrale de Lyon", being further encouraged by recent, successful experiments of Zhu *et al.* [ZJD+06] on a small scale.

Although the pulse shaping experiments have shown some indications of possible nonlinear optimization processes, further experiments will necessitate a considerable augmentation of the laser repetition rate. This would allow to increase the number of pixels on the pulse shaper mask, enhancing the ensemble of applicable phase modulation functions.

Although the analysis of the experiments of the multi-terawatt experiment at

the *Alisé*-facility has not yet been concluded, the preliminary results indicate that statements on the filament parameters, such as their onset or length, may be difficult when they are solely based on the recorded LIDAR-signals. Therefore, a horizontal propagation experiment is currently being planned and probably scheduled for 2007, offering direct access to the beam.

A Filter specifications

Narrow bandpass filters

Filtertype	center wavelength	FWHM	max. tansmission
LC360NB5-F (Lasercomponents)	360 nm	5 nm	20 %
LC400NB5-F (Lasercomponents)	400 nm	5 nm	30 %
LC500NB5-F (Lasercomponents)	500 nm	5 nm	45 %

Bandpass filters

Filtertype	range of 50 % transmission min.	description
BG39	350 - 580 nm	visible white-light spectrum
BG40	340 - 610 nm	visible white-light spectrum
RG780	$\lambda > 780$ nm	blocks the white-light spectrum

Dichroic mirrors

Filtertype	50 % transmission min.
475FD68-25 (L.O.T.-Oriel)	$\lambda > 473$ nm
580FD70-25 (L.O.T.-Oriel)	$\lambda < 559$ nm

B List of publications

1. **R. Ackermann**, G. Méchain, G. Méjean, R. Bourayou, M. Rodriguez, K. Stelmaszczyk, J. Kasparian, J. Yu, E. Salmon, S. Tzortzakis, Y.-B. André, J.-F. Bourrillon, L. Tamin, J.-C. Cascelli, C. Campo, C. Davoise, A. Mysyrowicz, R. Sauerbrey, L. Wöste, and J.-P. Wolf. Influence of negative leader propagation on the triggering and guiding of high-voltage discharges by laser filaments. *Applied Physics B*, 82(4):561 - 566, 2006.

2. **R. Ackermann**, K. Stelmaszczyk, P. Rohwetter, G. Méjean, E. Salmon, J. Yu, J. Kasparian, V. Bergmann, S. Schaper, B. Weise, T. Kumm, K. Rethmeier, W. Kalkner, L. Wöste, and J.-P. Wolf. Triggering and guiding of megavolt discharges by laser-induced filaments under rain conditions. *Applied Physics Letters*, 85(23):5781, 2004.

3. **R. Ackermann**, G. Méjean, J. Kasparian, J. Yu, E. Salmon, and J.-P. Wolf. Laser filaments generated and transmitted in highly turbulent air. *Optics Letters*, 31(1):86, 2006.

4. **R. Ackermann**, E. Salmon, N. Lascoux, J. Kasparian, P. Rohwetter, K. Stelmasczyk, S. Li, A. Lindinger, L. Wöste, P. Béjot, L. Bonacina, and J.-P. Wolf. Optimal Control of Filamentation in Air. to be published in *Applied Physics Letters*, 2006

5. **R. Ackermann**, N. Lascoux, E. Salmon, R. Salamé, J. Kasparian, N. Blanchot, O. Bonville, P. Canal, M. Castaldi, O. Hartmann, C. Lepage, L. Masmande, E. Mazataud, G. Mennerat, L. Patissou, D. Raffestin, S. Champeaux, L. Bergé, C. Guet, L. Bonacina, P. Béjot, J. Extermann, M. Moret, and J.-P. Wolf. 30 Terawatt White Light Laser Reaches the Stratosphere. submitted to *Nature Physics*, 2006

6. G. Méjean, J. Kasparian, J. Yu, S. Frey, E. Salmon, **R. Ackermann**, J.-P. Wolf, L. Bergé, and S. Skupin. UV-Supercontinuum generated by femtosecond pulse filamentation in air: Meter-range versus numerical simulations. *Applied Physics B*, 82(4):341, 2006.

7. G. Méjean, **R. Ackermann**, J. Kasparian, E. Salmon, K. Rethmeier, W. Kalkner, P. Rohwetter, K. Stelmaszczyk, and L. Wöste. Improved laser triggering and guiding of megavolt discharges with dual fs-ns pulses. *Applied Physics Letters*, 88:021101, 2006.

8. P. Rohwetter, K. Stelmaszczyk, L. Wöste, **R. Ackermann**, G. Méjean, E. Salmon, J. Kasparian, J. Yu, and J.-P. Wolf. Filament-induced remote surface ablation for long range laser-induced breakdown spectroscopy operation. *Spectrochimica Acta Part B*, 60:1025, 2005.

9. K. Stelmaszczyk, P. Rohwetter, G. Méjean J. Yu, E. Salmon, J. Kasparian, **R. Ackermann**, J.-P. Wolf, and L. Wöste. Long-distance remote laser-induced breakdown spectroscopy using filamentation in air. *Applied Physics Letters*, 85(18):3977, 2004

10. G. Méchain, G. Méjean, **R. Ackermann**, P. Rohwetter, Y.-B. André, J. Kasparian, B. Prade, K. Stelmaszczyk, J. Yu, E. Salmon, W. Winn, L. A. (Vern) Schlie, A. Mysyrowicz, R. Sauerbrey, L. Wöste, and J.-P. Wolf. Propagation of fs-TW laser filaments in adverse atmospheric conditions. *Applied Physics B*, 80(7):785, 2005.

11. P. Béjot, J. Kasparian, E. Salmon, **R. Ackermann**, N. Gisin, and J.-P. Wolf. Laser Noise Reduction in Air. *Applied Physics Letters*, 88(1):251112, 2006.

12. P. Béjot, J. Kasparian, E. Salmon, **R. Ackermann**, and J.-P. Wolf. Spectral correlation and noise reduction in laser filaments. submitted to *Physical Review A*, 2006.

Bibliography

[Ack03]   R. Ackermann. Untersuchung von Weißlicht-Plasmakanälen mit optischen Methoden. Master's thesis, Freie Universität Berlin, 2003.

[AIB$^+$02] N. Aközbek, A. Iwasaki, B. Becker, M. Scalora, and Chin S. L. Third-harmonic Generation and Self-Channeling in Air Using High-Power Femtosecond Laser Pulses. *Physical Review Letters*, 89:143901, 2002.

[AM76]   N. W. Ashcroft and N. D. Mermin. *Solid State Physics*. Brooks Cole, 1976.

[AMK$^+$05] R. Ackermann, G. Méjean, J. Kasparian, J. Yu, E. Salmon, and J.-P. Wolf. Laser filaments generated and transmitted in highly turbulent air. *Optics Letters*, 31(1):86, 2005.

[AMM$^+$06] R. Ackermann, G. Méchain, G. Méjean, R. Bourayou, M. Rodriguez, K. Stelmaszczyk, J. Kasparian, J. Yu, E. Salmon, S. Tzortzakis, André, J.-F. Bourrillon, L. Tamin, J.-P. Cascelli, C. Camp, C. Davoise, A. Mysyrowicz, R. Sauerbrey, L. Wöste, and J.-P. Wolf. Influence of negative leader propagation on the triggering and guiding of high voltage discharges by laser filaments. *Applied Physics B*, 82(4):561, 2006.

[ASL+06]   R. Ackermann, E. Salmon, N. Lascoux, J. Kasparian, P. Rohwetter, K. Stelmaszczyk, S. Li, A. Lindinger, L. Wöste, P. Béjot, L. Bonacina, and J.-P. Wolf. Optimal Control of Filamentation in Air. to be published in *Applied Physics Letters*, 2006.

[ASR+04]   R. Ackermann, K. Stelmaszczyk, P. Rohwetter, G. Méjean, E. Salmon, J. Yu, J. Kasparian, G. Méchain, V. Bergmann, S. Schaper, B. Weise, T. K. Rethmeier, W. Kalkner, L. Wöste, and J.-P. Wolf. Triggering and guiding of megavolt discharges by laser-induced filaments under rain conditions. *Applied Physics Letters*, 85(23):5781, 2004.

[Bar02]   A. Bartelt. *Steuerung der Wellenpaketdynamik in kleinen Alkaliclustern mit optimierten Femotsekundenpulsen.* PhD thesis, Freie Universität Berlin, 2002.

[BAV+01]   A. Becker, N. Akötzbek, K. Vijayalakshmi, E. Oral, C. M. Bowden, and S. L. Chin. Intensity clamping and re-focusing of intense femtosecond laser pulses in nitrogen molecular gas. *Applied Physics B*, 73(3):287, 2001.

[BBS+97]   T. Baumert, T. Brixner, V. Seyfried, M. Strehle, and G. Gerber. Femtosecond pulse-shaping by an evolutionary algorithm with feedback. *Applied Physics B*, 65:779, 1997. Rapid communications.

[BCI+97]   A. Brodeur, C. Y. Chien, F. A. Ilkov, S. L. Chin, O. G. Kosareva, and V. P. Kandidov. Moving focus in the propagation of ultrashort laser pulses in air. *Optics Letters*, 22(5):304, 1997.

[BGB+94]   A. Bacchiega, A. Gazzani, M. Bernardi, I. Gallimberti, and A. Bondiou. Theoretical modelling of the laboratory negative

stepped leader. In *International Aerospace and Ground Conference on Lightning and Static Electricity, Mannheim*, page 13, 1994.

[BKB04]   S. Bendersky, N. S. Kopeika, and N. Blaunstein. Atmospheric optical turbulence over land in middle east coastal environments: prediction modelling and measurements. *Applied Optics*, 43(20):4070, 2004.

[BKL$^+$95]   A. Braun, G. Korn, X. Liu, D. Du, J. Squier, and G. Mourou. Self-channeling of high-peak-power femtosecond pulses. *Optics Letters*, 20:73, 1995.

[BLG$^+$68]   R. G. Brewer, J. R. Lifsitz, E. Garmire, R. Y. Chiao, and C. H. Townes. Small-Scale Trapped Filaments in Intense Laser Beams. *Physical Review*, 166:326, 1968.

[BMK$^+$05]   R. Bourayou, G. Méjean, J. Kasparian, M. Rodriguez, E. Salmon, J. Yu, H. Lehmann, B. Stecklum, U. Laux, J. Eislöffel, A. Scholz, Hatzes, R. Sauerbrey, L. Wöste, and J.-P. Wolf. White-light filaments for multiparameter analysis of cloud microphysics. *Journal of the Optical Society of America B*, 22(2):369, 2005.

[BOSG00]   T. Brixner, A. Oehrlein, M. Strehle, and G. Gerber. Feedback-controlled femtosecond pulse shaping. *Applied Physics B*, 70:119, 2000.

[BR98]   E. M. Bazelyan and Y. P. Raizer. *Spark Discharge*. CRC Press, 1998.

[BSL$^+$04]   L. Bergé, S. Skupin, F. Lederer, G. Méjean, J. Yu, J. Kaparian, E. Salmon, J.-P. Wolf, M. Rodriguez, L. Wöste, R. Bourayou,

and R. Multiple Filamentation of Terawatt Laser Pulses in Air. *Physical Review Letters*, 92:225002, 2004.

[Cam04]   Cambridge Research & Instrumentation, Inc. *Spatial Light Modulator (SLM) System*, 1.3 edition, 2004.

[CB06]   S. Champeaux and Luc Bergé. Long-range multifilamentation of femtosecond laser pulses versus air pressure. *Optics Letters*, 31(9):1301, 2006.

[CBK+03]   F. Courvoisier, V. Boutou, J. Kasparian, G. Méjean, J. Yu, and J.-P. Wolf. Ultraintense light filaments transmitted through clouds. *Applied Physics Letters*, 83(2):213, 2003.

[Chi71]   T. Chiba. Spot dancing of the laser beam propagated through the turbulent atmosphere. *Applied Optics*, 10(11):2456, 1971.

[CM99]   S. L. Chin and K. Miyazaki. A comment in lightning control using a femtosecond laser. *Japanese Journal of Applied Physics*, 38:2001, 1999.

[CPV+03a] D. Comtois, H. Pépin, F. Vidal, F. A. M. Rizk, C.-Y. Chien, T. W. Johnston, J.-C. Kieffer, B. La Fontaine, F. Martin, C. Potvin, P. Couture, H. Mercure, A. P. Bondiou-Clergerie, P. Lalande, and I. Gallimberti. Triggering and Guiding of an Upward Positive Leader From a Ground Rod With an Ultrashort Laser Pulse - *IEEE Transactions on Plasma Science*, 31(3):387, 2003.

[CPV+03b] D. Comtois, H. Pépin, F. Vidal, F. A. M. Rizk, C.-Y. Chien, T.-W. Johnston, J.-C. Kieffer, B. La Fontaine, F. Martin, C. Potvin, P. Couture, H. Mercure, A. Bondiou-Clergerie, P. Lalande, and I. Gallimberti. Triggering and Guiding of an Upward Positive Leader From a Ground Rod With an Ultrashort Laser Pulse -

I:Experimental Results. *IEEE Transactions on Plasma Science*, 31(3):377, 2003.

[CTY+02] S. L. Chin, A. Talebpour, J. Yang, S. Petit, V. P. Kandidiov, O. G. Kosareva, and M. P. Tamarov. Filamentation of femtosecond laser pulses in turbulent air. *Applied Physics B*, 74:67, 2002.

[DFT+94] K. W. DeLong, D. N. Fittinghoff, R. Trebino, B. Kohler, and K. Wilson. Pulse retrieval in frequency-resolved optical gating based on the method of generalized projections. *Optics Letters*, 19(19):2152, 1994.

[DL04] M. Dantus and V. V. Lozovoy. Experimental Coherent Laser Control of Physicochemical Processes. *Chemical Review*, 104:1813, 2004.

[DM69] E. L. Dawes and J. H. Marburger. Computer studies in self-focusing. *Physical Review*, 179:862, 1969.

[DR96] J.-C. Diels and W. Rudolph. *Ultrashort laser pulse phenomena.* Academic Press, 1996.

[DSLS84] S. De Silvestri, P. Laporta, and O. Svelto. The Role of Cavity Dispersion in CW Mode-Locked Lasers. *IEEE Journal of Quantum Electronics*, 20(5):533, 1984.

[DTHW94] K. W. DeLong, R. Trebino, J. Hunter, and W. E. White. Frequency-resolved optical gating with the use of second-harmonic generation. *Journal of the Optical Society of America B*, 11(11):2206, 1994.

[DTW97] M. A. Dugan, J. X. Tull, and W. S. Warren. High-resolution acousto-optic shaping of unamplified and amplified femtosec-

ond laser pulses. *Journal of the Optical Society of America B*, 14(9):2348, 1997.

[EE98]   J. Eichler and H. J. Eichler. *Laser*. Springer, 1998.

[FEI⁺05]   G. Fibich, S. Eisenmann, B. Ilan, Y. Erlich, M. Fraenkel, Z. Henis, A. Gaeta, and A. Zigler. Self-focusing Distance of Very High Power Laser Pulses. *Optics Express*, 13(15):5897, 2005.

[FGS81]   R. L. Fork, B. I. Greene, and C. V. Shank. Generation of optical pulses shorter than 0.1 psec by colliding pulse mode locking. *Applied Physics Letters*, 38(9):671, 1981.

[FI00]   G. Fibich and B. Ilan. Self-focusing of elliptic beams: an example of the failure of the aberrationless approximation. *Journal of the Optical Society of America*, 17:1749, 2000.

[Gal79]   I. Gallimberti. The mechanism of the long spark formation. *Journal de Physique*, C7(7):193, 1979.

[GHJR75]   G. Gruber, B. Hutzler, J. Jouraire, and J. P. Riu. Contribution a l'étude des Grandes Etincelles en Polarité Negative. *ISH Zürich*, 1975.

[GKK03]   I. S. Golubtsov, V. P. Kandidov, and O. G. Kosareva. Initial phase modulation of a high-power femtosecond laser pulse as a tool for controlling its filamentation and generation of a supercontinuum in air. *IEEE Journal of Quantum Electronics*, 33:525, 2003.

[Gro81]   Les Renardières Group. Negative Discharges in Long Air Gaps at Les Renardières. *Electra*, 75:67, 1981.

[GS76]   B. N. Gorin and A. V. Shkilev. Electric Discharge Development in Long Bar Plane Gaps in the Presence of Negative Impulse Voltage. *Elektrichestvo*, 6(1976), 1976.

[HCTS91]   J. P. Heritage, E. W. Chase, R. N. Thurston, and M. Stern. A simple Femtosecond Optical Third Order Disperser. In *presented at the Conference on Lasers and Electro-optics, Baltimore, MD*, 1991.

[HSL06]   G. Heck, J. Sloss, and R. J. Levis. Adaptive control of the spatial position of white light filaments in an aqueous solution. *Optics Communications*, 259:216, 2006.

[HTG+94]   C. W. Hillegas, J. X. Tull, D. Goswani, D. Stickland, and W. S. Warren. Femtosecond laser pulse shaping by use of microsecond radiofrequency pulses. *Optics Letters*, 19:737, 1994.

[HZL+05]   Z. Q. Hao, J. Zhang, Y. T. Li, X. Lu, X. H. Yuan, Z. Y. Zheng, Z. H. Wang, W. J. Ling, and Z. Y. Wei. Prolongation of the fluorescence lifetime of plasma channels in air induced by femtosecond laser pulses. *Applied Physics B*, 80(4):627, 2005.

[JR92]   R . S. Judson and H. Rabitz. Teaching lasers to control molecules. *Physical Review Letters*, 68:1500, 1992.

[KAS+05]   V. P. Kandidov, N. Akosbek, M. Scarola, O. G. Kosareva, A. V. Nyakk, Q. Luo, S. A. Husseini, and S. L. Chin. Towards a control of multiple filamentation by spatial regularization of a high-power femtosecond laser-pulse. *Applied Physics B*, 80:267, 2005.

[KKB+97]   O. G. Kosareva, V. P. Kandidov, A. Brodeur, C. Y. Chen, and S. L. Chin. Conical emission from laser-plasma interactions in

the filamentation of powerful ultrashort laser pulses in air. *Optics Letters*, 22(17):1332, 1997.

[KKG+03] V. P. Kandidov, O. G. Kosareva, I. S. Golubtsov, W. Liu, N. Becker, A. Aközbek, C. M. Bowden, and S. L. Chin. Self-transformation of a powerful femtosecond laser pulse into a white-light laser pulse in bulk optical media (or super-continuum generation). *Applied Physics B*, 77(2-3):149, 2003.

[KKMW03] M. Kolesik, G. Katona, J. V. Monoleny, and E. M. Wright. Theory and simulation of supercontinuum generation in transparent bulk media. *Applied Physics B*, 77(2-3):185, 2003.

[KKT+99] V. P. Kandidov, O. G. Kosareva, M. P. Tamarov, A. Brodeur, and S. L. Chin. Nucleation and random movements of filaments in the propagation of high-power laser radiation in a turbulent atmosphere. *Quantum Electronics*, 10(29):911, 1999.

[KRM+03] J. Kasparian, M. Rodriguez, G. Méjean, J. Yu, E. Salmon, H. Wille, R. Bourayou, S. Frey, Y.-B. André, A. Mysyrowicz, R. Sauerbrey, J.-P. Wolf, and L. White-light filaments for atmospheric analysis. *Science*, 301:61, 2003.

[KSC00] J. Kasparian, R. Sauerbrey, and S. L. Chin. The critical laser intensity of self-guided light filaments in air. *Applied Physics B*, 71:877 – 879, 2000.

[KSM+00] J. Kasparian, R. Sauerbrey, D. Mondelain, S. Niedermeier, J. Yu, J.-P. Wolf, Y. B. André, M. Franco, B. Prade, A. Mysyrowicz, S. Tzortzakis, M. Infrared extension of the supercontinuum generated by fs-TW-laser pulses propagating in the atmosphere. *Optics Letters*, 25(18):1397, 2000.

[LFCC+00] B. La Fontaine, D. Comtois, C.-Y. Chien, A. Desparois, F. Génin, G. Jarry, T. Johnston, J.-C. Kieffer, F. Martin, R. Mawassi, H. Pépin, F. A. M. Guiding large-scale spark discharges with ultrashort pulse laser filaments. *Journal of Applied Physics*, 88(2), 2000.

[LFVC+99] B. La Fontaine, F. Vidal, D. Comtois, C.-Y. Chien, A. Desparois, T. W. Johnston, J.-C. Kieffer, H. P. Mercure, H. Pépin, and F. A. M. Rizk. The influence of electron density on the formation of streamers in electrical discharges triggered with ultrashort laser pulses. *IEEE Transactions on Plasma Science*, 27(3):688, 1999.

[LGR+98] H. R. Lange, G. Grillon, J.-F. Ripoche, M. A. Franco, B. Lamouroux, B. S. Prade, A. Mysyrowicz, E. T. J. Nibbering, and A. Chiron. Anomalous long-range propagation of femtosecond laser through air: moving focus or pulse-self-guiding? *Optics Letters*, 23(2):120, 1998.

[LKG+02] W. Liu, O. Kosareva, I. S. Golubtsov, A. Iwasaki, A. Becker, V. P. Kandidov, and S. L. Chin. Random deflection of the white-light beam during self-focusing and filamentation of femtosecond laser pulse in water. *Applied Physics B*, 75:595, 2002.

[Loe36] L. B. Loeb. The Problem of the Mechanism of Static Spark Discharge. *Review of Modern Physics*, 8:267, 1936.

[LS69] M. T. Loy and Y. R. Shen. Small-Scale Filaments in Liquids and Tracks of Moving Focii. *Physical Review Letters*, 22:994, 1969.

[Lup04] C. Lupulescu. *Femtosecond Analysis and Feedback Control of Molecular Processes in Organometallic and Alkaline Systems*. PhD thesis, Freie Universität Berlin, 2004.

[LVJ+99]   B. LaFontaine, F. Vidal, Z. Jiang, C.-Y. Chien, D. Comtois, A. Desparois, T. W. Johnston, J.-C. Kieffer, H. Pépin, and H.P. Mercure. Filamentation of ultrashort laser pulse laser beams resulting from their propagation over long distances in air. *Physics of Plasmas*, 6(5):1615, 1999.

[LWM+95]   X. Liu, R. Wagner, A. Maksimchuk, E. Goodman, J. Workman, D. Umstadter, and A. Migus. Nonlinear temporal diffraction and frequency shifts resulting from pulsed shaping in chirped-pulse amplification systems. *Optics Letters*, 20(10):1163, 1995.

[MAK+06]   G. Méjean, R. Ackermann, J. Kasparian, E. Salmon, K. Rethmeier, W. Kalkner, P. Rohwetter, K. Stelmasczszyk, and L. Wöste. Improved laser triggering and guiding of megavolt discharges with dual fs-ns pulses. *Applied Physics Letters*, 88:021101, 2006.

[Mar75]   J. H. Marburger. Self-focusing: Theory. *Progress in Quantum Electronics*, 4:35, 1975.

[Mar87]   O. Martinez. 3000 times grating compressor with positive velocity dispersion: Application to fiber compensation in 1.3 - 1.6 µm region. *IEEE Journal of Quantum Electronics*, 23(1):59, 1987.

[MAS93]   M. Miki, Y. Aihara, and T. Shindo. Development of long discharges guided by a pulsed CO_2 laser. *Journal of Physics D:Applied Physics*, 26:1244, 1993.

[MCA+04]   G. Méchain, A. Couairon, Y.-B. Andé, C. D'Amico, M. Franco, B. Prade, S. Tzortzakis, A. Mysyrowicz, and R. Sauerbrey. Long-range self-channeling of infrared laser pulses in air: a new propagation regime without ionization. *Applied Physics B*, 79:379, 2004.

[MDA+05] G. Méchain, C. D'Amico, Y.-B. André, S. Tzortzakis, M. Franco, B. Prade, A. Mysyrowicz, A. Couairon, E. Salmon, and R. Sauerbrey. Range of plasma filaments created in air by a multi-terawatt femtosecond laser. *Optics Communications*, 247:171, 2005.

[Mea84] R. M. Measures. *Laser Remote Sensing: Fundamentals and Applications.* John Wiley and Sons Inc, 1984.

[Mee40] J. M. Meek. A Theory of Spark Discharge. *Physical Review*, 57:722, 1940.

[Méj05] G. Méjean. *Propagation d'impulsions Térawatts femtosecondes dans l'atmosphére et applications.* PhD thesis, Université Claude Bernard - Lyon 1, 2005.

[Mes99] D. Meschede. *Optik, Licht und Laser.* Teubner Studienbücher, 1999.

[MKY+04] G. Méjean, J. Kasparian, J. Yu, S. Frey, E. Salmon, and J.-P. Wolf. Remote Detection and Identification of Biological Aerosols using a Femtosecond Terawatt Lidar System. *Applied Physics B*, 78(5):535, 2004.

[MKY+05] G. Méjean, J. Kasparian, J. Yu, E. Salmon, S. Frey, J.-P. Wolf, S. Skupin, A. Vincotte, R. Nuter, S. Champeaux, and L. Bergé. Multifilamentation transmission through fog. *Physical Review E*, 72:026611, 2005.

[MKY+06] G. Mejean, J. Kasparian, J. Yu, S. Frey, E. Salmon, R. Ackermann, J.-P. Wolf, L. Bergé, and S. Skupin. UV-Supercontinuum generated by femtosecond pulse filamentation in air: Meter-range experiments versus numerical simulations. *Applied Physics B*, 82(1 - 3):341, 2006.

[MMA$^+$05] G. Méchain, G. Méjean, R. Ackermann, P. Rohwetter, Y.-B. André, J. Kasparian, B. Prade, S. Stelmaszczyk, J. Yu, E. Salmon, W. Winn, L. A. (Vern) Wolf. Propagation of fs-TW laser filaments in adverse atmospheric conditions. *Applied Physics B*, 80:785, 2005.

[MSA96] M. Miki, T. Shindo, and Y. Aihara. Mechanisms of guiding ability of CO_2 laser-produced plasmas on pulsed discharges. *Journal of Physics D:Applied Physics*, 29:1984, 1996.

[MSB$^+$88] P. Maine, D. Strickland, P. Bado, M. Pessot, and G. Mourou. Generation of Ultrahigh Peak Power Pulses by Chirped Pulse Amplification. *IEEE Journal of Quantum Electronics*, 24(2):398, 1988.

[MW96] M. Miki and A. Wada. Guiding of electrical discharges under atmospheric air by ultraviolet laser-produced plasma channel. *Journal of Applied Physics*, 80(6):3208, 1996.

[NB37] R. A. Nielsen and N. E. Bradbury. Electron and Negative Ion Mobilities in Oxygen, Air, Nitrous Oxide and Ammonia. *Physical Review*, 51:69, 1937.

[NCG$^+$96] E. T. J. Nibbering, P. F. Curley, G. Grillon, B. S. Prade, M. A. Franco, F. Salin, and A. Mysyrowicz. Conical emission from self-guided femtosecond pulses in air. *Optics Letters*, 21(1):62, 1996.

[NGF$^+$97] E. Nibbering, G. Grillon, M. Franco, B. Prade, and A. Mysyrowicz. Determination of the inertial contribution to the nonlinear refractive index of air,N_2, and O_2 by use of unfocused high-intensity femtosecond laser pulses. *Journal of the Optical Society of America B*, 14(3):650, 1997.

[ODG+94]   P. Ortega, P. Domens, A. Gibert, B. Hutzler, and G. Riquel. Performance of a 16.7 m air rod-plane gap under a negative switching impulse. *Journal of Physics D:Applied Physics*, 27:2379, 1994.

[Pay92]   J. Paye. The chronocyclic representation of ultrashort light pulses. *IEEE Journal of Quantum Electronics*, 28:2262, 1992.

[PCV+01]   H. Pépin, D. Comtois, F. Vidal, C. Y. Chien, A. Desparois, T. W. Johnston, J. C. Kieffer, B. La Fontaine, F. Martin, F. A. M. Rizk, C. Potvin, I. Gallimberti. Triggering and guiding high-voltage large-scale leader discharges with sub-joule ultrashort laser pulses. *Physics of Plasmas*, 8(5):2532, 2001.

[PHH89]   D. M. Pennington, M. A. Henesian, and R. W. Hellwarth. Nonlinear index of air at 1.053 µm. *Physical Review A*, 39:3003, 1989.

[PPS+99]   M. D. Perry, D. Pennington, B. C. Stuart, G. Tietbohl, J. A. Britten, C. Brown, S. Herman, B. Golick, M. Kartz, J. Miller, H. T. Powell, V. Yanovsky. Petawatt laser pulses. *Optics Letters*, 24(3):160, 1999.

[PWKC99]   N. A. Papadogiannis, B. Witzel, C. Kalpouzos, and D. Chralmbidis. Observation of Attosecond Light Localization in Higher Order Harmonic Generation. *Physical Review Letters*, 83(21):4289, 1999.

[Rai97]   Raizer. *Gas Discharge Physics*. Springer, 1997.

[Ran59]   D. H. Rank. *Advances in Spectroscopy*. H. W Thompson, interscience edition, 1959.

[RBM+04]   M. Rodriguez, R. Bourayou, G. Méjean, J. Kasparian, J. Yu, E. Salmon, A. Scholz, B. Stecklum, J. Eislöffel, U. Laux, A. P.

Hatzes, R. Sauerbrey, L. Kilometer-range non-linear propagation of fs laser pulses. *Physical Review E*, 69:036607, 2004.

[Rob97]   P. A. Robinson. Nonlinear wave collapse and strong turbulence. *Review of Modern Physics*, 69(2):507, 1997.

[Rod04]   M. Rodriguez. *Terawatt-Femtosekunden-Laserpulse in der Atmosphäre: Phänomene und Anwendungen*. PhD thesis, Freie Universität Berlin, 2004.

[ROG+95]   Th. Reess, P. Ortega, A. Gibert, P. Domens, and P. Pignolet. An experimental study of negative discharge in a 1.3 m point-plane air gap: the function of the space stem in the propagation mechanism. *Journal of Physics D:Applied Physics*, 28:2306, 1995.

[Roh04]   P. Rohwetter. Femtosecond Terawatt Pulses for Remote Laser Induced Breakdown Spectroscopy. Master's thesis, Freie Universität Berlin, 2004.

[RSD01]   P. Rambo, J. Schwarz, and J.-C Diels. High-voltage electrical discharges induced by an ultrashort-pulse UV laser system. *Journal of Optics A: Pure and Applied Optics*, 3:146, 2001.

[RSW+02]   M. Rodriguez, R. Sauerbrey, H. Wille, L. Wöste, T. Fujii, Y.-B. André, A. Mysyrowicz, L. Klingbeil, K. Rethmeier, W. Kalkner, J. Kasparian, E. Triggering and guiding megavolt discharges by use of laser-induced ionized filaments. *Optics Letters*, 27(9):772, 2002.

[RSW+05]   Ph. Rohwetter, K. Stelmaszczyk, L. Wöste, R. Ackermann, G. Méjean, E. Salmon, J. Kasparian, J. Yu, and J.-P. Wolf. Filament-induced remote surface ablation for long range laser-

induced breakdown spectroscopy operation. *Spectrochimica Acta Part B*, 60:1025, 2005.

[RYM+04]   Ph. Rohwetter, J. Yu, G. Méjean, K. Stelmaszczyk, E. Salmon, J. Kasparian, L. Wöste, and J.-P. Wolf. Remote LIBS with ultrashort pulses: characteristics in pico- and femtosecond regimes. *Journal of Analytical Atomic Spectrometry*, 19:437, 2004.

[SBP+04]   S. Skupin, L. Bergé, U. Peschel, F. Lederer, G. Méjean, J. Yu, J. Kasparian, E. Salmon, J.-P. Wolf, M. Rodriguez, and L. Wöste. Filamentation of femtosecond light pulses in air: Turbulent cells versus long-range clusters. *Physical Review E*, 70:046602, 2004.

[SC94]   D. Strickland and P. B. Corkum. Resistance of short pulses to self-focusing. *Journal of the Optical Society of America B*, 11(3):492, 1994.

[SKS91]   D. E. Spence, P. N. Kean, and W. Sibbett. 60-fsec pulse generation from a self-mode-locked Ti-Sapphire laser. *Optics Letters*, 16(1):42, 1991.

[SM85]   D. Strickland and G. Mourou. Compression of amplified chirped pulses. *Optics Communications*, 56(3):219, 1985.

[SMAW93]   T. Shindo, M. Miki, Y. Aihara, and A. Wada. Laser guided discharges in long gaps. *IEEE Transactions on Power Delivery*, 8(4):2016, 1993.

[SRM+04]   K. Stelmaszczyk, Ph. Rohwetter, G. Méjean, J. Yu, E. Salmon, J. Kasparian, R. Ackermann, J.-P. Wolf, and L. Wöste. Long-distance remote laser-induced breakdown spectroscopy using filamentation in air. *Applied Physics Letters*, 85(18):3977, 2004.

[SS99]   H. Schillinger and R. Sauerbrey. Electrical conductivity of long plasma channels in air generated by self-guided femtosecond laser pulses. *Applied Physics B*, 68:753 – 756, 1999.

[SSP91]   F. Salin, J. Squier, and M. Piche. Mode locking of Ti:Al$_2$O$_3$ lasers and self-focusing: a Gaussian approximation. *Optics Letters*, 16(21):1674, 1991.

[STL68]   C. A. Sacchi, C. H. Townes, and J. R. Lifsitz. Anti-stokes generation in trapped filaments of light. *Physical Review*, 174(2):439, 1968.

[Tat71]   V. I. Tatarski. The Effects of the Turbulent Air on the Wave Propagation. *National Technical Information Service, U.S. Department of Commerce*, 1971.

[TDF$^+$97] R. T. Trebino, K. W. DeLong, D. N. Fittinghoff, J. N. Seetser, M. A. Krumbügel, B. A. Richman, and D. J. Kane. Measuring ultrashort laser pulses in the time-frequency domain using frequency-resolved optical gating. *Review of Scientific Instruments*, 68(9):3277, 1997.

[TFA$^+$99] S. Tzortzakis, M. A. Franco, Y.-B. André, A. Chiron, B. Lamouroux, S. Prade, and A. Mysyrowicz. Formation of a conducting channel in air by self-guided laser pulses. *Physical Review E, Rapid Communications*, 60:3505, 1999.

[Tow00]   J. S. Townsend. The Conductivity produced in Gases by the Motion of Negatively-charged Ions. *Nature*, 62:340, 1900.

[TPC99]   A. Talebpour, S. Petit, and S. L. Chin. Re-focusing during the propagation of a focused femtosecond Ti:Sapphire laser pulse in air. *Optics Communications*, 171(4 - 6):285, 1999.

[TPFM00]   S. Tzortzkais, B. Prade, M. Franco, and A. Mysyrowicz. Time-evolution of the plasma channel at the trail of a self-guided IR femtosecond laser pulse in air. *Optics Communications*, 181:123, 2000.

[Tre69]   E. B. Treacy.   Optical Pulse Compression With Diffraction Gratings. *IEEE Journal of Quantum Electronics*, 5(9):454, 1969.

[Tre00]   R. Trebino. *Frequency-Resolved Optical Gating: The Measurement of Ultrashort Laser Pulses.* Kluwer Academic Publishers, 2000.

[Tzo01]   S. Tzortzakis. *Femtosecond laser pulse filamentation in nonlinear transparent media.* PhD thesis, ENSTA - Ecole Polytechnique, Chemin de la Hunière, 91761 Palaiseau Cedex, France, 2001.

[Uma01]   M. A. Uman. *The Lightning Discharge.* Dover Publications, 2001.

[USY$^+$99]   S. Uchida, Y. Shimada, H. Yasuda, S. Motokoshi, T. Yamanaka, Z.-I. Kawasaki, and K. Tsubakimoto. Laser-triggered lightning in field experiments. *Journal of Optical Technology*, 66(3):199, 1999.

[Web03]   S. Weber. Application of evolution strategies on arbitrary pulse form generation, white light generation and isotope ratio optimization of k_2. Master's thesis, Freie Universität Berlin, 2003.

[Wei00]   A. M. Weiner. Femtosecond pulse shaping using spatial light modulators. *Review of Scientific Instruments*, 71(5):1929, 2000.

[WHK88]   A. M. Weiner, J. P. Heritage, and E. M. Kirschner. High-resolution femtosecond pulse-shaping. *Journal of the Optical Society of America B*, 5(5):1563, 1988.

[Wig32]   E. Wigner. On the quantum correction for thermodynamic equilibrium. *Physical Review*, 40:749, 1932.

[WLPWI92] A. M. Weiner, D. E. Leaird, J. S. Patel, and J. R. Wullert II. Programmable Shaping of Femtosecond Optical Pulses by Use of 128-Element Liquid Crystal Phase Modulator. *IEEE Journal of Quantum Electronics*, 28(4):908, 1992.

[WN95]   M. M. Wefers and K A. Nelson. Analysis of programmable ultrahort waveform generation using liquid-crystal spatial light modulators. *Journal of the Optical Society of America B*, 12(7):1343, 1995.

[WRK+02] H. Wille, M. Rodriguez, J. Kasparian, D. Mondelain, J. Yu, A. Mysyrowicz, R. Sauerbrey, J.-P. Wolf, and L. Wöste. Teramobile: a mobile femtosecond-terawatt laser and detection system. *European Physical Journal - Applied Physics*, 20:183, 2002.

[WWW+97] L. Wöste, C. Wedekind, H. Wille, P. Rairoux, B. Stein, S. Nikolov, Ch. Werner, S. Niedermeyer, F. Ronneberger, H. Schillinger, and R. Sauerbrey. Femtosecond Atmospheric Lamp. *Laser und Optoelektronik*, 29(51), 1997.

[YMK+03] J. Yu, D. Mandelain, J. Kasparian, E. Salmon, S. Geffroy, C. Favre, V. Boutou, and J.-P. Wolf. Sonographic Probing of Laser Filaments in Air. *Applied Optics*, 42(36):7117, 2003.

[YZL+02]   H. Yang, J. Zhang, Y. Li, J. Zhang, Y. Li, Z. Chen, H. Teng, Z. Wei, and Z. Sheng. Characteristics of self-guided laser plasma channels generated by femtosecond laser pulses in air. *Physical Review E*, 66(1):016406, 2002.

[YZY⁺01]   H. Yang, J. Zhang, W. Yu, Y. J. Li, and Z. Y. Wei. Long plasma channels generated by femtosecond laser pulses. *Physical Review E*, 65(1):016406, 2001.

[YZZ⁺05]   H. Yang, J. Zhang, Q. Zhang, Z. Hao, Y. Li, Z. Wang, Q.-L. Dong, X. Lu, Z. Wei, Z.-M. Sheng, J. Yu, and W. Yu. Polarization dependent supercontinuum generation from light filaments in air. *Optics Letters*, 30:534, 2005.

[ZDWE95]   X. M. Zhao, J.-C. Diels, C. Y. Wang, and J. M. Elizondo. Femtosecond ultraviolet laser pulse induced lightning discharges in gases. *IEEE Journal of Quantum Electronics*, 31(3):599, 1995.

[ZJD⁺06]   J. Zhu, Z. Ji, Y. Deng, J. Liu, R. Li, and Z. Xu. Long lifetime plasma channel in air generated by multiple femtosecond laser pulses and an external electrical field. *Optics Express*, 14(11):4915, 2006.

[ZMB⁺99]   E. Zeek, K. Maginnis, S. Backus, U. Russek, M. Murnane, G. Mourou, H. Kapteyn, and G. Vdovin. Pulse compression by use of deformable mirrors. *Optics Letters*, 24(7):493, 1999.

Abstract

When an ultrashort-terawatt laser pulse is propagating through the atmosphere, long filaments may develop. Their light is confined in an area of about 100 µm over distances up to several hundred meters, and an air plasma is generated along the beam path. Moreover, filamentation leads to a significant broadening of the initial pulse spectrum. These properties open the perspective to improve classical LIDAR techniques as well as to laser lightning control.

In the laboratory, we have shown that the filaments survive the propagation through highly turbulent air as well as under adverse atmospheric conditions such as rain and reduced pressure. By using an multi-terawatt, ultrashort laser pulse, the white-light LIDAR signal could be detected at an altitude of more than 20 km for the first time.

In cooperation with high-voltage facilities, the effective plasma lifetime for the laser guiding of discharges and the achievable guided lengths have been determined. By using an additional nanosecond laser pulse, the triggering probability could be significantly enhanced. Furthermore, we have shown that the triggering and guiding is possible in artificial rain.

These results encourage further research aiming at the application of white-light LIDAR and real-scale lightning control.

Résumé

La propagation d'une impulsion térawatt ultra-brève dans l'atmosphère peut s'accompagner du phènomène de filamentation. La lumière se trouve alors auto-guidée dans des plasmas appelés filaments dont le diamètre est de l'ordre de 100 µm et la longueur peut s'étendre jusqu'à quelques centaines de mètres. De plus, le spectre initial de l'impulsion est considerablement élargi. Ces propriétés offrent la possibilité d'améliorer la technique LIDAR et de contrôler la foudre.

Nous avons montré que les filaments survivent à la propagation dans une turbulence forte et peuvent se développer sous une pression atmosphérique réduite et sous la pluie. Pour la première fois, la lumière blanche genérée par une impulsion ultra-brève, multi-terawatt a été détectée à une altitude de 20 km.

En collaberation avec des installations haute-tension, nous avons déterminé la durée de vie du plasma du filament et la longueur sur laquelle il est possible de guider des décharges électriques. Nous avons pu augmenter l'efficacité de déclenchement avec une configuration à double impulsion. Enfin, nous avons montré que le déclenchement et le guidage sont possibles sous une pluie artificielle.

Ces résultats se sont révélés très encourageants en vue d'expériences LIDAR à lumière blanche et du contrôle de la foudre.

Mots clés

impulsion ulta-brève - filamentation - plasma - lumière blanche - décharge électrique

Abstract

When an ultrashort-terawatt laser pulse is propagating through the atmosphere, long filaments may develop. Their light is confined in an area of about 100 µm over distances up to several hundred meters, and an air plasma is generated along the beam path. Moreover, filamentation leads to a significant broadening of the initial pulse spectrum. These properties open the perspective to improve classical LIDAR techniques as well as to laser lightning control.

In the laboratory, we have shown that the filaments survive the propagation through highly turbulent air as well as under adverse atmospheric conditions such as rain and reduced pressure. By using an multi-terawatt, ultrashort laser pulse, the white-light LIDAR signal could be detected at an altitude of more than 20 km for the first time.

In cooperation with high-voltage facilities, the effective plasma lifetime for the laser guiding of discharges and the achievable guided lengths have been determined. By using an additional nanosecond laser pulse, the triggering probability could be significantly enhanced. Furthermore, we have shown that the triggering and guiding is possible in artificial rain.

These results encourage further research aiming at the application of white-light LIDAR and real-scale lightning control.

Résumé

La propagation d'une impulsion térawatt ultra-brève dans l'atmosphère peut s'accompagner du phènomène de filamentation. La lumière se trouve alors auto-guidée dans des plasmas appelés filaments dont le diamètre est de l'ordre de 100 µm et la longueur peut s'étendre jusqu'à quelques centaines de mètres. De plus, le spectre initial de l'impulsion est considerablement élargi. Ces propriétés offrent la possibilité d'améliorer la technique LIDAR et de contrôler la foudre.

Nous avons montré que les filaments survivent à la propagation dans une turbulence forte et peuvent se développer sous une pression atmosphérique réduite et sous la pluie. Pour la première fois, la lumière blanche genérée par une impulsion ultra-brève, multi-terawatt a été détectée à une altitude de 20 km.

En collaberation avec des installations haute-tension, nous avons déterminé la durée de vie du plasma du filament et la longueur sur laquelle il est possible de guider des décharges électriques. Nous avons pu augmenter l'efficacité de déclenchement avec une configuration à double impulsion. Enfin, nous avons montré que le déclenchement et le guidage sont possibles sous une pluie artificielle.

Ces résultats se sont révélés très encourageants en vue d'expériences LIDAR à lumière blanche et du contrôle de la foudre.